Static and Dynamic properties of Cubic Chiral Magnets

Qian, Fengjiao

DOI
10.4233/uuid:764f8b6b-4fea-4f64-9915-8afe97d54179

Publication date
2017

Document Version
Publisher's PDF, also known as Version of record

STATIC AND DYNAMIC PROPERTIES OF CUBIC CHIRAL MAGNETS

Fengjiao QIAN

STATIC AND DYNAMIC PROPERTIES OF CUBIC CHIRAL MAGNETS

Proefschrift

ter verkrijging van de graad van doctor
aan de Technische Universiteit Delft,
op gezag van de Rector Magnificus prof. ir. K.C.A.M. Luyben,
voorzitter van het College voor Promoties,
in het openbaar te verdedigen op woensdag 14 juni 2017 om 15:00 uur

door

Fengjiao QIAN

Master in Materials Science and Engineering,
Nanjing University of Aeronautics and Astronautics, China,
geboren te Anhui, China.

This dissertation has been approved by the

promotor: Prof. dr. C. Pappas

Composition of the doctoral committee:

Rector Magnificus,	Chairperson
Prof. dr. C. Pappas,	Delft University of Technology
Independent members:	
Dr. ir. A.A. van Well	Delft University of Technology
Prof. dr. E.H. Brück	Delft University of Technology
Prof. dr. M.V. Mostovoy	University of Groningen
Dr. habil. G. Chaboussant	Laboratoire Léon Brillouin
Dr. E. Lelièvre-Berna	Institut Laue-Langevin
Dr. habil. H. Wilhelm	Diamond Light Source
Reserve member:	
Prof. dr. P. Dorenbos	Delft University of Technology

The research carried out in this thesis has been financially supported by the China Scholarship Council and the European Union Seventh Framework Programme FP7/2007-2013 under Grant Agreement No. 283883.

ISBN 978-94-92516-56-5

An electronic version of this dissertation is available at
http://repository.tudelft.nl/.

Dedicated to my parents and my husband Xuefei

CONTENTS

1 Introduction **1**

2 Experimental Techniques **7**
2.1 DC magnetisation and AC susceptibility 7
2.2 Neutron scattering 8
2.2.1 Small angle neutron scattering 11
2.2.2 Neutron polarimetry 11
2.2.3 Neutron spin echo spectroscopy 15

3 Magnetic relaxation phenomena in Cu_2OSeO_3 and phase diagram close to T_C **19**
3.1 Introduction 20
3.2 Experimental details 21
3.3 Magnetization 22
3.4 AC susceptibility at 0.8 Hz 24
3.5 Frequency dependence of the susceptibility 29
3.6 Cole-Cole analysis 35
3.7 Phase diagram close to T_C 36
3.8 Conclusion 39

4 Neutron scattering investigations of magnetic correlations and dynamics close to T_C for Cu_2OSeO_3 **43**
4.1 Introduction 44
4.2 Experiment details 45
4.3 Magnetic correlations at zero field 45
4.4 Magnetic phase diagram and skyrmion lattice scattering 51
4.5 Magnetic relaxation under magnetic fields 54
4.6 Discussion 57
4.7 Conclusion 59

5 Low temperature magnetism of Cu_2OSeO_3 below 50 K: Magnetisation, susceptibility and neutron scattering studies **63**
5.1 Introduction 64
5.2 Experimental details 64
5.2.1 Sample details 64

5.2.2 DC magnetisation and AC susceptibility 65
5.2.3 Neutron scattering 65
5.3 DC magnetisation 65
5.4 AC susceptibility at 10 Hz 68
5.5 Frequency dependence of ZFC AC magnetic susceptibility 69
5.6 Magnetic phase diagrams below 50 K 73
5.7 Neutron scattering 75
5.8 Discussion 78
5.9 Conclusion 79

6 AC susceptibility and dissipation phenomena in MnSi 81
6.1 Introduction 82
6.2 Experimental details 82
6.3 Results 83
6.4 Discussion 86
6.5 Conclusion 87

7 Neutron scattering investigation of magnetic correlations in FeGe 91
7.1 Introduction 92
7.2 Experimental details 92
7.3 Magnetic behaviour close to T_C 94
7.4 $B-T$ Phase Diagram 97
7.5 Helix reorientation at low temperatures and zero field 101
7.6 Conclusion 102

Summary 105

Samenvatting 107

Acknowledgements 111

List of Publications 115

Curriculum Vitæ 117

1

INTRODUCTION

Chirality designates the break of symmetry between left and right and is ubiquitous in nature, from the fundamental interactions, to elementary particles, condensed matter physics, chemistry and biology. A chiral crystal structure with break of inversion symmetry is illustrated in Fig. 1.1(a) and (b) as an example for the case, where the original lattice and the associated one after point inversion operation are non-superposable. This thesis explores the interrelations of chiral and magnetic properties in non-centrosymmetric systems, where the lack of inversion symmetry in the crystal structure gives rise to antisymmetric Dzyaloshinsky-Moriya (DM) magnetic interactions [1, 2]. These tend to twist the magnetic moments leading to magnetic chirality. A most fascinating effect of magnetic chirality is the stabilisation of chiral skyrmions [3–5], which are topologically protected and presently at the focus of scientific interest.

In the recent years, a variety of chiral magnets that host magnetic skyrmions have been found, which all belong to the chiral cubic space group $P2_13$ and lack inversion symmetry in their crystal structure. The materials range from the metallic MnSi [4, 6–8], FeGe [9–11], $Mn_{1-x}Fe_xGe$ [12, 13] and the semiconducting $Fe_{1-x}Co_xSi$ [5, 14–16], to the insulating Cu_2OSeO_3 [17–19]. These systems all show the same generic behavior and their magnetic ground state can be derived from the Landau-Ginzburg-Wilson (LGW) functional with three interactions corresponding to well-separated energy scales [20]. The strongest ferromagnetic exchange favours a collinear spin arrangement, the weaker Dzyaloshinsky-Moriya (DM) interaction [1, 2] twists the magnetic moments to a helix, and the weakest magnetic anisotropy fixes the helix prorogation direction along a specific crystallographic axis. The pitch of the helices ℓ varies from ~ 3 to ~ 100 nm from one material to another and reflects the ratio between the ferromagnetic and DM in-

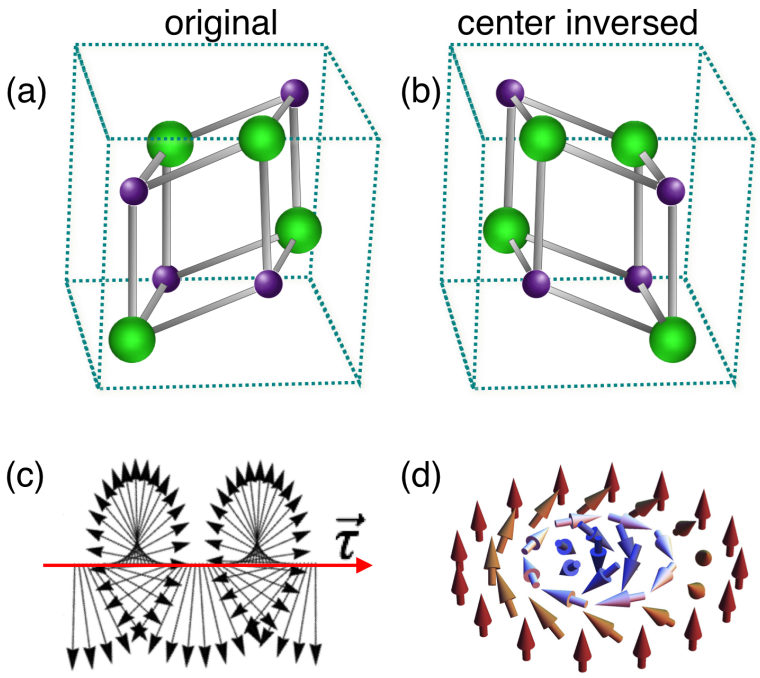

Figure 1.1: Illustration of crystal and magnetic structures of chiral magnets: (a) and (b) a crystal structure of the $P2_13$ space group before and after center inversion operation. The spheres represent a single atom or a cluster of atoms (e.g. tetrahedra of Cu^{2+} ions in the case of Cu_2OSeO_3). Arrangement of magnetic moments in a helical order (c) and for a chiral skyrmion (d) after Seki et. al [17].

teractions. The magnetic moments then rotate in the plane perpendicular to the helix propagation direction, as illustrated in Fig. 1.1(c). These helices have also a well defined chirality determined by the sign of the DM interaction and the chirality of the crystallographic structure [13, 21].

The three relevant energy scales are also visible in the magnetic field - temperature phase diagrams of these systems, that follow the same generic scheme as illustrated in Fig. 1.2. At zero field, the magnetic ground state is a helical spiral with the magnetic moments rotating in a plane perpendicular to the helix propagation direction. A weak magnetic field exceeding the magnetic anisotropy reorients the helices along its direction and at the same time cants the magnetic moments towards its direction, inducing the conical phase. Large enough magnetic fields overcome the DM interactions, and align the magnetic moments inducing the field-polarised state. At intermediate magnetic fields and just below T_C, the A-phase pocket appears, where chiral skyrmions, illustrated in Fig. 1.1(d), are

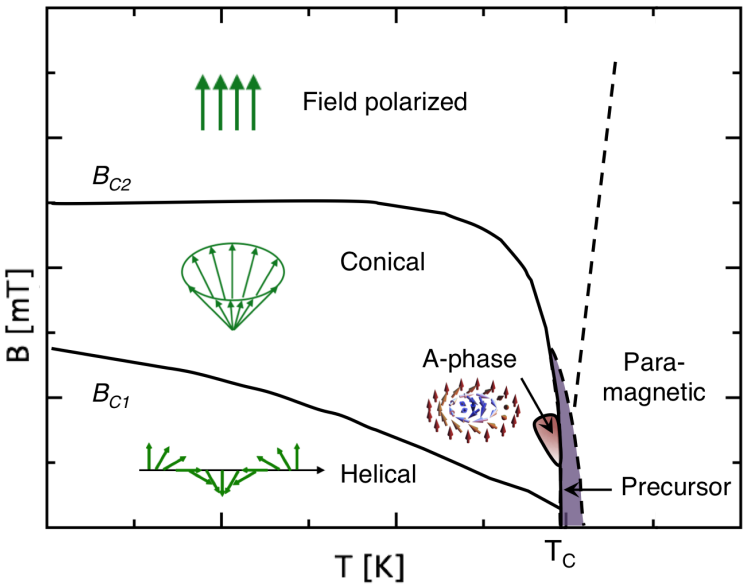

Figure 1.2: Sketch of a typical magnetic phase diagram for skyrmion hosting chiral magnets. The magnetic correlations of the helical, conical, *A*- and field-polarised phases are illustrated in the insets.

stabilized and form a hexagonal lattice. The phase transition at T_C is often preceded by strong correlations that build up just above T_C, in a so-called precursor phase, the origin of which is subject of debate.

This thesis presents an experimental investigation of Cu_2OSeO_3, MnSi and FeGe by DC magnetization, AC susceptibility, Small Angle Neutron Scattering, also with polarization analysis, and Neutron Spin Echo spectroscopy. The main focus is on Cu_2OSeO_3, which is currently the only insulating and multiferroic chiral magnet, and its magnetic structure, including skyrmions, can be manipulated by electric fields. The thesis comprises the following chapters:

- *Chapter* 2 introduces the experimental techniques employed in this work, DC magnetisation and AC magnetic susceptibility measurements using a Superconducting Quantum Interference Device (SQUID), Small Angle Neutron Scattering (SANS), also with polarisation analysis, and Neutron Spin Echo spectroscopy (NSE).
- *Chapter* 3 presents a DC magnetisation and AC susceptibility study of Cu_2OSeO_3 in the vicinity of T_C = 58.2 K and around the skyrmion lattice *A*-phase. By covering a broad frequency range from 0.1 Hz up to 1 kHz, the

AC susceptibility reveals the characteristic relaxation associated with the transitions between the helical, conical, A- and field-polarised phases. The strong frequency dependence leads to different magnetic field-temperature phase diagrams for different frequencies, which account for the different phase boundaries reported in the literature.

- *Chapter* 4 presents a complementary investigation by SANS and NSE. The analysis of polarised neutron scattering at zero magnetic field provides information on the chiral properties of the magnetic correlations, and NSE unravels their dynamics. The results show a first order helimagnetic transition at T_C and fully chiral short-range correlations above T_C. Investigations under magnetic fields high enough to stablize the skyrmion lattice phase reveal an interplay between the skyrmion lattice phase and the crystal lattice orientation. In addition, the dependence on the magnetic history has been investigated. By rapidly changing the magnetic field, the SANS intensity change can be followed over macroscopic times, revealing patterns corresponding to different phases of the phase diagram.
- *Chapter* 5 presents DC magnetisation, AC susceptibility and SANS investigations of Cu_2OSeO_3 below 50 K. These reveal qualitatively different phase diagrams for magnetic fields applied along the easy ⟨100⟩ and the hard ⟨110⟩ crystallographic directions. The results are discussed in view of theoretical predictions.
- *Chapter* 6 presents AC magnetic susceptibility measurements on the archetype helimagnet MnSi. The measurements cover the whole temperature range from low temperatures up to well above $T_C \sim 29$ K, and a broad range of magnetic fields up to 4 T. The measurements lead to a magnetic phase diagram with the helical, conical, skyrmion lattice and field-polarised phases below T_C. Above T_C strong dissipation has been found at low frequencies and under magnetic field, the origin of which remains unclear.
- *Chapter* 7 presents a SANS investigation of the magnetic correlations in FeGe, which orders at $T_C \sim 278$ K, thus close to room-temperature. Close to T_C, the magnetic correlations are chiral and the transition is possibly of first order. By applying magnetic fields, the magnetic phase diagram close to T_C and around the skyrmion lattice A-phase has been investigated, confirming previous results and revealing additional scattering as a precursor of the skyrmion lattice phase just above T_C.
  At zero magnetic field, the helical order reorients from ⟨100⟩ at high temperatures to ⟨111⟩ at low temperatures. This reorientation occurs between 250 and 200 K and is followed by SANS. The origin of this phenomenon is discussed in conjunction with possible structural changes and magnetoelastic coupling.

REFERENCES

[1] I. Dzyaloshinsky, *A thermodynamic theory of "weak" ferromagnetism of antiferromagnetics,* J. Phys. Chem. Solids **4**, 241 (1958).

[2] T. Moriya, *Anisotropic superexchange interaction and weak ferromagnetism,* Physical review **120**, 91 (1960).

[3] A. N. Bogdanov and D. A. Yablonskii, *Thermodynamically stable "vortices" in magnetically ordered crystals. The mixed state of magnets,* Sov. Phys. JETP **68**, 101 (1989).

[4] S. Mühlbauer, B. Binz, F. Jonietz, C. Pfleiderer, A. Rosch, A. Neubauer, R. Georgii, and P. Böni, *Skyrmion lattice in a chiral magnet,* Science **323**, 915 (2009).

[5] X. Z. Yu, Y. Onose, N. Kanazawa, J. H. Park, J. H. Han, Y. Matsui, N. Nagaosa, and Y. Tokura, *Real-space observation of a two-dimensional skyrmion crystal,* Nature **465**, 901 (2010).

[6] C. Pappas, E. Lelièvre-Berna, P. Bentley, P. Falus, P. Fouquet, and B. Farago, *Magnetic fluctuations and correlations in MnSi: Evidence for a chiral skyrmion spin liquid phase,* Phys. Rev. B **83**, 224405 (2011).

[7] T. Adams, S. Mühlbauer, C. Pfleiderer, F. Jonietz, A. Bauer, A. Neubauer, R. Georgii, P. Böni, U. Keiderling, K. Everschor, M. Garst, and A. Rosch, *Long-Range Crystalline Nature of the Skyrmion Lattice in MnSi,* Phys. Rev. Lett. **107**, 217206 (2011).

[8] A. Tonomura, X. Yu, K. Yanagisawa, T. Matsuda, Y. Onose, N. Kanazawa, H. S. Park, and Y. Tokura, *Real-Space Observation of Skyrmion Lattice in Helimagnet MnSi Thin Samples,* Nano Lett. **12**, 1673 (2012).

[9] X. Z. Yu, N. Kanazawa, Y. Onose, K. Kimoto, W. Z. Zhang, S. Ishiwata, Y. Matsui, and Y. Tokura, *Near room-temperature formation of a skyrmion crystal in thin-films of the helimagnet FeGe,* Nat Mater **10**, 106 (2010).

[10] H. Wilhelm, M. Baenitz, M. Schmidt, U. K. Rößler, A. A. Leonov, and A. N. Bogdanov, *Precursor Phenomena at the Magnetic Ordering of the Cubic Helimagnet FeGe,* Phys. Rev. Lett. **107**, 127203 (2011).

[11] E. Moskvin, S. Grigoriev, V. Dyadkin, H. Eckerlebe, M. Baenitz, M. Schmidt, and H. Wilhelm, *Complex Chiral Modulations in FeGe Close to Magnetic Ordering,* Phys. Rev. Lett. **110**, 077207 (2013).

[12] K. Shibata, X. Z. Yu, T. Hara, D. Morikawa, N. Kanazawa, K. Kimoto, S. Ishiwata, Y. Matsui, and Y. Tokura, *Towards control of the size and helicity of skyrmions in helimagnetic alloys by spin-orbitcoupling,* Nature Nanotechnology **8**, 723 (2013).

[13] S. V. Grigoriev, N. M. Potapova, S. A. Siegfried, V. A. Dyadkin, E. V. Moskvin, V. Dmitriev, D. Menzel, C. D. Dewhurst, D. Chernyshov, R. A. Sadykov, L. N. Fomicheva, and A. V. Tsvyashchenko, *Chiral Properties of Structure and Magnetism in $Mn_{1-x}Fe_xGe$ Compounds: When the Left and the Right are Fighting, Who Wins?* Phys. Rev. Lett. **110**, 207201 (2013).

[14] W. Münzer, A. Neubauer, T. Adams, S. Mühlbauer, C. Franz, F. Jonietz, R. Georgii, P. Böni, B. Pedersen, M. Schmidt, A. Rosch, and C. Pfleiderer, *Skyrmion lattice in the doped semiconductor $Fe_{1-x}Co_xSi$,* Phys. Rev. B **81**, 041203(R) (2010).

[15] D. Morikawa, K. Shibata, N. Kanazawa, X. Z. Yu, and Y. Tokura, *Crystal chirality and skyrmion helicity in MnSi and (Fe, Co) Si as determined by transmission electron microscopy,* Phys. Rev. B **88**, 024408 (2013).

[16] P. Milde, D. Kohler, J. Seidel, L. M. Eng, A. Bauer, A. Chacon, J. Kindervater, S. Mühlbauer, C. Pfleiderer, S. Buhrandt, C. Schutte, and A. Rosch, *Unwinding of a Skyrmion Lattice by Magnetic Monopoles,* Science **340**, 1076 (2013).

[17] S. Seki, X. Z. Yu, S. Ishiwata, and Y. Tokura, *Observation of Skyrmions in a Multiferroic Material,* Science **336**, 198 (2012).

[18] S. Seki, J. H. Kim, D. S. Inosov, R. Georgii, B. Keimer, S. Ishiwata, and Y. Tokura, *Formation and rotation of skyrmion crystal in the chiral-lattice insulator Cu_2OSeO_3,* Phys. Rev. B **85**, 220406(R) (2012).

[19] T. Adams, A. Chacon, M. Wagner, A. Bauer, G. Brandl, B. Pedersen, H. Berger, P. Lemmens, and C. Pfleiderer, *Long-Wavelength Helimagnetic Order and Skyrmion Lattice Phase in Cu_2OSeO_3,* Phys. Rev. Lett. **108**, 237204 (2012).

[20] P. Bak and M. H. Jensen, *Theory of helical magnetic structures and phase transitions in MnSi and FeGe,* J. Phys. C: Solid State Phys. **13**, L881 (1980).

[21] V. Dyadkin, K. Prša, S. V. Grigoriev, J. S. White, and P. Huang, *Chirality of structure and magnetism in the magnetoelectric compound Cu_2OSeO_3,* Phys. Rev. B **89**, 140409(R) (2014).

2

EXPERIMENTAL TECHNIQUES

All samples investigated in this thesis were single crystals that have been provided by collaborators. The Cu_2OSeO_3 and FeGe samples used for neutron scattering were grown with chemical vapour transport method and were provided by dr. M. Schmidt and dr. M. Baenitz from the Max Planck Institute for Chemical Physics of Solids in Dresden, Germany. The Cu_2OSeO_3 samples used for DC magnetisation and AC susceptibility measurements were produced with the same method [1, 2] by A. Aqeel and T.T.M Palstra at the Zernike Institute for Advanced Materials, Groningen University. The MnSi sample was cut from a large single crystal grown by the Bridgman technique [3] at Ames Laboratory, USA. This chapter will present briefly the experimental techniques employed in this thesis: DC magnetization, AC susceptibility, Small Angle Neutron Scattering, Neutron polarimetry and Neutron Spin Echo spectroscopy.

2.1. DC MAGNETISATION AND AC SUSCEPTIBILITY

Bulk magnetisation measurements were performed with a Quantum Design MPMS-5XL superconducting quantum interference device (SQUID) magnetometer [4] at TU Delft. The temperature range of the SQUID spans from ~ 2 K up to 300 K, and the DC vertical magnetic field B can be varied between -5 T and 5 T. An additional vertical AC field B_{ac} with a maximum amplitude of 4 mT can be applied superimposed to the DC field for the AC susceptibility measurements. These were performed at a frequency range covering from 0.1 to 1000 Hz and provided both the real or in-phase component of the susceptibility χ', and the imaginary or out-of-phase component χ''.

The samples were positioned in a capsule and amounted at the bottom of a

sample rod, which was introduced in the cryostat and the SQUID. Both the DC magnetisation and the AC magnetic susceptibility measurements were carried out using a standard extraction method and by moving the sample along the vertical direction between four pick-up coils [4], as illustrated in Fig. 2.1. The coils are winded in a manner that the currents at the top and bottom flow oppositely to those in the middle two coils, and the response of the sample is a symmetric waveform. The magnetisation M of the sample is obtained through the integration of this waveform and thus is enhanced with four pick-up coils. The temperatures were varied stepwise and all measurements were performed once the samples reached thermal equilibrium.

The magnetisation M of a sample induces a demagnetising field B_{dem} that is opposite to the applied external magnetic field B_{ext}, and in SI unit is given as: $B_{dem} = D\mu_0 M$. The demagnetisation factor D depends on the sample shape and is homogenous through the sample only in the case of a perfect ellipsoid shape [5]. For a spherical shaped sample, $D = 1/3$. The demagnetising field leads to a reduced internal magnetic field:

$$\vec{B}_{int} = \vec{B}_{ext} - \vec{B}_{dem} = \vec{B}_{ext} - D\mu_0\vec{M} \tag{2.1}$$

and modifies the (scalar) susceptibility:

$$\frac{dB_{int}}{dM} = \frac{dB_{ext}}{dM} - D\mu_0 \tag{2.2}$$

$$\frac{1}{\chi_{int}} = \frac{1}{\chi_{ext}} - D\mu_0 \tag{2.3}$$

$$\chi_{int} = \frac{\chi_{ext}}{1 - D\mu_0\chi_{ext}} \tag{2.4}$$

In case of samples with non-ellipsoid shapes and irregular surfaces, the magnitude and even the direction of the internal magnetic field is not homogenous through the samples. This has also been the case for the single-crystalline samples investigated in this thesis, where the effect of this correction will be addressed.

2.2. NEUTRON SCATTERING

Neutrons are charge-less particles with spin 1/2, which penetrate deeply in the materials and interact directly with the local magnetic fields. For this reason, they are a powerful source for investigating magnetic correlations in the bulk of materials.

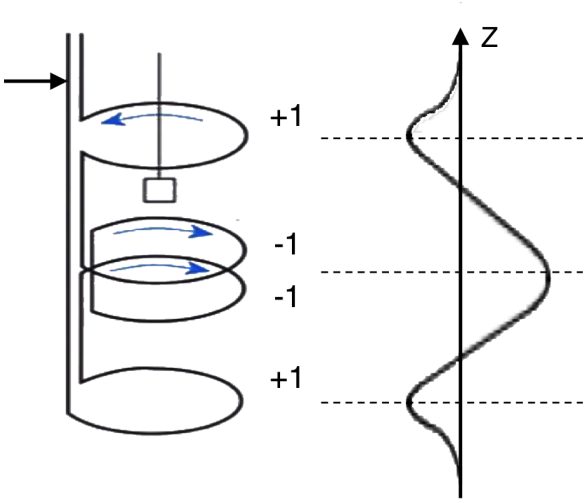

Figure 2.1: Configuration of the pick-up coils and the typical sample response profile at SQUID [4].

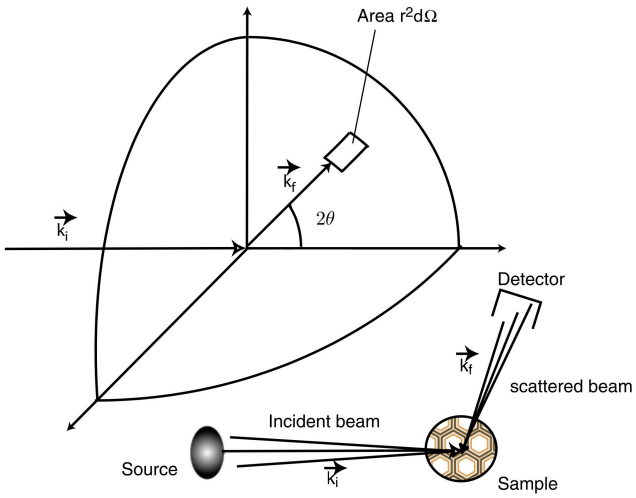

Figure 2.2: Geometry of a scattering experiment after [6].

In a neutron scattering measurement, an incident neutron beam, with a wavevector $\vec{k}_i$ and energy E_i is scattered by a sample, where momentum and energy transfer occur, so that the scattered beam has a wavevector $\vec{k}_f$ and energy E_f. The observable quantity is a cross section, which defines the probability of neutrons being scattered along a specific direction, deviating by the scattering angle 2θ from the incident beam, into a solid angle $d\Omega$ and with energies between E_f and $E_f + dE_f$, as schematically illustrated in Fig. 2.2. The neutron scattering cross section is expressed in the Born approximation as [7]:

$$\frac{d^2\sigma}{d\Omega dE_f} = \frac{k_f}{k_i}\left(\frac{m}{2\pi\hbar^2}\right)^2 |\langle k_f\sigma_f\lambda_f|V|k_i\sigma_i\lambda_i\rangle|^2\delta(\hbar\omega + E_{\lambda i} - E_{\lambda f}) \tag{2.5}$$

where m is the mass of the neutron , V the interaction potential between sample and neutrons, σ_i and σ_f the spin state of the incident and scattered neutrons respectively, and finally $E_{\lambda i}$ and $E_{\lambda f}$ the initial and final energies of the sample in the eigenstates $|\lambda_i\rangle$ and $|\lambda_f\rangle$ respectively. The conservation of energy and momentum leads to:

$$\hbar\omega = E_f - E_i = \frac{\hbar^2}{2m}(k_f^2 - k_i^2) \tag{2.6}$$

$$\vec{Q} = \vec{k}_f - \vec{k}_i \tag{2.7}$$

with $\hbar\omega$ the energy transfer and $\vec{Q}$ the scattering vector. For elastic scattering, $\hbar\omega$ is zero, and the modulus of the scattering vector can be expressed as:

$$|\vec{Q}| = \frac{4\pi\,\sin\theta}{\lambda} \tag{2.8}$$

with λ the neutron beam wavelength.

Nuclear scattering originates from the strong nuclear force between the neutrons and the nuclei, whereas magnetic scattering is caused by the magnetic dipole-dipole interaction between the magnetic moment of neutrons and the local magnetic fields in the sample. The vector properties of the magnetic dipole-dipole interaction are reflected in the scattering cross section of neutrons, which as it will be discussed below may also depend on the polarisation of the incident neutron beam and the chiral magnetic character of the sample.

The scattering by the nucleus or magnetic atoms is an interference phenomenon as illustrated in Fig. 2.3, which shows interference patterns produced by plane wave scattering from two particles that are separated by a distance d. The waves are spherically symmetric and interfere with each other, leading to constructive and destructive interference. These interference patterns are the Fourier transform of the real space arrangement of the particles. For larger distance between the particles, the constructive interference occurs at smaller angles. For

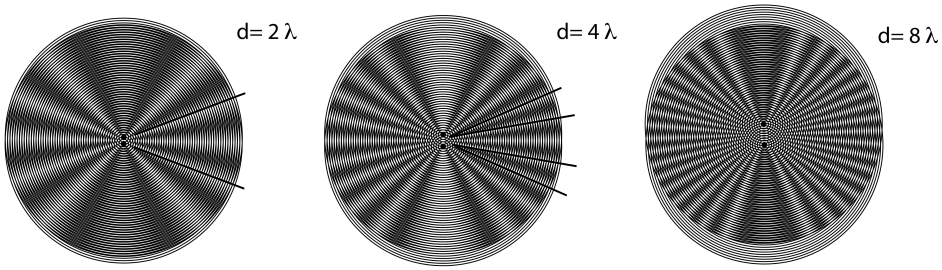

Figure 2.3: Illustration of the interference patterns between two particles that are separated by various distances d with respect to the wavelength λ of the beam, after [6].

this reason, large-scale correlations, typically in a length scale between 1 and 1000 nm, are probed by small angle scattering. This is also the case for helimagnetic correlations with typical modulations between 3 and 100 nm.

2.2.1. SMALL ANGLE NEUTRON SCATTERING

A schematic illustration of the small angle neutron scattering (SANS) geometry is given in Fig. 2.4. A white neutron beam from the reactor is transferred to the sample via neutron guides, monochromatized by a velocity selector and collimated by pin-hole collimators. After the sample the scattered neutrons are detected by a position sensitive 2D detector, while those transmitted are absorbed by a beam stop.

The SANS measurements that are part of this thesis were performed at PAXY and PA20 of the Laboratoire Léon Brillouin, Saclay, France, and at IN15, which is also a neutron spin echo (NSE) spectrometer at the Institut Laue Langevin, France. The wavelength spread $\Delta\lambda/\lambda$ was $\sim 10\% - 15\%$ determined by the velocity selector, and the beam divergence $\Delta\theta$ approximated $\sim 0.02^\circ$ FWHM at PAXY and PA20, and $\sim 0.28^\circ$ FWHM at IN15. The detector had dimensions of 64×64 cm^2 with a pixel resolution of 0.5×0.5 cm^2 at PAXY and PA20, and dimensions of 32×32 cm^2 with a pixel resolution of 1×1 cm^2 at IN15. For all instruments, an orange-type cryostat was used for controlling the sample temperature between ~ 2 K and 300 K with an accuracy of 0.01 K. A horizontal cryomagnet was installed at the sample position when necessary.

2.2.2. NEUTRON POLARIMETRY

Following the Blume-Maleyev equations [10], the magnetic cross section and the scattered beam polarisation $\vec{P}_f$ are expressed as:

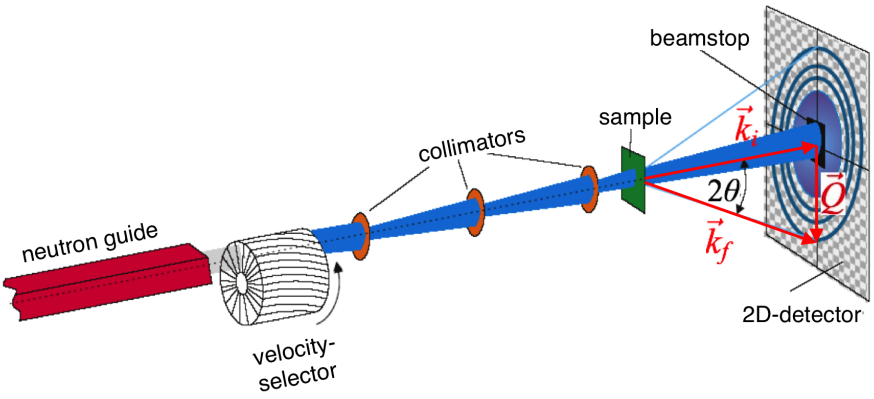

Figure 2.4: Schematic representation of small angle neutron scattering geometry after [8] and [9]. $\vec{k}_i$ and $\vec{k}_f$ are the incident and scattered beam, respectively, and $\vec{Q}$ is the scattering vector $\vec{Q} = \vec{k}_f - \vec{k}_i$.

$$\sigma(\vec{Q}) = \vec{M}_\perp \vec{M}_\perp^\star + \vec{P} \cdot \Im(\vec{M}_\perp \times \vec{M}_\perp^\star) \tag{2.9}$$

$$\vec{P}_f \sigma(\vec{Q}) = -\vec{P}(\vec{M}_\perp \vec{M}_\perp^\star) + 2\Re[(\vec{P} \cdot \vec{M}_\perp^\star)\vec{M}_\perp] - \Im(\vec{M}_\perp \times \vec{M}_\perp^\star) \tag{2.10}$$

where $\vec{P}$ is the polarisation of the incident neutron beam, and $\vec{M}_\perp$ is the magnetic interaction vector expressed as $\vec{M}_\perp = \vec{Q} \times (\vec{M}(\vec{Q}) \times \vec{Q})$ with $\vec{M}(\vec{Q})$ the Fourier transform of the magnetic correlation function. Thus the magnetic neutron scattering is only sensitive to those magnetic components that are perpendicular to the scattering vector $\vec{Q}$. For this reason, it is always "spin-flip", i.e. it changes the sign of the incoming beam polarisation, when this is along $\vec{Q}$. In order to account for the vector properties of the magnetic scattering, in the following a right-handed Cartesian set will be introduced with $\hat{x} \parallel \vec{Q}$, $\hat{z}$ in the scattering plane and $\hat{y}$ completing the Cartesian set. In the SANS geometry considered here, $\hat{y}$ becomes collinear to $\vec{k}_i$.

The scattering cross section in Eq. 2.9 comprises the scalar product $\vec{M}_\perp \vec{M}_\perp^\star$ and a second term that is non-zero only for a polarised incident neutron beam and chiral correlations. The vector product $\Im(\vec{M}_\perp \times \vec{M}_\perp^\star)$ is parallel or antiparallel to the scattering vector $\vec{Q}$ depending on the sign of the chirality ζ, positive ($\zeta = +1$) for right-handed and negative ($\zeta = -1$) for left-handed. This component contributes constructively to the scattering cross section for $\vec{P} \parallel \Im(\vec{M}_\perp \times \vec{M}_\perp^\star)$ and destructively for $\vec{P} \parallel -\Im(\vec{M}_\perp \times \vec{M}_\perp^\star)$, as illustrated by the typical half-moon scattering patterns in Fig. 2.5 for the archetype chiral magnet MnSi [11]. It can then

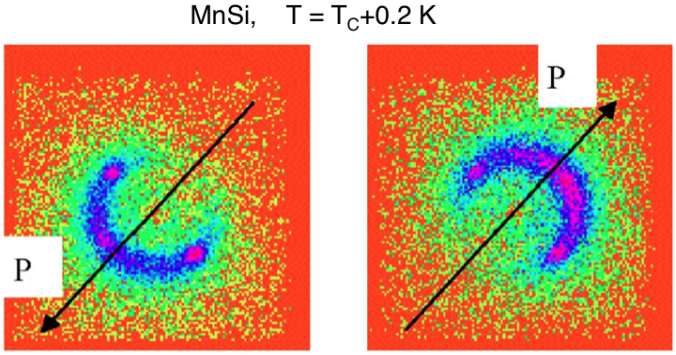

Figure 2.5: Typical neutron scattering pattern for MnSi at $T = T_C + 0.2$ K for two opposite incoming beam polarisations, after [11].

be determined from the scattering cross sections with opposite incoming polarisations.

$$\sigma^{SF}_{\vec{P}\parallel\vec{Q}}(\vec{Q}) = \sigma_{+x,-x} = \vec{M}_\perp \vec{M}^\star_\perp + \zeta \cdot |\vec{P}| \cdot |\Im(\vec{M}_\perp \times \vec{M}^\star_\perp)| \tag{2.11}$$

$$\sigma^{SF}_{\vec{P}\parallel-\vec{Q}}(\vec{Q}) = \sigma_{-x,+x} = \vec{M}_\perp \vec{M}^\star_\perp - \zeta \cdot |\vec{P}| \cdot |\Im(\vec{M}_\perp \times \vec{M}^\star_\perp)| \tag{2.12}$$

The difference between the two cross sections leads to $|\Im(\vec{M}_\perp \times \vec{M}^\star_\perp)|$ and their sum to $\vec{M}_\perp \vec{M}^\star_\perp$. Therefore the chirality is given by [12]:

$$\zeta \cdot \eta(\vec{Q}) = \zeta \cdot \frac{|\Im(\vec{M}_\perp \times \vec{M}^\star_\perp)|}{\vec{M}_\perp \vec{M}^\star_\perp} = \frac{1}{|\vec{P}|} \cdot \frac{\sigma_{+x,-x} - \sigma_{-x,+x}}{\sigma_{+x,-x} + \sigma_{-x,+x}} \tag{2.13}$$

The scattered beam polarisation is given by Eq. 2.10. The first two terms lead to $-\hat{Q}(\hat{Q} \cdot \vec{P})$ for isotropically distributed magnetic moments, where $\hat{Q}$ is the unit vector of $\vec{Q}$. The third chiral term $\vec{M}_\perp \times \vec{M}^\star_\perp$ creates polarisation along the scattering vector $\vec{Q}$, parallel or anitparallel depending on the sign of the chirality, and independently of the incoming beam polarisation $\vec{P}$. A general form of Eq. 2.10 can be written as [13]:

$$\mathbb{P}_{i,j} = \frac{\tilde{P}_{i,j} P_i + P^\dagger_j}{|\vec{P}_f|} \tag{2.14}$$

with $P^\dagger_j$ the created polarisation and $(i, j) \in (x, y, z)$.

In the case of an ideal paramagnet, the scattered beam polarisation becomes $\vec{P}_f = -\hat{Q}(\hat{Q} \cdot \vec{P})$, thus only when the incoming beam polarisation $\vec{P}$ is along $\vec{Q}$ or

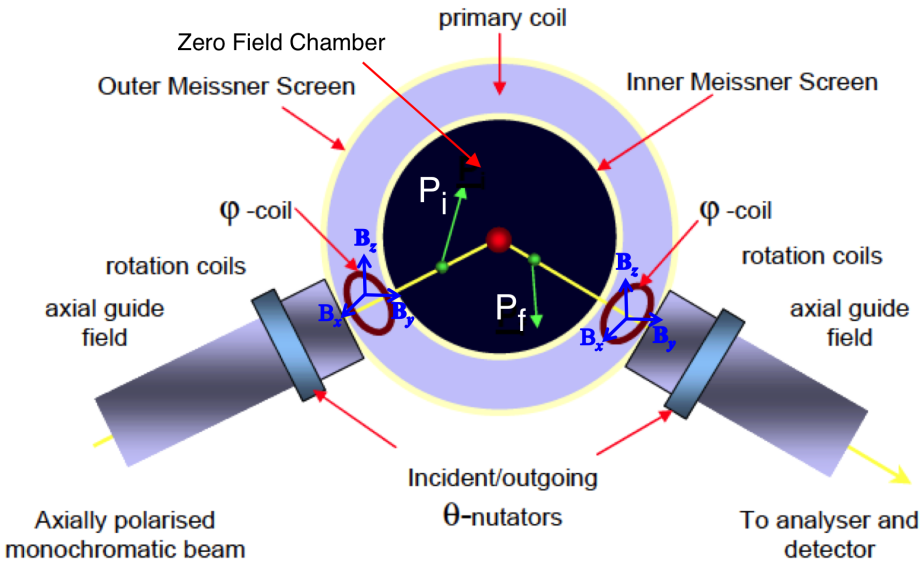

Figure 2.6: Schematic illustration of the Cryogenic Polarisation Analysis Device (Cryopad) after [14].

$\hat{x}$, the scattered beam is polarised and undergoes a change of sign. As a result, the polarisation matrix is:

$$\mathbb{P}_{\text{para}} = \begin{vmatrix} -1 & 0 & 0 \\ 0 & 0 & 0 \\ 0 & 0 & 0 \end{vmatrix}$$

The presence of a chiral term creates polarisation along $\vec{Q}$ or $\hat{x}$ independently of the incoming beam polarisation, leading to the matrix:

$$\mathbb{P}_{\text{chiral}} = \begin{vmatrix} -1 & \zeta\eta & \zeta\eta \\ 0 & 0 & 0 \\ 0 & 0 & 0 \end{vmatrix}$$

A complete analysis of the scattered beam polarisation along the three directions (x, y and z) independently of the incoming beam polarisation is possible by spherical neutron polarimetry (SNP) [12, 14], which analyses all components in the polarisation matrix and complements the classical polarisation analysis that provides only the diagonal xx, yy and zz components [15]. For this purpose, a zero-field chamber [12, 14] is introduced around the sample , as illustrated in Fig. 2.6. By using superconducting Meissner shields, $B < 1$ mG is obtained in

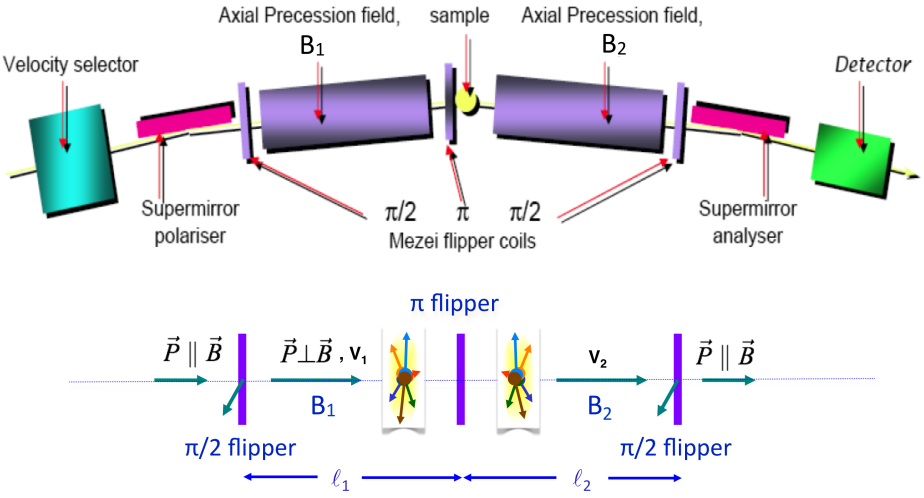

Figure 2.7: Schematic illustration of a Neutron Spin Echo Spectrometer after [16].

the chamber. The incoming and the scattered beam polarisations are tuned independently from each other through the nutators, which can adiabatically rotate the polarisations along x, y or z directions at the two sides of the zero-field sample chamber. The third generation Cryogenic Polarisation Analysis Device (Cryopad) [14] is illustrated in Fig. 2.6 and has been installed on IN15 for the experiments presented in this thesis.

2.2.3. NEUTRON SPIN ECHO SPECTROSCOPY

Neutron spin echo (NSE) spectroscopy reaches the highest resolution in inelastic neutron spectroscopy, and can measure energy transfers of some *n*eV. For this purpose it uses the Larmor precession of the neutron beam polarization in a magnetic field before and after the sample [16, 17].

A schematic illustration of an NSE spectrometer is given in Fig. 2.7, including several flippers and two precession arms that are designed to satisfy $B_1\ell_1 = B_2\ell_2$ with B_1 and B_2 the magnetic fields and ℓ_1 and ℓ_2 the lengths, of the two precession arms, respectively. The incoming neutrons with a velocity v_1 are polarised parallel to the magnetic field. The first $\pi/2$ flipper marks the beginning of the Larmor precession by turning the neutron polarisation vector over 90°, thus perpendicular to the magnetic field. The motion of the neutron polarisation vector

$\vec{P}$ with respect to the magnetic field $\vec{B}$ is given by:

$$\frac{d\vec{P}}{dt} = -\gamma_n \vec{P} \times \vec{B} = \vec{P} \times \vec{\omega}_L \tag{2.15}$$

with γ_n the gyromagnetic ratio of neutrons and $\omega_L = -\gamma B$ the Larmor precession frequency. The resulting precession angle at the first arm is $\phi_1 = \omega_L \ell / v_1$ and at the second arm $\phi_2 = \omega_L \ell / v_2$ with v_2 being the neutron velocity after the sample.

A π flipper is placed at the symmetry point of the setup to mirror the precession at the second arm. So, in the absence of sample and for elastic scattering where $v_1 = v_2$, the total precession angle is $\phi = \phi_1 - \phi_2 = 0$ and the neutron beam recovers its initial state at the second $\pi/2$ flipper. The symmetry of the setup is broken by inelastic scattering at the sample, and the energy transfer at the limit of small changes can be expressed as:

$$\hbar\omega = m/2 \cdot (v_2^2 - v_1^2) = m/2 \cdot (v_2 + v_1)(v_2 - v_1) \approx m \cdot v\Delta v \tag{2.16}$$

with $(v_2 + v_1)/2 = v$ and $v_2 - v_1 = \Delta v$.

In this case, the total precession angle between the two arms becomes:

$$\phi = \phi_1 - \phi_2 = \omega_L \ell (1/v_1 - 1/v_2) \approx \omega_L \ell \Delta v / v^2 \tag{2.17}$$

Invoking eq. 2.16,

$$\phi \approx \omega_L \ell \Delta v / v^2 = \frac{\hbar \omega_L \ell}{m v^3} \omega = \omega t \tag{2.18}$$

with $t = \hbar\omega_L \ell / m v^3$ the spin-echo time.

At the analyser, the spin echo polarisation vector is projected along the direction of the magnetic field, which is the quantisation axis, leading to the observable:

$$P_{NSE} = \langle cos(\phi) \rangle = \langle cos(\omega t) \rangle \tag{2.19}$$

where $\langle ... \rangle$ averages the probability of the scattering with energy transfer $\hbar\omega$.

The relation between the scattered beam polarisation and the scattered intensity $S(Q,\omega)$ measured at the detector is then given by [12, 16]:

$$P_{NSE} = \frac{\int S(Q,\omega) cos(\omega t) d\omega}{\int S(Q,\omega) d\omega} = I(Q,t) \tag{2.20}$$

where $I(Q,t)$ is the intermediate scattering function.

In the presence of a magnetic sample, the magnetic scattering from the sample acts as a π flipper, and for this reason no π flipper is required at the sample position. This configuration corresponds to the paramagnetic NSE [16], which

was used for the NSE measurements performed for this thesis. These were carried out at the high-resolution NSE spectrometer IN15 of the Institut Laue Langevin in Grenoble, France.

REFERENCES

[1] J.-W. G. Bos, C. V. Colin, and T. T. M. Palstra, *Magnetoelectric coupling in the cubic ferrimagnet Cu_2OSeO_3*, Phys. Rev. B **78**, 094416 (2008).

[2] A. Aqeel, J. Baas, G. R. Blake, and T. T. M. Palstra, *Growth and helicity of non-centrosymmetric Cu_2OSeO_3 crystals,* unpublished (2017).

[3] S. M. Stishov, A. E. Petrova, S. Khasanov, G. K. Panova, A. A. Shikov, J. C. Lashley, D. Wu, and T. A. Lograsso, *Magnetic phase transition in the itinerant helimagnet MnSi: Thermodynamic and transport properties,* Phys. Rev. B **76** (2007).

[4] *Brochure for Physical Property Measurement System.* (Technical report, Quantum Design, www.qdusa.com, 2003).

[5] J. A. Osborn, *Demagnetizing factors of the general ellipsoid,* Phys. Rev. **67**, 351 (1945).

[6] H. Schober, *An introduction to the theory of nuclear neutron scattering in condensed matter,* Journal of Neutron Research **17**, 109 (2014).

[7] G. L. Squires, *Introduction to the Theory of Thermal Neutron Scattering; 3rd ed.* (Cambridge University Press, Cambridge, 1978).

[8] W. Wagner and J. Kohlbrecher, *Modern Techniques for Characterizing Magnetic Materials* (ed Y Zhu, Boston: Kluwer, 2005) pp. 65–103.

[9] A. Michels and J. Weissmüller, *Magnetic-field-dependent small-angle neutron scattering on random anisotropy ferromagnets,* Reports on progress in physics **71**, 066501 (2008).

[10] M. Blume, *Polarization effects in the magnetic elastic scattering of slow neutrons,* Physical review **130**, 1670 (1963).

[11] S. Grigoriev, S. Maleyev, A. Okorokov, Y. Chetverikov, R. Georgii, P. Böni, D. Lamago, H. Eckerlebe, and K. Pranzas, *Critical fluctuations in MnSi near T_C: A polarized neutron scattering study,* Phys. Rev. B **72**, 134420 (2005).

[12] C. Pappas, E. Lelièvre-Berna, P. Bentley, P. Falus, P. Fouquet, and B. Farago, *Magnetic fluctuations and correlations in MnSi: Evidence for a chiral skyrmion spin liquid phase,* Phys. Rev. B **83**, 224405 (2011).

[13] P. J. Brown, *Polarised neutrons and complex antiferromagnets: an overview,* Physica B: Physics of Condensed Matter **297**, 198 (2001).

[14] F. Tasset, P. J. Brown, E. Lelièvre-Berna, T. Roberts, S. Pujol, J. Allibon, and E. Bourgeat-Lami, *Spherical neutron polarimetry with Cryopad-II,* Physica B: Physics of Condensed Matter **267**, 69 (1999).

[15] O. Schärpf, *The Spin of the Neutron as a Measuring Probe,* Institut Max von Laue–Paul Langevin (1996).

[16] F. Mezei, *Neutron Spin Echo*, Lecture Notes in Phys. Ser., vol. 601 (Springer-Verlag, Heidelberg, 1980).

[17] C. Pappas, E. Lelièvre-Berna, P. Falus, B. Farago, P. Bentley, E. Moskvin, T. Krist, and S. Grigoriev, *Challenges in neutron spin echo spectroscopy,* Physica B: Physics of Condensed Matter **404**, 2578 (2009).

3

MAGNETIC RELAXATION PHENOMENA IN Cu_2OSeO_3 AND PHASE DIAGRAM CLOSE TO T_C

We present an investigation of the magnetic field-temperature phase diagram of Cu_2OSeO_3 based on DC magnetisation and AC susceptibility measurements covering a broad frequency range of four orders of magnitude, from very low frequencies reaching 0.1 *Hz up to* 1 *kHz. The experiments were performed in the vicinity of $T_C = 58.2$ K and around the skyrmion lattice A-phase. At the borders between the different phases the characteristic relaxation times reach several milliseconds and the relaxation is non-exponential. Consequently the borders between the different phases depend on the specific criteria and frequency used and an unambiguous determination is not possible.*

This chapter has been published in Phys. Rev. B **94**, 064418 (2016) [1].

3.1. INTRODUCTION

In noncentrosymmetric magnetic materials Dzyaloshinsky-Moriya (DM) interactions [2, 3] can stabilize 2D and 3D modulations with a fixed sense of rotation of the magnetization vector. These *chiral skyrmions* [4–7] in form of axisymmetric strings have been found both in real and reciprocal space in a number of cubic helimagnets with B20 structure, such as MnSi [8, 9], FeGe [10–12], $Fe_{1-x}Co_xSi$ [13–15] in the so called A-phase. This is a closed pocket of the magnetic field (B) - temperature (T) phase diagram. The recent discovery of similar behaviour in the insulator and multiferroic Cu_2OSeO_3 [16–18] has attracted attention also because in this system it is possible to manipulate skyrmions by external electric fields [19, 20].

Cu_2OSeO_3 crystallizes in the non-centrosymmetric space group $P2_13$, the same as for the B20 compounds, but with two different Cu^{2+} ion sites [21, 22], as shown in the inset of Fig. 3.1. The balance between the ferromagnetic exchange and the DM interactions leads to a long-period helical order with a pitch of ~ 60 nm [16, 18]. A weak anisotropy fixes the helices along the ⟨100⟩ crystallographic directions below the ordering temperature T_C, which is close to 58 K. A weak external magnetic field B may overcome the anisotropy, unpin the helices from the lattice and orient them along its direction leading to the conical phase if $B > B_{C1}$. Higher magnetic fields stabilize the A-phase pocket close to T_C and even higher magnetic fields are needed to overcome the DM interaction and the helical correlations inducing the field polarised phase, which sets-in for $B > B_{C2}$ [16, 18]. These features are summarised in Fig. 3.1, which schematically illustrates the spin arrangements of the various phases.

The phase diagram of Cu_2OSeO_3 has been investigated close to T_C by neutron scattering [16–18] and AC susceptibility for frequencies from 2.5 Hz to 1 kHz [23]. The DC magnetisation and AC susceptibility measurements presented in the following complement these previous studies. Our experiments span a very broad frequency range, from 0.1 Hz to 1 kHz, which extends the previous study [23] towards the low frequencies by more than one order of magnitude. The analysis of the results as a function of the magnetic field, instead of the temperature as in the previous study, provides a quantitative approach to the phase diagram. The dynamics at the transitions between the helical, conical and A-phases, at B_{C1}, B_{A1} and B_{A2}, involve a broad distribution of relaxation times with characteristic times reaching several milliseconds. Additional relaxation processes have also been found at very low frequencies and around B_{C1}. The borders between the different phases are discussed and we conclude that these are not sharp but their exact location depends on the specific criteria and the frequency used. Remarkably, no relaxation is found at the high and the low temperature boundaries

of the *A*-phase.

This chapter will present and discuss the experimental results at separate sections: experimental details, magnetization, AC susceptibility at a frequency of 0.8 Hz, frequency dependence, Cole-Cole analysis and finally the $B-T$ phase diagram.

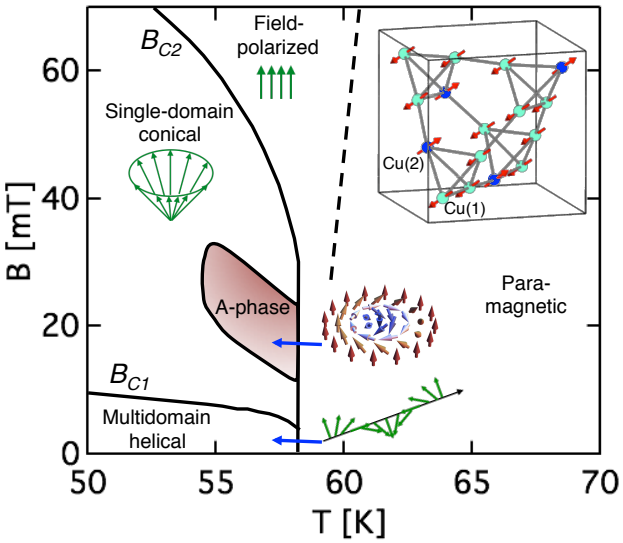

Figure 3.1: Schematic representation of the phase diagram of Cu_2OSeO_3 illustrating the spin arrangements of the various phases. The inset shows the crystal structure with the two different Cu^{2+} ion sites[21].

3.2. EXPERIMENTAL DETAILS

A high-quality single crystal of Cu_2OSeO_3 was grown by the chemical vapour transport method [24] and its structure was checked by X-ray diffraction. The sample with almost cubic shape was oriented with the ⟨001⟩ axis vertical within ±5°. The magnetization M and the real and imaginary components of the AC-susceptibility, χ' and χ'' respectively, were measured with a MPMS-XL Quantum design SQUID magnetometer using the extraction method. A DC magnetic field B was applied along the vertical direction and parallel to the drive AC field, B_{AC}, with $0 < B_{AC} \leq 0.4$ mT, within the frequency range $0.1 \leq f \leq 1000$ Hz. Frequency scans were performed with logarithmic steps for each B and after having checked that the AC susceptibility was independent of B_{AC}, the measurements were done for $B_{AC} = 0.4$ mT. For the measurements two specific experimental

protocols have been used:

- FC temperature scans: the sample was brought to 70 K, a magnetic field was applied and the signal was recorded with decreasing stepwise the temperature. At each temperature the sample was brought to thermal equilibrium before measurement.
- ZFC magnetic field scans: the sample was brought to the temperature of interest under zero field (more specifically the residual field of the magnetometer which was less than 1 mT). Once thermal equilibrium was reached the measurements were performed by increasing stepwise the magnetic field.

3.3. MAGNETIZATION

Figure 3.2 displays the ZFC magnetization M and the susceptibility $\Delta M/\Delta B$, derived by numerical differentiation of the M vs B curves. The same set of data has been plotted either versus the magnetic field for selected temperatures (a and c) or versus the temperature for selected magnetic fields (b and d) in order to better emphasise the occurring phase transitions. The magnetisation curves in panels (a) and (b) highlight the transition from the paramagnetic to the helical phase around 58 K, seen both in the strong non-linearities of M versus B for $56\,\text{K} \lesssim T \lesssim 59\,\text{K}$ (a) and the onset of a plateau at the M versus T plots (b). The M vs B plots give only a coarse overview and the effects related with the onset of the A-phase, are only brought out by the $\Delta M/\Delta B$ curves, which show clear dips at $56\,\text{K} \lesssim T \lesssim 58\,\text{K}$ and $15\,\text{mT} \lesssim B \lesssim 30\,\text{mT}$. Thus the relevant features are seen on $\Delta M/\Delta B$ and show up with much higher accuracy on the AC susceptibility which will be discussed in the following sections.

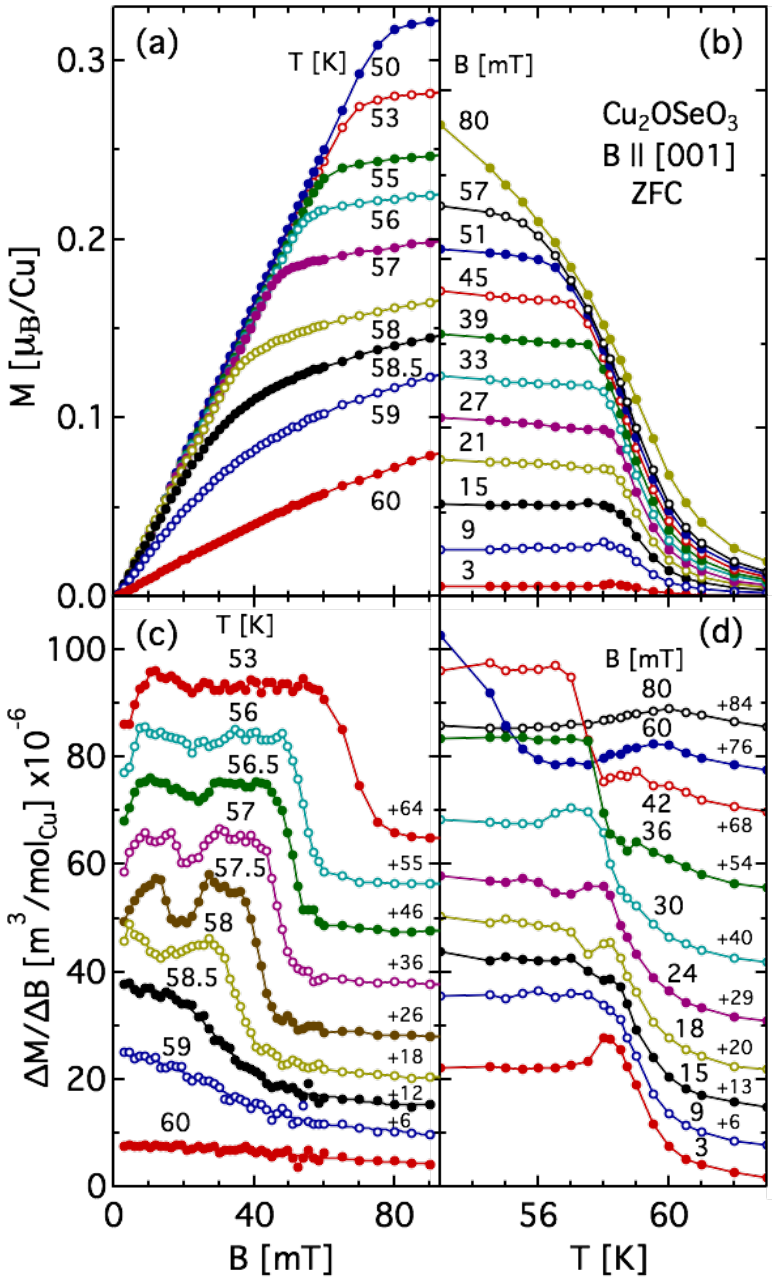

Figure 3.2: ZFC magnetization of Cu_2OSeO_3 as a function of temperature and magnetic field. The same set of data has been plotted versus the magnetic field for selected temperatures (a) and versus the temperature for selected magnetic fields (b). The susceptibility $\Delta M/\Delta B$ deduced by numerical differentiation of the M vs B curves is shown as a function of the magnetic field in (c) and of temperature in (d). For the sake of clarity the curves in (c) and (d) have been shifted vertically with respect to the baseline by the values indicated.

3.4. AC SUSCEPTIBILITY AT 0.8 HZ

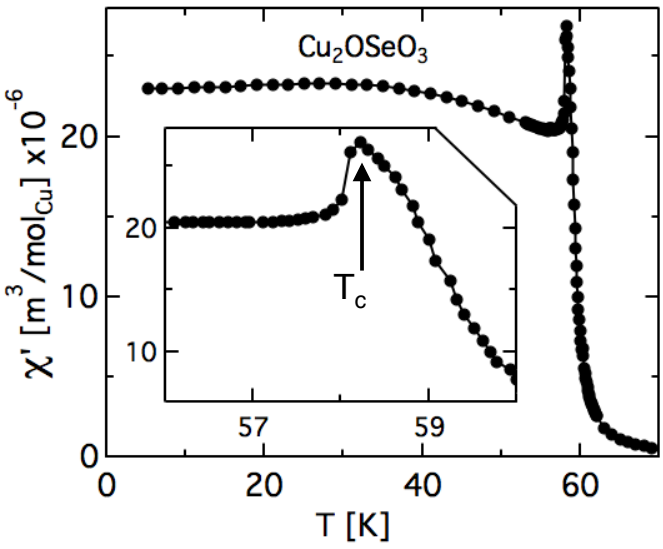

Figure 3.3: Temperature dependence of χ' of Cu_2OSeO_3 for $B = 0$ mT and $f = 0.8$ Hz. The inset shows a close-up around the peak, which marks the onset of the helical order and reveals an asymmetric shape with a shoulder above $T_C = 58.20 \pm 0.05$ K.

Figure 3.3(a) shows the temperature dependence of χ' measured at $B = 0$ mT and at a frequency of 0.8 Hz. For $B = 0$ mT and all frequencies used in this work χ' was frequency independent and $\chi'' = 0$. The peak at $T_C = 58.20 \pm 0.05$ K marks the transition to the helical state and the closer inspection shown in the inset reveals an asymmetric cusp-like shape with a shoulder at 59 ± 0.01 K, as reported before in Cu_2OSeO_3 [23, 25]. Similarly to MnSi [26] the shoulder marks the onset of the precursor phase [27], where helical correlations and fluctuations become predominant.

In the helical phase χ' varies non-monotonically showing a minimum at ~ 57 K and a broad maximum at about 30 K before levelling-off to $\sim 23 \cdot 10^{-6}$ m^3/mol_{Cu} below 10 K. This value is comparable to the one reported for a polycrystalline sample [21], where however a smoother temperature dependence with no clear peak at T_C has been found. On the other hand, the overall shape of χ' in Fig. 3.3 is similar to the one found for another single crystal along ⟨111⟩, where slightly lower absolute values have been reported possibly due to the different crystal orientations [28].

At low temperatures the magnetic response depends on the magnetic history of the sample. It has indeed been found that below 50 K FC and ZFC measurements give different results[21, 25]. For this reason we distinguished between FC or ZFC following the specific procedures described above. The results did not show any influence of the magnetic history on the susceptibility. Despite of that, for the sake of clarity, we will specify in the following the protocol used for each set of data.

Figure 3.4 shows the FC susceptibility, χ' (a and b) and χ'' (c and d), in the vicinity of T_C for selected values of B and reveals the strong influence of the magnetic field: the peak of χ', which has been associated with T_C at $B = 0$, shifts to lower temperatures whereas the high-temperature shoulder becomes more noticeable. At 12 mT $\lesssim B \lesssim$ 23 mT the shape of χ' changes dramatically: it shows two maxima separated by a minimum characteristic for the A-phase. By further increasing the magnetic field only one cusp remains and the shape becomes again similar to that of low fields. Much higher magnetic fields smoothen the cusp and χ' becomes almost temperature independent below ~ 58 K.

The magnetic field has a dramatic influence also on χ''. The weakest magnetic field (3 mT in our case) induces already a peak in χ'' slightly below T_C, which becomes more pronounced at 5 mT and transforms into a broad maximum upon further increasing the field. Between 14 and 17 mT the maximum becomes a strong and well defined cusp. By further increasing B, χ'' vanishes for 21 mT <B <23 mT but re-appears for B >23 mT before fading away at higher fields approaching B_{C2}.

A complementary view of the effect of temperature and magnetic field is given by Fig. 3.5, where the ZFC susceptibility is plotted versus the magnetic field for selected temperatures. Well above T_C, at 60.5 K, χ' is almost field independent and χ'' is practically zero. Lowering the temperature leads to a strong increase of the low field χ'. Furthermore, at T_C a non-monotonic behaviour develops with a minimum at B ~ 14 mT, which is characteristic for the A-phase. The minimum is most pronounced for 58 K $\gtrsim T \gtrsim$ 57 K and persists down to 55 K.

As already mentioned χ'' is zero for $T \geq T_C$ and for all frequencies used in this study. A peak first appears at 58 K centered at $B = 4$ mT and remains significant upon decreasing the temperature. At 57.8 K two additional maxima appear at the borders of the A-phase, which evolve to well defined peaks at 57 K and fade out at lower temperatures.

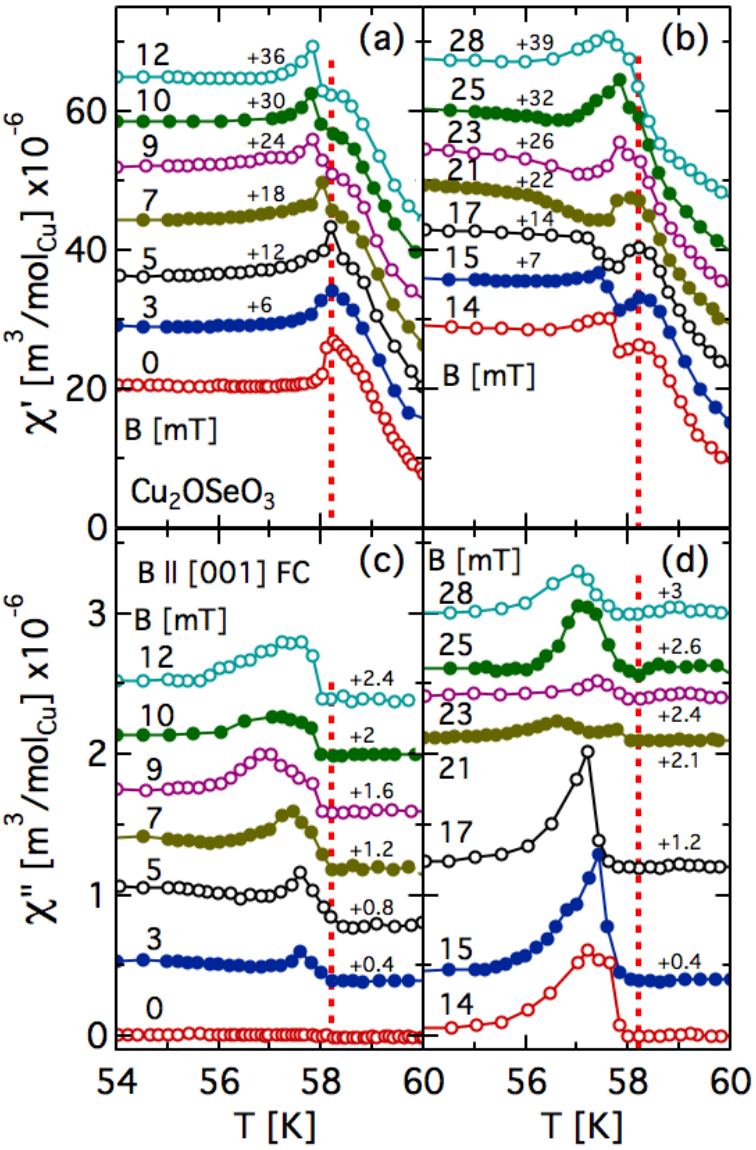

Figure 3.4: Temperature dependence of FC χ' (a and b) and χ'' (c and d), for different magnetic fields B and for $f = 0.8$ Hz. The vertical dashed lines indicate T_C for $B = 0$. For the sake of clarity the curves have been shifted vertically with respected to the base line by the numbers given next to each of them.

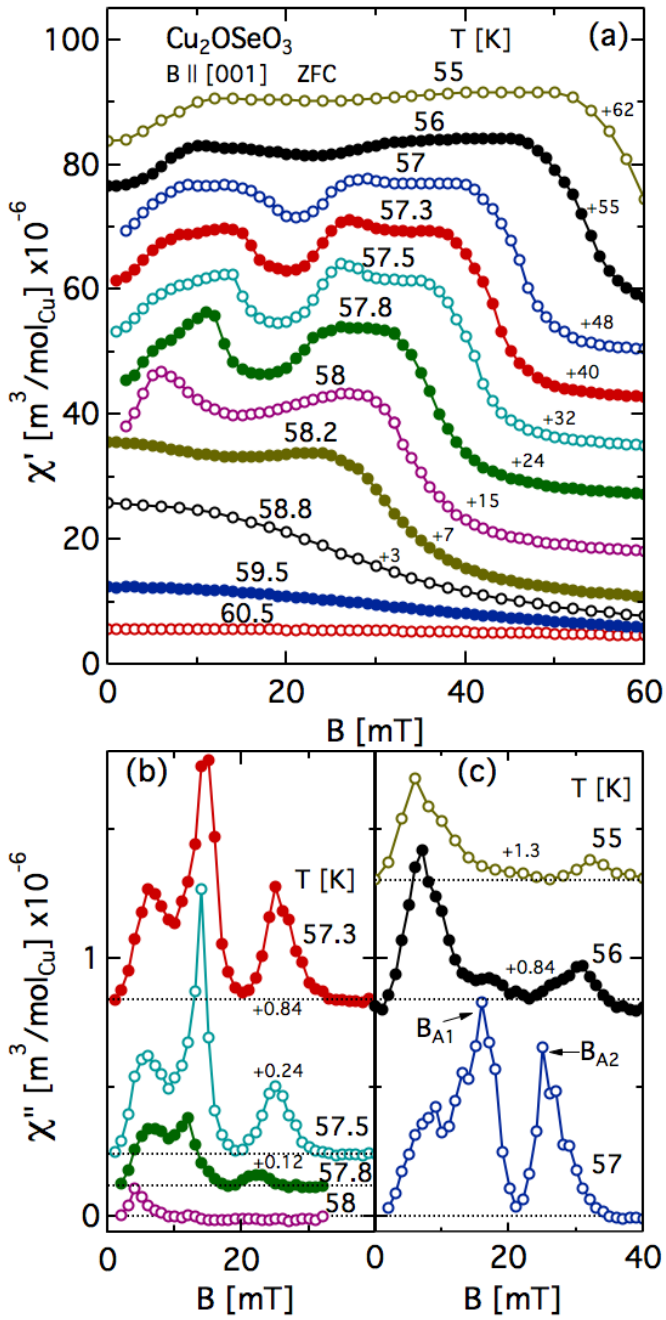

Figure 3.5: Magnetic field dependence of ZFC χ' (a) and χ'' (b and c) of Cu_2OSeO_3 for some selected temperatures and for $f = 0.8$ Hz. For the sake of clarity some curves have been vertically shifted with respect to the base line by the values indicated next to each of them.

Both χ' and χ'' bear the signature of the series of field-induced transitions characteristic of Cu_2OSeO_3 [18, 23, 29] and helimagnets of B20 types such as MnSi [8, 30] or FeGe [11, 12]. Below T_C the application of a magnetic field induces an initial increase of χ' related to the transition from the helical to the conical phases at the lower critical field B_{C1}. By further increasing the magnetic field at sufficiently low temperatures, for Cu_2OSeO_3 at $T < 55$ K, χ' remains constant until the upper critical field B_{C2}, where it decreases rapidly indicating the transition to the field polarised state. Besides this generic scheme, very close to T_C additional features appear both in χ' and χ'' in relation with the boundaries of the A-phase.

The extraction of an exact phase diagram however, with precise values for the critical fields is not an easy task as the result very much depends on the specific criteria used. This is illustrated by Fig. 3.6, that displays the magnetic field dependence of the ZFC χ', its first derivative $d\chi'/dB$ and the corresponding χ'' at $T = 57.3$ K, a characteristic temperature where all features are present. One may indeed choose either the inflection points of χ' or the maxima of χ'' to define the phase boundaries. Both choices are valid and would lead to magnetic fields with similar temperature dependence. We chose the peaks of χ'' at $f = 0.8$ Hz to define B_{C1} and the boundaries of the A-Phase, B_{A1} and B_{A2} respectively. On the other hand χ'' is zero at high fields and for this reason B_{C2} was defined from the inflection point of χ'. The lower and upper boundaries of this transition can be estimated from the extrema of the second derivative $d^2\chi'/dB^2$ (thus the inflection points of the first derivative $d\chi'/dB$), which are given by the red dotted lines in Fig. 3.6(b) and will discussed at the phase diagram section below.

A clear overview of the phase diagram and the transitions between the helical, conical, A- and field polarized phases respectively is only provided by the analysis as a function of the magnetic field presented above. If only the temperature dependence of the susceptibility is considered, as it was the case in the previous study [23], the different contributions merge into broad features as illustrated by Fig. 3.4(c), in particular between 9 and 12 mT, and thus no clear indications for the phase boundaries can be obtained.

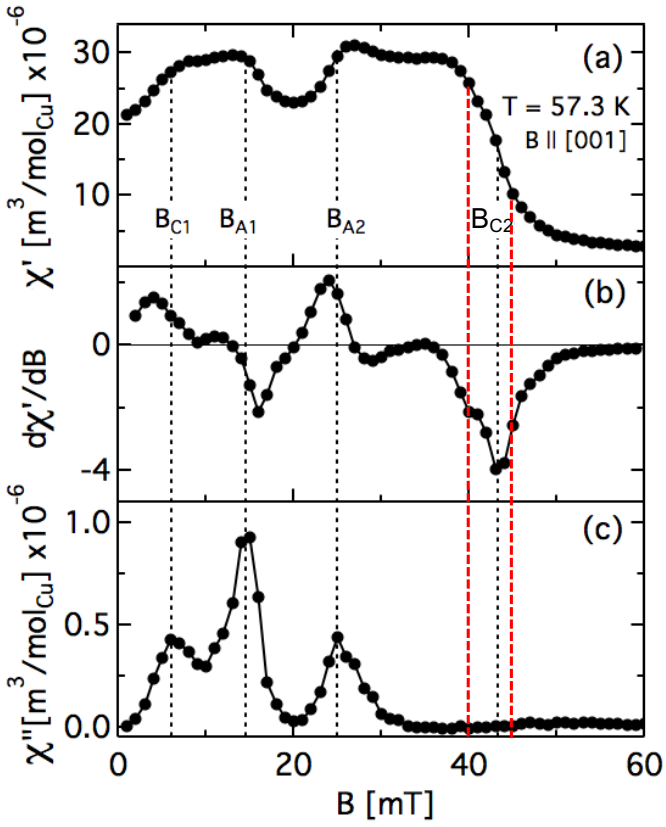

Figure 3.6: Magnetic field dependence of ZFC χ', its derivative $d\chi'/dB$ and the corresponding χ'' of Cu_2OSeO_3 at $T = 57.3$ K for $B \parallel [001]$ and $f = 0.8$ Hz. The maxima of χ'' define the lower critical field $B_{C1} = 6$ mT as well as the lower and upper boundaries of the A-phase, $B_{A1} = 14.5$ mT and $B_{A2} = 25$ mT, respectively. The upper critical field ($B_{C2} = 43$ mT) was determined from the inflection points of χ' and the extrema of $d\chi'/dB$. The red dotted lines correspond to the inflection points of $d\chi'/dB$ at the two sides of B_{C2} and thus to the lower and upper boundaries of this transition. The unit of $d\chi'/dB$ is $m^3/(mol_{Cu} \cdot mT) \times 10^{-6}$.

3.5. FREQUENCY DEPENDENCE OF THE SUSCEPTIBILITY

The previous section discussed results at $f = 0.8$ Hz. However, the susceptibility depends on the frequency of the AC drive field as highlighted by Fig. 3.7, where ZFC χ' and χ'' are displayed versus the magnetic field for some selected frequencies and $T = 57.3$ K. The minimum in χ', which is characteristic for the A-phase is best defined at low frequencies. With increasing frequency, the minimum broadens, accompanied by a decreasing amplitude of the hump-like edges

at both sides.

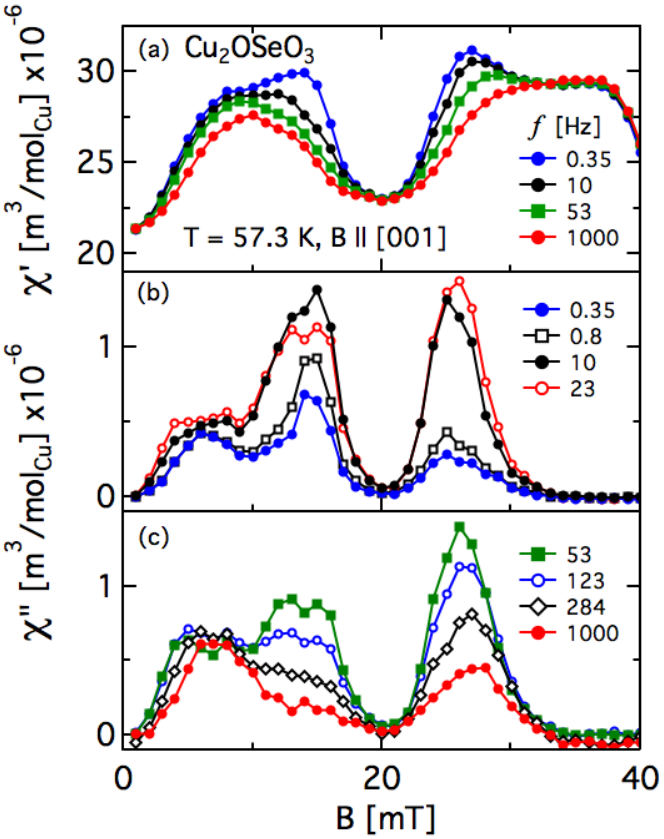

Figure 3.7: Magnetic field dependence of ZFC χ' (a) and χ'' (b and c) of Cu_2OSeO_3 at $T = 57.3$ K and for the frequencies indicated.

The most dramatic changes are found for χ'', which at 0.35 Hz displays the three well-defined maxima related to the phase boundaries B_{C1}, B_{A1} and B_{A2}. The amplitude of these maxima changes with frequency but their position remains roughly the same.

A more detailed overview of the effect of frequency is given in Fig. 3.8, where χ' and χ'' are displayed as a function of frequency for selected magnetic fields around $B_{C1} = 6$ mT (a and d), $B_{A1} = 14.5$ mT (b and e) and $B_{A2} = 25$ mT (c and f) at $T = 57.3$ K. As already mentioned and illustrated by Fig. 3.7, χ' does not depend on the frequency for $B = 0$ and $\chi'' = 0$. However, even weak magnetic fields induce noticeable effects shown in both Fig. 3.7 and 3.8. The broad bell-shaped frequency dependence of χ'' seen in Fig. 3.8 (d-f) reflects a distribution of relax-

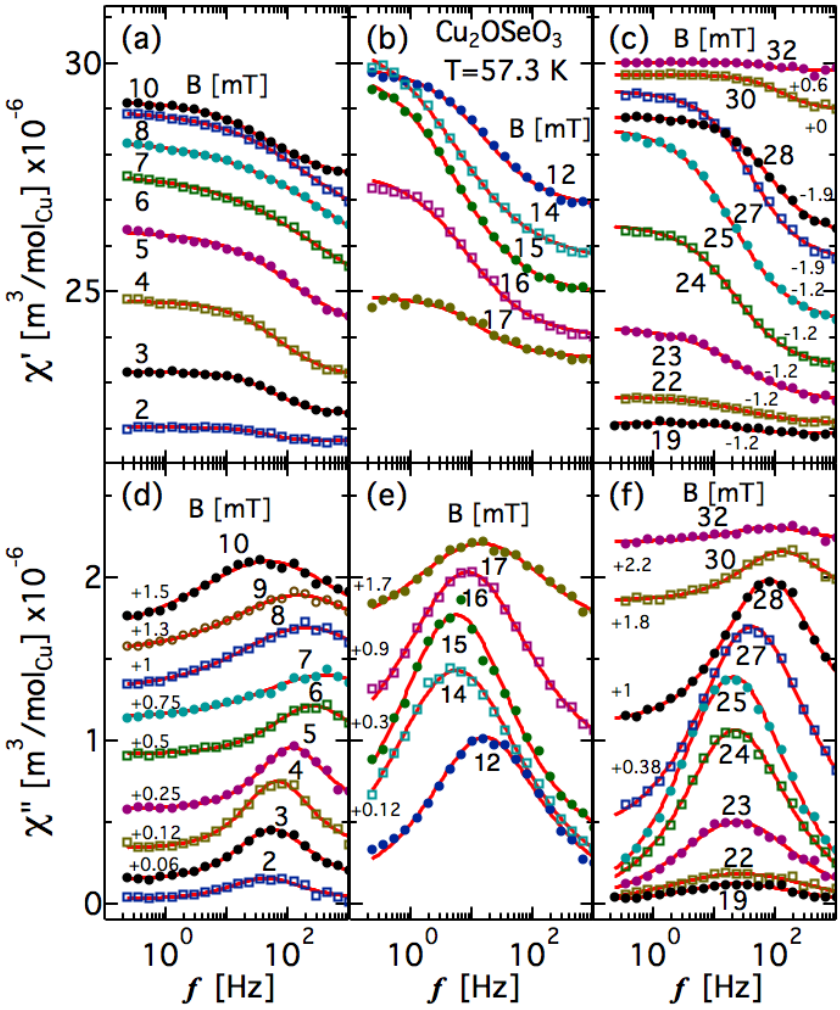

Figure 3.8: Frequency dependence of ZFC χ' and χ'' of Cu_2OSeO_3 at $T = 57.3$ K for magnetic fields around B_{C1} (a and d), B_{A1} (b and e) and B_{A2} (c and f) respectively. The lines represent fits of eqs. (3.2) and (3.3). For the sake of clarity some data sets in panel (c-f) have been vertically shifted with respect to the baseline as indicated.

ation frequencies centred at the characteristic frequency f_0, which varies non-monotonically around B_{C1}, B_{A1} and B_{A2}. Similar behaviour has already been reported for Cu_2OSeO_3 [23] and the quantitative analysis is based on the modified Cole-Cole formalism [31, 32]:

$$\chi(\omega) = \chi(\infty) + \frac{\chi(0) - \chi(\infty)}{1 + (i\omega\tau_0)^{1-\alpha}} \tag{3.1}$$

with $\chi(0)$ and $\chi(\infty)$ the isothermal and adiabatic susceptibilities, $\omega = 2\pi f$ the angular frequency, $\tau_0 = 1/(2\pi f_0)$ the characteristic relaxation time and α a parameter that accounts for the width of the relaxation frequencies distribution, $\alpha = 1$ for an infinitely broad distribution and $\alpha = 0$ for a single relaxation process. Thus $\alpha = 0$ corresponds to a simple exponential and $\alpha > 0$ to a stretched exponential relaxation, which can be attributed to a distribution of energy barriers in a phase-space landscape [33]. Eq. 3.1 can be decomposed in the in- and out-of-phase components [32, 34] :

$$\chi'(\omega) = \chi(\infty) + \frac{A_0[1 + (\omega\tau_0)^{1-\alpha}\sin(\pi\alpha/2)]}{1 + 2(\omega\tau_0)^{1-\alpha}\sin(\pi\alpha/2) + (\omega\tau_0)^{2(1-\alpha)}} \tag{3.2}$$

$$\chi''(\omega) = \frac{A_0\cos(\pi\alpha/2)(\omega\tau_0)^{1-\alpha}}{1 + 2(\omega\tau_0)^{1-\alpha}\sin(\pi\alpha/2) + (\omega\tau_0)^{2(1-\alpha)}} \tag{3.3}$$

with $A_0 = \chi(0) - \chi(\infty)$. The fit of these equations to the data, leads to the solid lines in Fig. 3.8 and the parameters, $f_0 = 1/(2\pi\tau_0)$, α and A_0 are plotted as a function of the magnetic field in Fig. 3.9.

The characteristic frequency f_0 shown in Fig. 3.9(a) is derived from the maxima of χ'' varies non-monotonically with B. First a maximum develops slightly above B_{C1}, indicating the acceleration of the dynamics at the border between the helical and conical phases. Then clear minima, reflecting a slowing down of the relaxation, mark the limits of the A-phase B_{A1} and B_{A2} respectively.

The parameter α given in Fig. 3.9(b) shows no clear trends, but remains non-zero over the whole magnetic field range, as previously found [23]. This implies a stretched exponential relaxation similar to spin glasses [32, 34] and is in agreement with the glassiness found by electron microscopy for Cu_2OSeO_3 [35] and other systems with similarly long helices [36].

The pre-factor $A_0 = \chi(0) - \chi(\infty)$ given in Fig. 3.9(c) shows clear maxima at B_{C1}, B_{A1} and B_{A2}. Consequently at these characteristic fields the difference between $\chi(0)$ and $\chi(\infty)$ is the strongest and the magnetic relaxation phenomena are most prominent.

For $B < 10$ mT, which includes B_{C1}, the fit of χ' and χ'' does not lead to the same values for α and A_0, indicating the existence of an additional process. Indeed in this magnetic field range an almost frequency independent component,

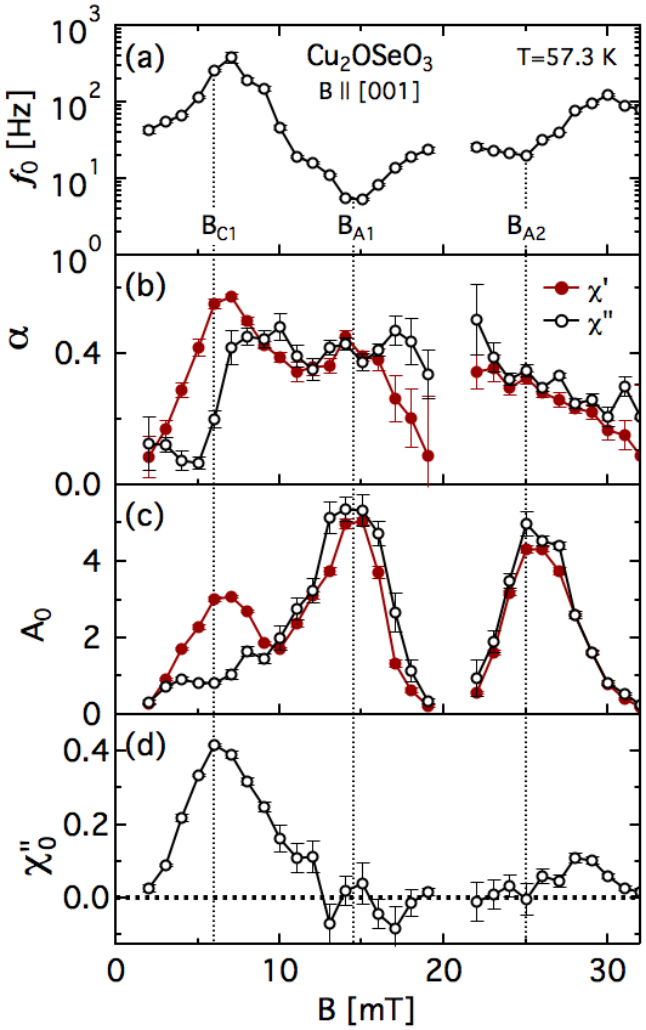

Figure 3.9: Magnetic field dependence of (a) the characteristic frequency f_0, (b) the relaxation times distribution parameter α, and (c) $A_0 = \chi(0) - \chi(\infty)$ as defined by eq. 3.2. The open and closed symbols correspond to the parameters extracted from χ'' and χ' respectively. The phase boundaries B_{C1}, B_{A1}, and B_{A2} are indicated by the vertical dashed lines. No fits are possible in the centre of the A-phase, which explains the absence of points. Panel (d) displays a frequency independent component χ_0'', which is required to fit χ'' around B_{C1} and accounts for the different A_0 derived from χ' and χ'' respectively. The units of A_0 and χ_0'' are $\mathrm{m}^3/\mathrm{mol}_{\mathrm{Cu}} \times 10^{-6}$.

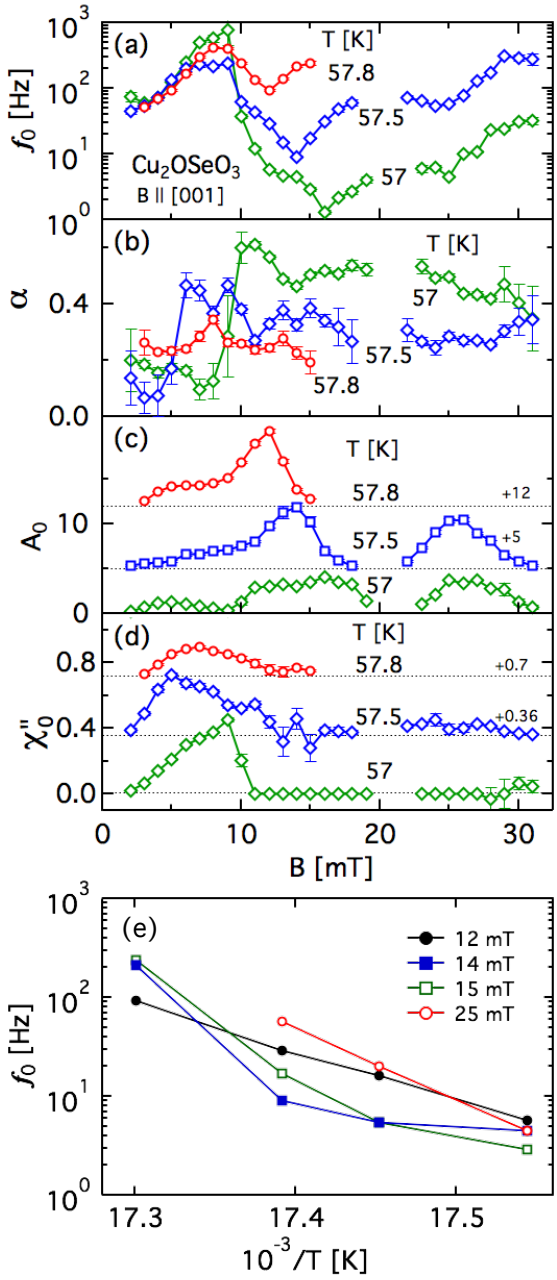

Figure 3.10: Magnetic field dependence of (a) the characteristic frequency f_0, (b) the relaxation times distribution parameter α, (c) the amplitude $A_0 = \chi(0) - \chi(\infty)$ and (d) the constant term χ''_0 for the temperatures indicated, obtained from the fits of eq. 3.3 to χ'' of Cu_2OSeO_3. For the sake of clarity some A_0 and χ''_0 curves have been shifted with respect to the baseline as indicated. No fits are possible in the centre of the A-phase and above 15 mT for 57.8 K, which explains the absence of points. The units of A_0 and χ''_0 are $m^3/mol_{Cu} \times 10^{-6}$. Panel (e) shows the temperature dependence of f_0 from panel (a) for various magnetic fields.

designated by χ_0'' and shown in Fig. 3.9(d) exists that is most visible on χ'' and is at the origin of the different A_0 values derived from χ' and χ''. As it will be discussed below it is also seen on the Cole-Cole plots.

The magnetic field dependence of f_0, α, A_0 and χ_0'' derived from χ'' is given in Fig. 3.10 for some selected temperatures. The figure shows the same trends as Fig. 3.9. The relaxation involves indeed macroscopic characteristic times, which reflect rearrangements over large magnetic volumes. We note that all maxima and minima of f_0 and A_0 are correlated with the phase boundaries B_{C1}, B_{A1} and B_{A2}.

Figure 3.10(a) shows that f_0 is almost temperature independent at B_{C1} but varies strongly with temperature at B_{A1} and B_{A2}. At these magnetic fields a simple Arrhenius law $f_0 = A\,exp(-E/k_BT)$ implies a linear dependence of $\log(f_0)$ on $1/T$. As seen in Fig. 3.10 (e) this is in general not the case. Furthermore, an Arrhenius fit to the data leads to un-physically large energy barriers of the order of 10^4 K. Thus the temperature dependence of the relaxation cannot be accounted for by a simple thermal activation picture.

3.6. COLE-COLE ANALYSIS

The Cole-Cole formalism interrelates χ' and χ'' and from eq. 3.2 and 3.3 one deduces:

$$\chi''(\omega) = -B_0 + \Big[B_0^2 + A_0\left(\chi'(\omega) - \chi(\infty)\right) - \left(\chi'(\omega) - \chi(\infty)\right)^2\Big]^{1/2} \tag{3.4}$$

with $B_0 = A_0 \tan(\pi\alpha/2)/2$. This relation has three free parameters, $\chi(\infty)$, A_0 and α, and corresponds to the equation of a circular arc centred at the maximum of χ'', where $\omega\tau_0 = 1$. Resulting Cole-Cole plots are shown in Fig. 3.11, where the ZFC data of Fig. 3.8 have been replotted for selected magnetic fields. The Cole-Cole plots for one relaxation process are symmetric and centred at $\chi' = [\chi(0) + \chi(\infty)]/2$, where χ'' is maximum. As the parameter α is proportional to the ratio of the bottom width to the height of the curves, the plots directly evidence the existence of a distribution of relaxation times.

The data fall on a circular arc as expected by eq. 3.4 and are well described for all magnetic fields expect for $4 \lesssim B \lesssim 8$ mT, where significant deviations at the highest values of χ', which correspond to the lowest frequencies, are observed. This is indeed the magnetic field range, where eq. 3.2 and 3.3 do not give consistent results for both χ' and χ'' as witnessed by the different values of A_0 and α shown in Fig. 3.9 and the frequency independent term χ_0'' that must be con-

sidered to properly account for χ''. These deviations reveal the existence of additional relaxation mechanisms, the origin of which is unknown. In analogy to ferromagnets we speculate that they may be due to domain wall motion and coexist with the main dynamic process associated with the helical to conical phase transition. Indeed these deviations disappear above B_{C1} where the system becomes mono-domain under the influence of the strong external magnetic field.

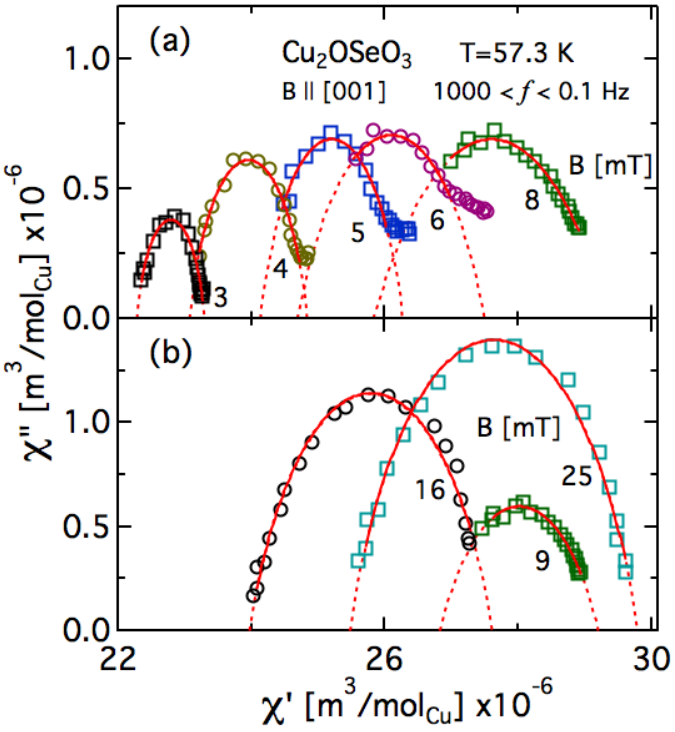

Figure 3.11: Cole-Cole plots of Cu_2OSeO_3 for various magnetic fields at $T = 57.3$ K. The dashed lines represent the fits of eq. 3.4 to the data.

3.7. PHASE DIAGRAM CLOSE TO T_C

The magnetic field, temperature and frequency dependence of χ' and χ'' are summarised by the contour plots of Fig. 3.12 for $f = 0.8$ Hz, 23 Hz and 1 kHz. The frequency has a weak effect on χ' in contrast to χ''. The contour plots also illustrate the differences in the frequency dependence around B_{C1} on one side and around B_{A1} or B_{A2} on the other side, addressed at the previous sections, e.g. see Fig. 3.7. Consequently, the strongest χ'' in Fig. 3.12 is for $f = 23$ Hz at B_{A1} or

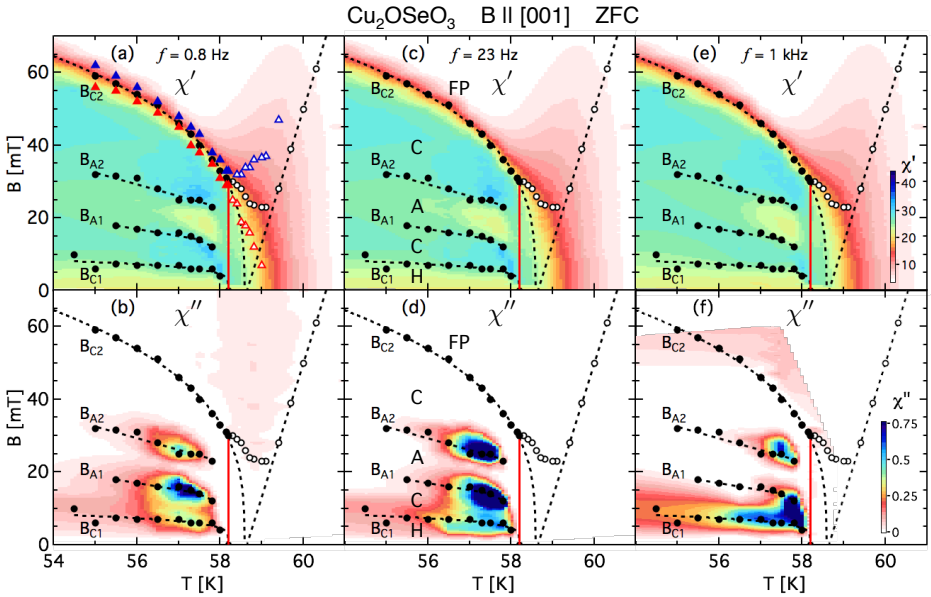

Figure 3.12: Contour plots of ZFC χ' and χ'' of Cu_2OSeO_3 measured at the frequencies $f = 0.8$ Hz (a and b) , 23 Hz (c and d) and 1 kHz (e and f) displayed versus temperature and magnetic field. The values given at the colour codes correspond to $m^3/mol_{Cu} \times 10^{-6}$. The vertical red lines indicate T_C at $B = 0$. The characteristic magnetic fields B_{C1}, B_{A1}, B_{A2} and B_{C2} determined at 0.8 Hz are also indicated. The lower and upper boundaries of the transition at B_{C2} are illustrated in panel (a) by the blue and red triangles determined from the inflection points of $d\chi'/dB$. Above T_C the extrema of the first and second derivatives of χ' are illustrated with open symbols to distinguish from B_{C2} below T_C. In the panels (c) and (d) we identify the following phases: H for helical, C for conical, A for the A-phase and FP for the field polarised one.

B_{A2}, and for $f = 1$ kHz at B_{C1}. At this highest frequency the phase boundaries seen in χ'' almost obliterate.

Very weak signals in χ'' appear for $B > B_{C2}$ in the panels (b) and (f). The origin of the χ'' at $f = 0.8$ Hz is unclear and we plan to investigate this feature more in detail in the future. We note that similar features have been found also at very low frequencies in MnSi and the soliton lattice system $Cr_{1/3}NbS_2$ [37, 38]. On the other hand, the signal at 1 kHz may be associated with the spin dynamics in the field-polarised phase. In this phase the magnetic field is strong enough to overcome the DM interaction and the behaviour crosses-over to ferromagnetism with clear susceptibility maxima developing above T_C. These shift to higher temperatures with increasing magnetic field, as shown in Fig. 3.2(d) and in the χ' contour plots of Fig. 3.12(a), (c) and (e).

Below T_C the temperature dependence of B_{C2} is described by the power law

$B_{C2} \propto (T - T_0)^{0.318 \pm 0.03}$ with $T_0 = 58.6 \pm 0.15$ K, i.e. $\sim T_C + 0.4$ K. The extrapolation of this power law to low fields is given by the black dashed lines in Fig. 3.12 and is in good agreement with the contour plots of χ'. The lower and upper magnetic field limits deduced from the inflection points of $d\chi'/dB$, as illustrated by the red dotted lines in Fig.3.6, are also given by the blue and red triangles in Fig. 3.12(a). These are very close to B_{C2} deduced from the first derivative of χ' (black dots in Fig. 3.12(a)) and follow the same power law. Thus the result is not affected by the specific criterion used and the sharpness of the transition.

Above T_C, the steep change of χ' at B_{C2}, reflected by the sharp minimum of the first derivative $d\chi'/dB$ in Fig. 3.6 broadens with increasing temperature. To distinguish from B_{C2} below T_C, the inflection point of χ' above T_C is illustrated with open circles. It goes through a minimum at $\sim$ 59 K and for higher temperatures increases linearly with temperature, extrapolating to $T_0 = 58.6$ K at zero field. This linear temperature dependence of the inflection points of χ' at high fields can also be derived from a magnetisation Brillouin function. In this case, similarly to the Curie-Weiss law for the susceptibility, T_0 corresponds to the mean-field average of the interactions and is equivalent to a Curie-Weiss temperature.

For $B < B_{C2}$ the plots of Fig. 3.12 reveal the areas associated with the helical, conical and A-phases respectively. On the χ' plots, Fig. 3.12(a),(c) and (e), the yellowish area below the B_{C1} line corresponds to the helical phase, whereas the light blue areas between B_{C1} and B_{A1} and between B_{A2} and B_{C2} to the conical phase. Between B_{A1} and B_{A2}, a yellowish area with almost a triangular shape at low frequencies stands for the centre of the A-phase. The high temperature limits of the A-phase are better defined than the low temperature ones, where below $\sim$ 57 K a rather gradual crossover from the A-phase to the conical is observed.

Remarkably neither the high temperature nor the low temperature limits of the A-phase are seen on χ'', panels (b), (d) and (f) of Fig. 3.12, in contrast to the clear delimitation of the low and upper magnetic field limits B_{A1} and B_{A2} respectively. We note that this result does not depend on the way the measurements were performed: temperature scans at constant magnetic fields (FC) and magnetic field scans at constant temperatures (ZFC) give exactly the same results within the experimental accuracy. Thus the temperature induced transitions into and out of the A-phase are not equivalent to the magnetic field induced ones. In MnSi the (1st order phase transition) upper temperature limits of the A-phase are clearly seen by specific heat but not in χ'' for $f = 1$ kHz [39]. This might also explain the absence of χ'' for the temperature limit of the A-phase in Cu_2OSeO_3 as well.

The absence of a clear low temperature boundary of the A-phase on χ'' may be another indication for a gradual crossover to the conical phase seen by χ'. In

such a case the magnetic relaxation phenomena might be spread over a broad temperature range and the resulting χ'' signal might become too weak to be detected.

3.8. CONCLUSION

The analysis of the DC magnetization and AC suceptibility of Cu_2OSeO_3 as a function of the magnetic field, instead of the temperature as in previous studies provides a quantitative approach to the phase diagram. The investigation of the $B-T$ phase diagram of Cu_2OSeO_3 by DC magnetisation and AC susceptibility shows that the borders between the different phases (helical, conical and A-phase) are not sharp but their exact position depends on the specific technique and criteria used. The frequency dependence of χ'', between the helical and conical phases at B_{C1} and between the conical and A-phases at B_{A1} and B_{A2}, is governed by almost macroscopic relaxation times, which reach some milliseconds and may be attributed to rearrangements over large magnetic volumes. An additional relaxation process has also been found, which appears only at very low frequencies and around B_{C1}. The strongly non-exponential relaxation bears similarities with spin glasses and is in-line with the glassy behaviour reported by electron microscopy in Cu_2OSeO_3 and other systems with similarly long helices. The dynamical phenomena discussed at the previous sections could be at the origin of the different phase boundaries reported in the literature not only for Cu_2OSeO_3 but also for other systems of the same family including the reference chiral magnet MnSi.

REFERENCES

[1] F. Qian, H. Wilhelm, A. Aqeel, T. Palstra, A. Lefering, E. Brück, and C. Pappas, *Phase diagram and magnetic relaxation phenomena in Cu_2OSeO_3,* Phys. Rev. B **94**, 064418 (2016).

[2] I. Dzyaloshinsky, *A thermodynamic theory of "weak" ferromagnetism of antiferromagnetics,* J. Phys. Chem. Solids **4**, 241 (1958).

[3] T. Moriya, *Anisotropic superexchange interaction and weak ferromagnetism,* Physical review **120**, 91 (1960).

[4] A. N. Bogdanov and D. A. Yablonskii, *Thermodynamically stable "vortices" in magnetically ordered crystals. The mixed state of magnets,* Sov. Phys. JETP **68**, 101 (1989).

[5] A. Bogdanov and A. Hubert, *Thermodynamically stable magnetic vortex states in magnetic crystals,* J. Magn. Magn. Mater. **138**, 255 (1994).

[6] U. K. Rößler, A. Leonov, and A. N. Bogdanov, *Chiral Skyrmionic matter in non-centrosymmetric magnets,* J. Phys.: Conf. Ser. **303**, 012105 (2011).

[7] N. Nagaosa and Y. Tokura, *Topological properties and dynamics of magnetic skyrmions,* Nat. Nanotechnol. **8**, 899 (2013).

[8] S. Mühlbauer, B. Binz, F. Jonietz, C. Pfleiderer, A. Rosch, A. Neubauer, R. Georgii, and P. Böni, *Skyrmion lattice in a chiral magnet,* Science **323**, 915 (2009).

[9] A. Tonomura, X. Yu, K. Yanagisawa, T. Matsuda, Y. Onose, N. Kanazawa, H. S. Park, and Y. Tokura, *Real-Space Observation of Skyrmion Lattice in Helimagnet MnSi Thin Samples,* Nano Lett. **12**, 1673 (2012).

[10] X. Z. Yu, N. Kanazawa, Y. Onose, K. Kimoto, W. Z. Zhang, S. Ishiwata, Y. Matsui, and Y. Tokura, *Near room-temperature formation of a skyrmion crystal in thin-films of the helimagnet FeGe,* Nat Mater **10**, 106 (2010).

[11] H. Wilhelm, M. Baenitz, M. Schmidt, U. K. Rößler, A. A. Leonov, and A. N. Bogdanov, *Precursor Phenomena at the Magnetic Ordering of the Cubic Helimagnet FeGe,* Phys. Rev. Lett. **107**, 127203 (2011).

[12] E. Moskvin, S. Grigoriev, V. Dyadkin, H. Eckerlebe, M. Baenitz, M. Schmidt, and H. Wilhelm, *Complex Chiral Modulations in FeGe Close to Magnetic Ordering,* Phys. Rev. Lett. **110**, 077207 (2013).

[13] X. Z. Yu, Y. Onose, N. Kanazawa, J. H. Park, J. H. Han, Y. Matsui, N. Nagaosa, and Y. Tokura, *Real-space observation of a two-dimensional skyrmion crystal,* Nature **465**, 901 (2010).

[14] W. Münzer, A. Neubauer, T. Adams, S. Mühlbauer, C. Franz, F. Jonietz, R. Georgii, P. Böni, B. Pedersen, M. Schmidt, A. Rosch, and C. Pfleiderer, *Skyrmion lattice in the doped semiconductor $Fe_{1-x}Co_xSi$,* Phys. Rev. B **81**, 041203(R) (2010).

[15] H. S. Park, X. Yu, S. Aizawa, T. Tanigaki, T. Akashi, Y. Takahashi, T. Matsuda, N. Kanazawa, Y. Onose, D. Shindo, A. Tonomura, and Y. Tokura, *Observation of the magnetic flux and three-dimensional structure of skyrmion lattices by electron holography,* Nat. Mater. **9**, 337 (2014).

[16] S. Seki, X. Z. Yu, S. Ishiwata, and Y. Tokura, *Observation of Skyrmions in a Multiferroic Material,* Science **336**, 198 (2012).

[17] S. Seki, J. H. Kim, D. S. Inosov, R. Georgii, B. Keimer, S. Ishiwata, and Y. Tokura, *Formation and rotation of skyrmion crystal in the chiral-lattice insulator Cu_2OSeO_3*, Phys. Rev. B **85**, 220406(R) (2012).

[18] T. Adams, A. Chacon, M. Wagner, A. Bauer, G. Brandl, B. Pedersen, H. Berger, P. Lemmens, and C. Pfleiderer, *Long-Wavelength Helimagnetic Order and Skyrmion Lattice Phase in Cu_2OSeO_3*, Phys. Rev. Lett. **108**, 237204 (2012).

[19] J. S. White, I. Levatić, A. A. Omrani, N. Egetenmeyer, K. Prša, I. Živković, J. L. Gavilano, J. Kohlbrecher, M. Bartkowiak, H. Berger, and H. M. Rønnow, *Electric field control of the skyrmion lattice in Cu_2OSeO_3*, J. Phys.: Condens. Matter **24**, 432201 (2012).

[20] J. S. White, K. Prša, P. Huang, A. A. Omrani, I. Živković, M. Bartkowiak, H. Berger, A. Magrez, J. L. Gavilano, G. Nagy, J. Zang, and H. M. Rønnow, *Electric-Field-Induced Skyrmion Distortion and Giant Lattice Rotation in the Magnetoelectric Insulator Cu_2OSeO_3*, Phys. Rev. Lett. **113**, 107203 (2014).

[21] J.-W. G. Bos, C. V. Colin, and T. T. M. Palstra, *Magnetoelectric coupling in the cubic ferrimagnet Cu_2OSeO_3*, Phys. Rev. B **78**, 094416 (2008).

[22] M. Belesi, I. Rousochatzakis, H. C. Wu, and H. Berger, *Ferrimagnetism of the magnetoelectric compound Cu_2OSeO_3 probed by ^{77}Se NMR*, Phys. Rev. B (2010).

[23] I. Levatić, V. Šurija, H. Berger, and I. Živković, *Dissipation processes in the insulating skyrmion compound Cu_2OSeO_3*, Phys. Rev. B **90**, 224412 (2014).

[24] K. H. Miller, X. S. Xu, H. Berger, E. S. Knowles, D. J. Arenas, M. W. Meisel, and D. B. Tanner, *Magnetodielectric coupling of infrared phonons in single-crystal Cu_2OSeO_3*, Phys. Rev. B **82**, 144107 (2010).

[25] I. Živković, D. Pajić, T. Ivek, and H. Berger, *Two-step transition in a magnetoelectric ferrimagnet Cu_2OSeO_3*, Phys. Rev. B **85**, 224402 (2012).

[26] S. M. Stishov, A. E. Petrova, S. Khasanov, G. K. Panova, A. A. Shikov, J. C. Lashley, D. Wu, and T. A. Lograsso, *Magnetic phase transition in the itinerant helimagnet MnSi: Thermodynamic and transport properties*, Phys. Rev. B **76** (2007).

[27] S. M. Stishov and A. E. Petrova, *Vollhardt invariant and phase transition in the helical itinerant magnet MnSi*, Phys. Rev. B **94**, 140406(R) (2016).

[28] I. Živković, J. S. White, H. M. Rønnow, K. Prša, and H. Berger, *Critical scaling in the cubic helimagnet Cu_2OSeO_3*, Phys. Rev. B **89**, 060401(R) (2014).

[29] S. Seki, S. Ishiwata, and Y. Tokura, *Magnetoelectric nature of skyrmions in a chiral magnetic insulator Cu_2OSeO_3,* Phys. Rev. B **86**, 060403(R) (2012).

[30] A. Bauer and C. Pfleiderer, *Magnetic phase diagram of MnSi inferred from magnetization and ac susceptibility,* Phys. Rev. B **85**, 214418 (2012).

[31] K. S. Cole and R. H. Cole, *Dispersion and Absorption in Dielectrics I. Alternating Current Characteristics,* J. Chem. Phys. **9**, 341 (1941).

[32] D. Huser, A. J. van Duyneveldt, G. J. Nieuwenhuys, and J. A. Mydosh, *Phenomenological model for the frequency dependence of the susceptibility of spin glasses and related compounds,* J. Phys. C: Solid State Phys. **19**, 3697 (1986).

[33] I. A. Campbell, *Ordering and relaxation in spin glasses,* Phys. Rev. B **33**, 3587 (1986).

[34] C. Dekker, A. Arts, H. W. Dewijn, A. J. Vanduyneveldt, and J. A. Mydosh, *Activated dynamics in a two-timensional Ising spin glass: $Rb_2Cu_{1-x}Co_xF_4$,* Phys. Rev. B **40**, 11243 (1989).

[35] J. Rajeswari, P. Huang, G. F. Mancini, Y. Murooka, T. Latychevskaia, D. McGrouther, M. Cantoni, E. Baldini, J. S. White, A. Magrez, T. Giamarchi, H. M. Rønnow, and F. Carbone, *Filming the formation and fluctuation of skyrmion domains by cryo-Lorentz transmission electron microscopy,* P Natl Acad Sci USA **112**, 14212 (2015).

[36] P. Milde, D. Kohler, J. Seidel, L. M. Eng, A. Bauer, A. Chacon, J. Kindervater, S. Mühlbauer, C. Pfleiderer, S. Buhrandt, C. Schutte, and A. Rosch, *Unwinding of a Skyrmion Lattice by Magnetic Monopoles,* Science **340**, 1076 (2013).

[37] K. Tsuruta, M. Mito, Y. Kousaka, J. Akimitsu, J. Kishine, and K. Inoue, *Nonlinear magnetic responses in skyrmion phase of MnSi and chiral-soliton-lattice phase of $Cr_{1/3}NbS_2$,* poster presentation at χ-Mag2016, Hiroshima, Japan (2016).

[38] K. Tsuruta, M. Mito, H. Deguchi, J. Kishine, Y. Kousaka, J. Akimitsu, and K. Inoue, *Phase diagram of the chiral magnet $Cr_{1/3}NbS_2$ in a magnetic field,* Phys. Rev. B **93**, 104402 (2016).

[39] A. Bauer, M. Garst, and C. Pfleiderer, *Specific heat of the skyrmion lattice phase and field-induced tricritical point in MnSi,* Phys. Rev. Lett. **110**, 177207 (2013).

4

NEUTRON SCATTERING INVESTIGATIONS OF MAGNETIC CORRELATIONS AND DYNAMICS CLOSE TO T_C FOR Cu_2OSeO_3

The magnetic correlations and dynamics of Cu_2OSeO_3 have been investigated by small angle neutron scattering, polarisation analysis and high resolution neutron spin echo spectroscopy close to T_C. At zero field, the helimagnetic transition at T_C is of first order. Above T_C, short range chiral magnetic correlations persist, as in the archetype MnSi. Under magnetic fields in the skyrmion lattice phase, the scattering patterns depend on the crystal lattice orientation and the magnetic history, which indicates coupling between the skyrmion and the crystal lattices. In addition, relaxation processes are seen by rapidly changing the magnetic field, with the neutron scattering pattern being the signature of the different phases of the phase diagram: helical, conical and skyrmion lattice phases.

4.1. INTRODUCTION

Cu_2OSeO_3 is currently the only known insulating chiral helimagnet and is characterised by a more complex crystal structure than the metallic B20 compounds [1–3], although with the same $P2_13$ space group. The unit cell contains 16 Cu^{2+} ions on two different sites, Cu(1) and Cu(2) [4, 5], which form tetrahedra composed of three Cu(1) and one Cu(2). In contrast to the B20 metallic chiral magnets, in Cu_2OSeO_3 the superexchange magnetic interactions between the Cu^{2+} spins and the DM interactions can be calculated ab-initio at the atomic level [6–8] providing a direct link between theory and experiment. This approach reveals the existence of weak and strong magnetic bonds and a separation of exchange energy scales beyond the one encountered in the B20 metallic counterparts [9].

At zero field the helimagnetic transition is of weakly first order, as evidenced by a sharp peak at T_C in the specific heat [10, 11]. On the other hand, a broad maximum of the specific heat and the susceptibility [12, 13] can be associated with precursor phenomena, similarly to MnSi [14–16]. On the application of magnetic fields and in the A-phase region, the skyrmion lattice is stablised, but the neutron scattering pattern is more complex than in MnSi, showing either six or twelve Bragg peaks [10, 17, 18] depending on the orientation of the crystal as well as the magnetic and thermal history [18].

In the following, the precursor phenomena and the phase transition of Cu_2OSeO_3 at zero field will be discussed based on small angle neutron scattering (SANS) in combination with polarisation analysis and high resolution neutron spin echo spectroscopy measurements. These indicate a first order phase transition at T_C and chiral short range order above T_C, as in the archetype helimagnet MnSi.

The scattering of the skyrmion lattice phase under magnetic fields shows a dependence on the crystal lattice orientation and the magnetic history. In addition, by rapidly changing the magnetic field, the scattering patterns change with time as if the sample relaxes through the different phases of the magnetic phase diagram.

4.2. EXPERIMENT DETAILS

The sample was a single crystal grown by chemical vapour transport method with dimensions of $\sim 3\times3\times5$ mm^3. It was aligned with the $\langle 110\rangle$ crystallographic axis vertical within an accuracy of $\pm5^\circ$. By rotating the sample around the vertical axis, it was possible to bring different crystallographic orientations into the Bragg condition.

Neutron scattering measurements were performed at the small angle neutron scattering (SANS) instruments PAXY and PA20 of the Laboratoire Léon Brillouin and the neutron spin echo (NSE) spectrometer IN15 of the Institut Laue Langevin. At PAXY, the measurements were performed at a wavelength of λ = 9.5 Å with $\Delta\lambda/\lambda$ = 10%. The position sensitive detector of 64×64 cm^2 with 0.5×0.5 cm^2 pixel resolution was placed at 6.7 m from the sample. At PA20, the neutron beam wavelength was λ = 6 Å with $\Delta\lambda/\lambda$ = 10%, and the detector was put at 12.7 m away from the sample. A magnetic field B parallel to the incoming neutron beam was created by a 10 T horizontal cryomagnet.

At IN15, the measurements were performed using polarised neutron beams with a polarisation of 95% and $\Delta\lambda/\lambda$ = 15%. The wavelength was λ = 8 Å for the NSE and polarisation analysis measurements, and λ = 12.5 Å for the measurements under magnetic fields. The position sensitive detector had the dimensions of 32×32 cm^2 with a pixel resolution of 1×1 cm^2 and was placed at 4.6 m from the sample. A 7 T horizontal Cryomagnet was used to produce magnetic fields along the incoming neutron beam.

Background corrections were performed using measurements at 70 K where the magnetic scattering is negligible. Due to different thermometers used in those set-ups, most of the results in the following are plotted against $(T-T_C)$.

4.3. MAGNETIC CORRELATIONS AT ZERO FIELD

Figure 4.1(a) depicts SANS scattering patterns at zero field and close to T_C measured at PAXY. With decreasing temperature a weak diffuse pattern above T_C develops to a ring-shaped diffuse scattering at $\sim T_C+0.1$ K with a radius corresponding to the helix wave vector modulation $\tau=2\pi/\ell=0.105\pm0.001$ nm^{-1} and $\ell\sim60\pm1$ nm. This radius shows weak temperature dependence, which will be addressed below.

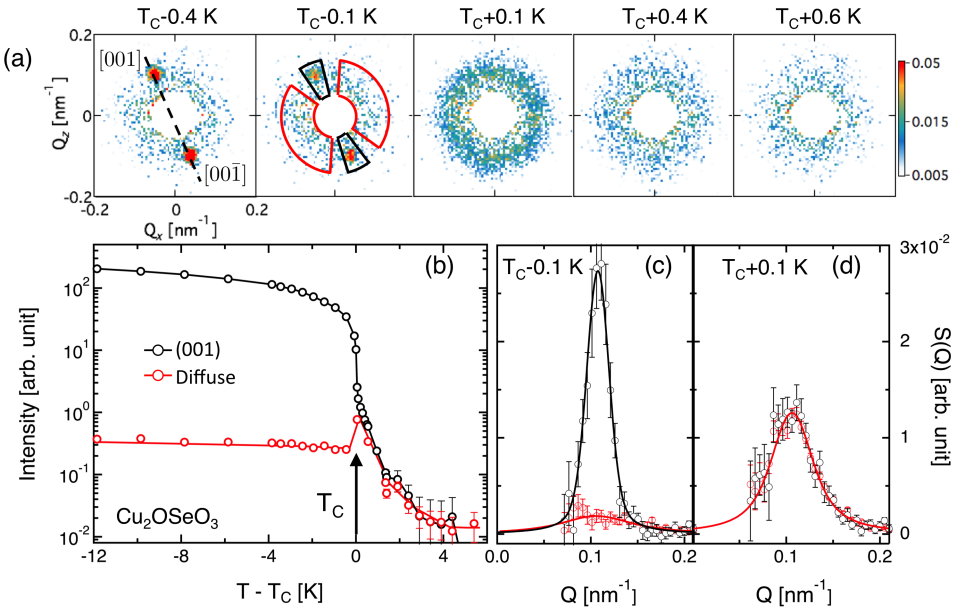

Figure 4.1: (a) Neutron scattering patterns at zero field and in the vicinity of T_C collected at PAXY for Cu_2OSeO_3. The fan-shaped frames represent the areas over which the intensity has been averaged. The black frames correspond to the ⟨001⟩ crystallographic directions and the red ones to the remaining areas. (b) Temperature dependence of the magnetic scattered intensity averaged over the ⟨001⟩ Bragg peak positions (black curve) and outside them (red curve). (c) and (d) are radial scans over the ⟨001⟩ Bragg peaks (black) and the remaining region (red) for $T = T_C - 0.1$ K and $T = T_C + 0.1$ K respectively. The solid lines are fits to the Ornstein-Zernike equation (eq. 4.1 in the text).

For $T \leq T_C$ two discrete Bragg peaks emerge along the ⟨001⟩ crystallographic directions, characteristic of the helical long range order, on top of diffuse scattering that persists below T_C. In order to analyse the different contributions to the scattering pattern, we defined areas of interest over which the scattered intensity was averaged. For this purpose, two black boxes were defined along the ⟨001⟩ directions, and two red boxes for the rest, as shown in Fig. 4.1(a) at $T_C - 0.1$ K. Figure 4.1(b) displays the resulting temperature dependence of the intensities. Above T_C, the scattered intensity is the same for all areas of interest, and increases continuously with decreasing temperature. At T_C, the intensity over the ⟨001⟩ positions shows a jump by almost one order of magnitude within 0.1 K due to the appearance of the helical Bragg peaks. This is an indication of a first-order phase transition. On the other hand, the scattering outside the Bragg positions shows a cusp at T_C. At lower temperatures, all intensities reach a plateau with the diffuse scattering being about three orders of magnitude lower than the intensity

of the Bragg peaks.

The resulting Q-dependence of the scattered intensities is shown in the radial Q scans of Figs. 4.1(c) and (d) for $T_C - 0.1$ K and $T_C + 0.1$ K, respectively. Similar analysis was also performed for the SANS patterns obtained on IN15 leading to the $S(Q)$ curves shown in Fig. 4.2(a). Below T_C, the typical Gaussian-shaped Bragg peak is superimposed on a weak diffuse scattering that is the same as the scattering outside the ⟨001⟩ directions.

Above T_C the two regions of the radial averaging give the same results, with a broad Q-dependence that can be fitted by the Ornstein-Zernike Lorentzian shape:

$$S(Q) \quad \propto \quad \frac{C}{(Q-\tau)^2 + 1/\xi^2} \tag{4.1}$$

with C the Curie-Weiss constant and ξ the correlation length. The temperature dependences of the fitting parameters τ and ξ are presented in Fig. 4.2(b) and (c) respectively, where PAXY and IN15 give consistent results.

The temperature dependence of the helical modulation wave vector τ, shown in Fig. 4.2(b), is weak. On the other hand, the correlation length ξ shown in Fig. 4.2(c) increases continuously with decreasing temperature. At $T_C + 0.5$ K ξ is ~ 20 nm, which amounts to $\sim \ell/3$, whereas at T_C $\xi \sim \ell$. Below T_C, the analysis of the diffuse scattering leads to a decrease of ξ and $\xi \sim 20$ nm at $T_C - 0.1$ K.

The temperature dependence of the correlation length ξ follows the formula [16, 19]:

$$\xi(T) = \xi_{Gi} \sqrt{\frac{2^{1/3}[1-\epsilon^3 + (\sqrt{1-2\epsilon^3})^{1/3}]}{\epsilon + (1-\epsilon^3 + \sqrt{1-2\epsilon^3})^{1/3}]^2}} \tag{4.2}$$

with $\epsilon = (T - T_{MF})/T_0$, T_{MF} the mean-field temperature, ξ_{Gi} the Ginzburg length corresponding to the correlation length at T_{MF}. The fit leads to the dashed line in Fig. 4.2(c). The Ginzburg length obtained from the fit is $\xi_{Gi} = 20 \pm 8$ nm, comparable to $\xi_{Gi} \sim 8.5$ nm obtained from susceptibility measurements [12]. Thus it seems that $\xi_{Gi} \sim \xi_{DM}$ with the chiral DM length given by $\xi_{DM} = 1/\tau \approx 10$ nm. As a result, we conclude that the relation $\xi_{Gi} \gg \xi_{DM}$, required by the Brazovskii's theory to apply, is not fulfilled for Cu_2OSeO_3, which is consistent with the conclusions drawn in Ref. [12].

The dynamics of the magnetic correlations were measured with neutron spin echo spectroscopy, leading to the intermediate scattering functions $I(Q = \tau, t)$ for different temperatures, shown in Fig. 4.3(a). Above T_C the fluctuations decay exponentially with characteristic time t_0. This exponential decay is superimposed on an elastic fraction due to the scattering of the Bragg peaks, which leads

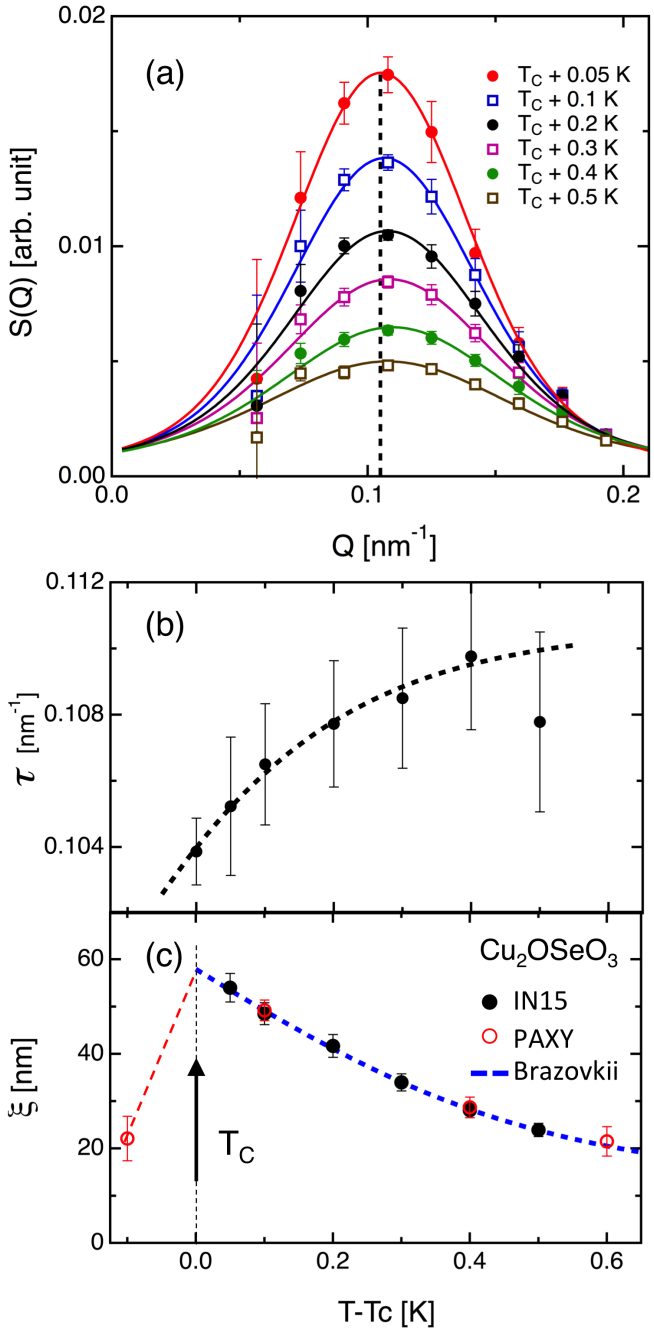

Figure 4.2: (a) SANS intensity as a function of Q obtained after radial averaging over the areas outside the Bragg conditions for various temperatures close to T_C. The data have been obtained on IN15. The solid lines are fits to the Ornstein-Zernike equation (eq. 4.1). (b) and (c) show the temperature dependence of τ and the correlation length ξ, respectively. The open and solid symbols denote the data from the PAXY and IN15 measurements respectively. The blue dashed line is the fit to eq. 4.2.

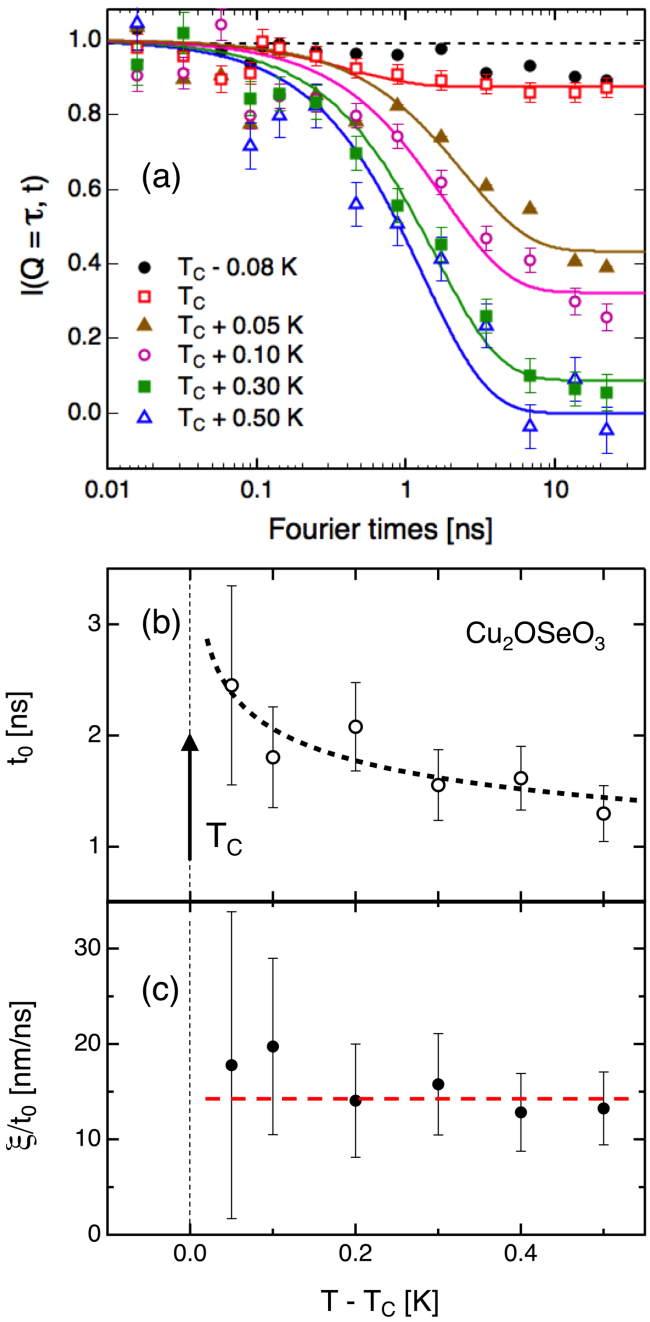

Figure 4.3: Neutron spin-echo spectroscopy results. (a) Intermediate scattering function I($Q = \tau$, t) for various temperatures close to T_C, (b) Characteristic relaxation time t_0 deduced from exponential fits to eq. 4.3. (c) ξ / t_0 as a function of temperature. The dashed lines connecting the data points in (b) and (c) are guides to the eyes.

to an elastic term α. Consequently, the NSE spectra were fitted by the function:

$$I(Q=\tau,t) \quad = \quad (1-\alpha)\exp(-t/t_0)+\alpha \tag{4.3}$$

The elastic term α evolves rapidly from 30% to 100% within 0.1 K following the rapid jump of the Bragg peak intensity at T_C. The characteristic relaxation time t_0 is shown in Fig. 4.3(b) and increases slowly with decreasing temperature from ~ 1.5 ns at $T_C + 0.5$ K to ~ 2.5 ns at T_C. This increase matches the temperature dependence of ξ, as displayed in Fig. 4.3(c), where the ratio ξ/t_0 is almost independent of the temperature.

On IN15 it was also possible to measure the chirality of the magnetic correlations with polarised neutrons following eq. 2.9. Figure 4.4(a-d) shows the scattering patterns obtained with opposite incoming beam polarisations in the detector plane. Below T_C the scattering patterns show Bragg peaks along the equivalent $\langle 001 \rangle$ directions and their appearance depends on the incoming beam polarisation. For $\vec{P} \parallel \hat{x}$, the scattering pattern in Fig. 4.4(b) shows Bragg peaks only at [010] and [00$\bar{1}$] crystallographic axes, whereas these are almost extinct for $\vec{P} \parallel -\hat{x}$ as shown by the pattern in Fig. 4.4(a). This is characteristic of a right-handed chiral helix. Above T_C, the ring-shape diffuse scattering in Fig. 4.1(a) for unpolarised neutrons reduces to half-moons that orient towards right-side for $\vec{P} \parallel \hat{x}$ and left-side for $\vec{P} \parallel -\hat{x}$, as illustrated in Fig. 4.4(d) and (c), respectively.

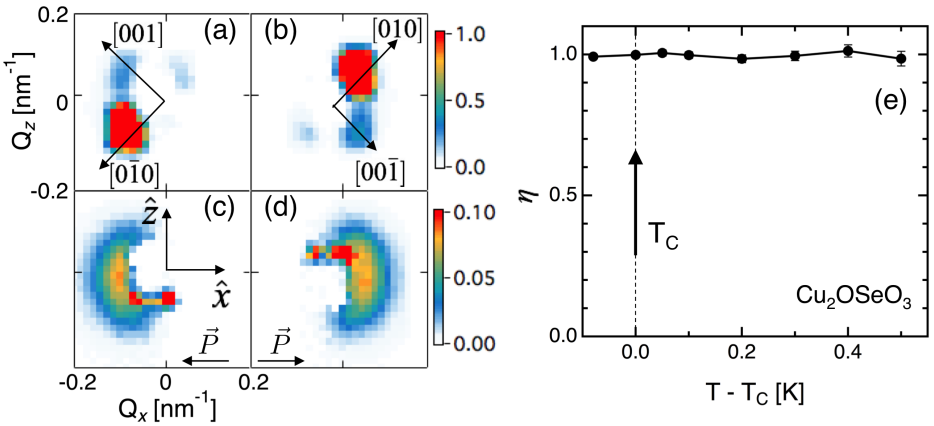

Figure 4.4: Scattering patterns of Cu_2OSeO_3 at $T_C - 0.1$ K (a-b) and $T_C + 0.3$ K (c-d) with opposite incoming beam polarisations. (e) Temperature dependence of magnetic chirality η at zero field in the vicinity of T_C.

The effect of chiral magnetic scattering on the cross section is quantitatively represented by the chirality η given in Figure 4.4(e), which was calculated following eq. 2.13. Below T_C, Cu_2OSeO_3 has a single domain right-handed chirality with $\eta = 1$. This high value of η persists also above T_C, in accordance with the half-moon diffuse scattering patterns that remain up to $T_C + 0.5$ K, where $\xi \sim \ell/3$. Above this temperature the scattering is very weak and background corrections become important, hindering an accurate determination of η.

As in MnSi, precursor phenomena with fully chiral correlations exist above T_C also in Cu_2OSeO_3. A theoretical estimation of the temperature window for the precursor phase has been provided in Ref. 7 and is about $\Delta T \sim 1$ K for Cu_2OSeO_3. This is comparable with the temperature range obtained experimentally, of $\Delta T \sim 0.5$ K for the fully chiral ring-shape scattering above T_C and of $\Delta T \sim 0.3$ K between the peak and the broad maximum in the specific heat measurements [11].

4.4. MAGNETIC PHASE DIAGRAM AND SKYRMION LATTICE SCATTERING

Figure 4.5 displays a contour plot of the scattered neutron intensity for $\vec{B} \parallel \vec{k}_i$, i.e. along the neutron beam propagation direction, illustrating the magnetic field-temperature ($B - T$) phase diagram deduced from the SANS patterns. At high temperatures, the magnetic scattering is weak and negligible for all magnetic fields. Below T_C, the scattering from the helical phase weakens with increasing magnetic field and almost vanishes above B_{C1} seen by the change of the colour codes from yellow to light blue. This is characteristic of a transition to the conical phase, the scattering of which does not fulfill the Bragg condition for $\vec{B} \parallel \vec{k}_i$. Furthermore, a red pocket delimited by the lines B_{A1} and B_{A2} appears just below T_C and is the signature of the skyrmion lattice phase.

The effect of the crystal lattice orientation on the scattering patterns of the helical and skyrmion lattice phases for $T = 57.2$ K were investigated by rotating the sample every 5° between 0° and 90° using the four different protocols schematically illustrated in the first column of Fig. 4.6.

(a) The measurements were performed at zero magnetic field to provide a reference of the crystal lattice orientation. The resulting scattering patterns of the helical phase are shown in Fig. 4.6(a). The angle $\psi = 0°$ corresponds to the orientation where four Bragg peaks are observed along two equivalent ⟨100⟩ crystallographic directions, which are along the diagonals of the detector. On the other hand, by rotating the sample over 90°, at $\psi = 90°$, the third equivalent ⟨100⟩ crystallographic direction fulfils the Bragg condition, and two Bragg peaks appear along the horizontal direction. The weaker intensity observed for $\psi = 90°$ is

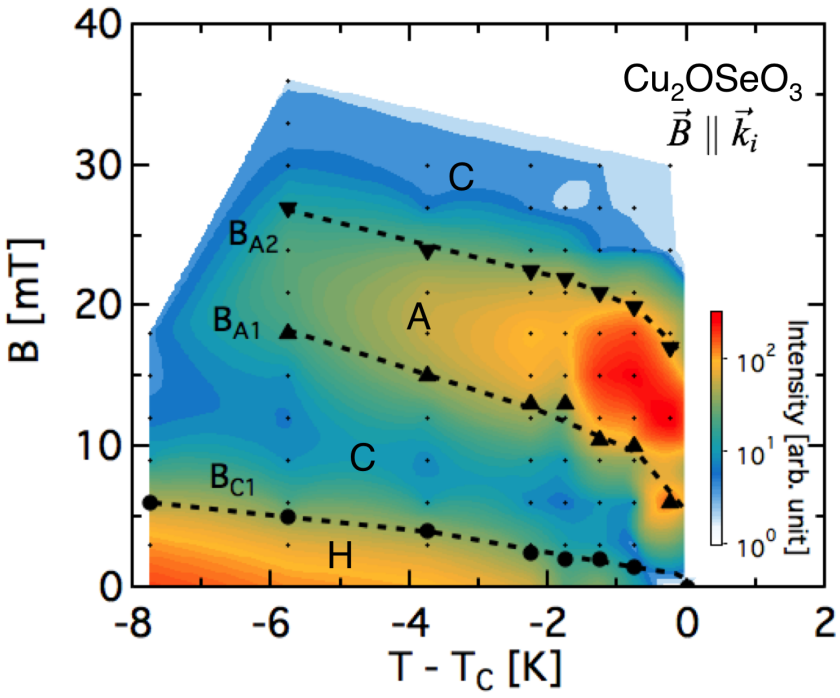

Figure 4.5: Contour plot of the neutron scattered intensity for $\vec{B} \parallel \vec{k}_i$ illustrating the $B-T$ magnetic phase diagram of Cu_2OSeO_3 close to T_C. The colour code quantifies the scattered intensity and can be used to identify the helical (H), conical (C) and the A-phase (A). In the contour plot, the phase boundaries between the phases, B_{C1}, B_{A1} and B_{A2} are also indicated. The black dots indicate the magnetic fields and temperatures at which the measurements were performed.

4

due to a slight misalignment of the sample. At the intermediate angles, such as $\psi = 20°$ and 80°, the scattering is typically background.

(b) The sample rotation took place at zero magnetic field. At each position, a magnetic field of 20 mT was applied and the scattering patterns, shown in Fig. 4.6(b), were recorded. At $\psi = 0°$, the scattering pattern does not contain six peaks but twelve separated by 30°, of which four appear along the ⟨100⟩ directions. At $\psi = 20°$, the twelve peaks merge to six broad spots, and there is indication for slight rotation of the pattern. At $\psi = 80°$, the six broad spots rotate further and at $\psi = 90°$, the peaks are sharper and two of them are along the horizontal ⟨100⟩ direction.

(c) The magnetic field of 20 mT was kept constant during the rotation of the sample from $\psi = 0°$ to 90°. The resulting scattering patterns are shown in Fig. 4.6(c), where at $\psi = 0°$ the scattering pattern is the same as for the previous

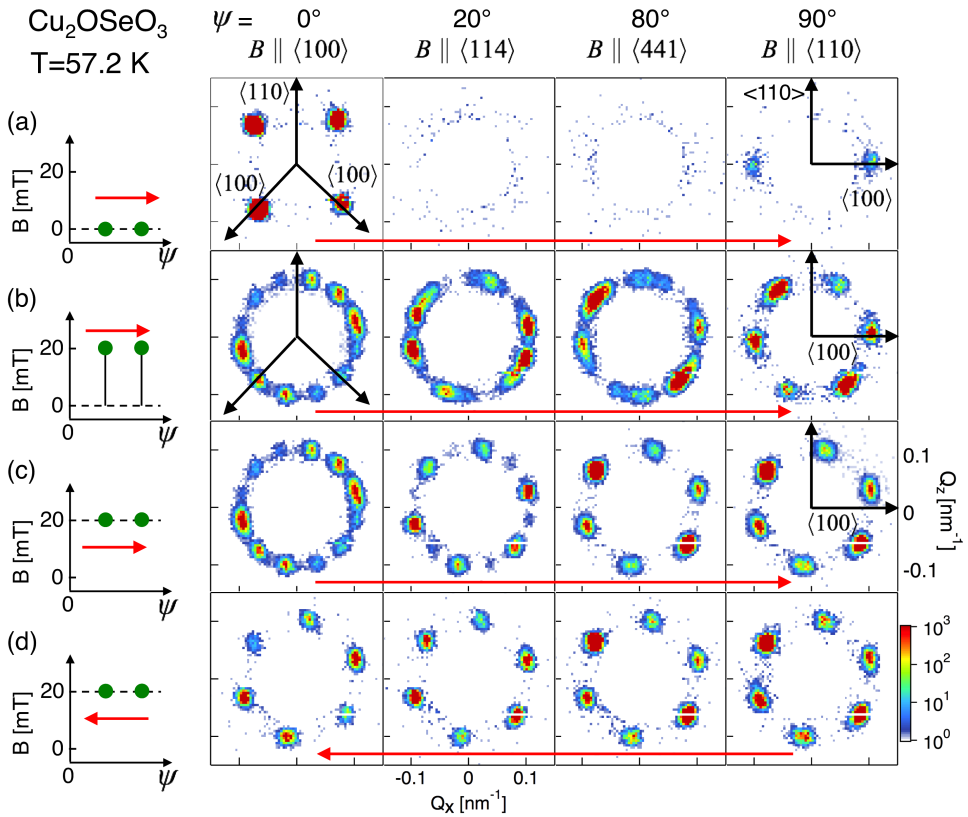

Figure 4.6: Magnetic scattering patterns of Cu_2OSeO_3 for various sample orientations designated by the angle ψ recorded at PA20 and for (a) zero field and (b-d) $B = 20$ mT at $T = 57.2$ K. The magnetic field is fixed along the beam propagation direction and thus perpendicular to the detector plane. The sample was rotated along the vertical ⟨110⟩ direction with a step of 5°. Its rotation direction and the measurement procedure are schematically illustrated by the drawings in the first column. In panel (a), the sample rotation and the measurements were performed at zero field. In panel (b) the sample was rotated at zero field every 5°, then a magnetic field of $B = 20$ mT was applied and the scattering patterns were recorded. The magnetic field was then set back to zero and the sample was rotated to the next position. In panels (c) and (d) the magnetic field stayed at 20 mT during sample rotation and signal recording. The sample was rotated from $\psi = 0°$ to 90° for the measurements in panels (a-c) and inversely from $\psi = 90°$ to 0° for the measurements in panel (d).

case. However, at $\psi = 20°$, the scattering pattern is very different from the one recorded in the previous protocol. In this scattering pattern, the peaks do not merge nor rotate, but six of them become stronger while the other six weaken. This is more pronounced for $\psi = 80°$, where only six of the original twelve peaks remain. The scattering pattern remains the same at $\psi = 90°$, and in this case no peaks appear along the horizontal ⟨100⟩ direction, which is different from the measurements of (b).

(d) After the measurements of (c), the sample was rotated back from $\psi = 90°$ to 0° always under the same magnetic field of 20 mT. In this case, the scattering pattern observed previously at $\psi = 90°$ remains the same during the rotation, and at $\psi = 0°$ the twelve peaks are not recovered.

These results show that the scattering of the skyrmion lattice phase is always present independently of the orientation of the magnetic field with respect to the crystallographic lattice. However the specific scattering pattern depends on the sample orientation and the magnetic history. The patterns of Fig. 4.6(b) are the same as those that would have been recorded after zero field cooling the sample. The number of peaks and their orientation are determined by the sample orientation, with twelve peaks when two ⟨100⟩ crystallographic directions are in the scattering plane and six peaks otherwise. Furthermore, both at $\psi = 0°$ and 90° skyrmion lattice peaks appear along the ⟨100⟩ crystallographic directions.

When the sample was rotated at a constant magnetic field, very different scattering patterns were found. The twelve peaks at $\psi = 0°$ split to two domains, one with strong and the other one with weak intensities. The intensity of the weak domain decreases with increasing ψ and is almost zero at $\psi = 80°$. On the other hand, the scattering of the dominant domain persists with the same orientation as at $\psi = 0°$, independently of the sample rotation. Thus at $\psi = 90°$ the scattering pattern is different from the one obtained in the (b) series of the measurements, indicating a metastable state.

The dependence of the scattering patterns on the sample orientation suggests a coupling between the skyrmion and the crystal lattices. This coupling originates from weak anisotropy produced by high-order spin-orbital coupling, which defines a preferred orientation of the skyrmion lattice, as also theoretically predicted for MnSi [1] and $Fe_{1-x}Co_xSi$ ($x = 0.2$) [20]. However, it is not clear why (one or more) specific crystallographic direction dominates the scattering pattern and which mechanism induces the change from one equivalent crystallographic direction to another, revealed by our experimental findings.

4.5. MAGNETIC RELAXATION UNDER MAGNETIC FIELDS

By rapidly changing the magnetic field, the response of the sample was followed by recording the scattering patterns as a function of time. Figure 4.7 shows

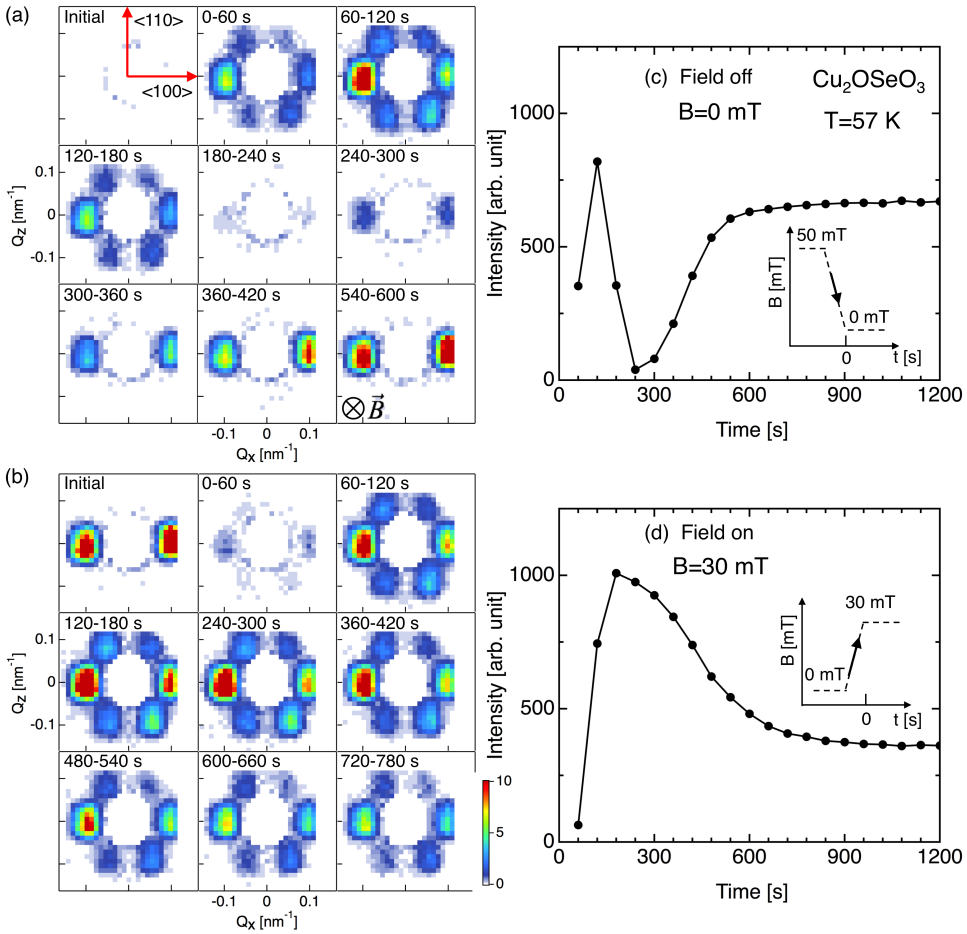

Figure 4.7: Time dependence of the scattering patterns and the corresponding integrated intensity recorded at IN15 and $T = 57$ K for Cu_2OSeO_3 after fast changing the magnetic field. Panels (a) and (c) show the results obtained after switching off the magnetic field from 50 mT to 0 mT. Panels (b) and (d) correspond to the results obtained after increasing the magnetic field from 0 mT to 30 mT. The measurements were performed once the magnetic field reached the setting values. Each scattering pattern was recorded over 60 seconds.

the scattering patterns and the scattered intensity integrated over the whole detector at $T = 57$ K for rapidly switching off or on the magnetic field. The magnetic field changed within ~ 40 s, and each pattern was the sum of the scattering over 60 seconds.

(a) The sample was initially stablized at $B = 50$ mT. The magnetic field was then switched off to $B = 0$ mT, and the scattering patterns shown in Fig. 4.7(a), were recorded. The reference initial state is the scattering at 50 mT before changing the magnetic field and the pattern is practically background. After turning off the magnetic field, a variety of different scattering patterns are observed as a function of time. In the first 60 s, the scattering pattern shows six Bragg peaks, typical for skyrmion lattice correlation. This pattern persists for $60 < t < 120$ s with enhanced intensity. At $120 < t < 180$ s, the intensity weakens and at $180 < t < 240$ s only two weak peaks appear along the ⟨100⟩ direction. This indicates a slow transition from skyrmion lattice to conical, and then to helical correlations. As time goes on, the horizontal Bragg peaks become stronger and reach saturation for $t \gtrsim 600$ s.

(b) After the measurements of (a), the magnetic field was switched on from 0 to 30 mT, leading to the scattering patterns shown in Fig. 4.7(b). In this case, the initial state is the helical phase at zero field, with two Bragg peaks along the horizontal ⟨100⟩ direction. After switching on the magnetic field to $B = 30$ mT, the scattering pattern over $0 < t < 60$ s shows very weak six spots. These become more intense at $60 < t < 120$ s, indicating clearly skyrmion lattice correlations. With increasing time, the scattering pattern remains unchanged but the intensity increases slightly. For $t \gtrsim 660$ s, the scattering does not depend on time.

The resulting time dependence of the scattered intensity shown in Fig. 4.7 (c) and (d) follows the change of the scattering patterns. At $B = 0$ mT, the scattered intensity increases with increasing time and reaches a maximum at $t \sim 120$ s. This corresponds to the appearance of the skyrmion lattice pattern. By further increasing time, the scattered intensity decreases and at $t = 240$ s it reaches a minimum of almost zero intensity as expected for the scattering of the conical phase. As time goes on, the intensity increases again and approaches a plateau for $t \gtrsim 600$ s where the helical peaks appear.

At $B = 30$ mT, the scattered intensity increases with time due to the appearance of the skyrmion lattice peaks. It reaches a maximum at $t \sim 180$ s and then gradually decreases, levelling off to a plateau for $t \gtrsim 700$ s. This is consistent with the weakening of the skyrmion lattice scattering patterns.

The time dependence of the scattered intensity for other temperatures is given in Fig. 4.8, and shows similar trends as for $T = 57$ K. The scattering patterns are not shown as they are similar to those at 57 K.

These results reveal a delayed response of the magnetic scattering after a

rapid change of the magnetic field, which follows the phases of the phase diagram: helical, conical and skyrmion lattice. The slow relaxation indicates macroscopic time scales, which may be related to the glassy behaviour observed for Cu_2OSeO_3 with Lorentz TEM [21] and the AC magnetic susceptibility results given in *Chapter* 3.

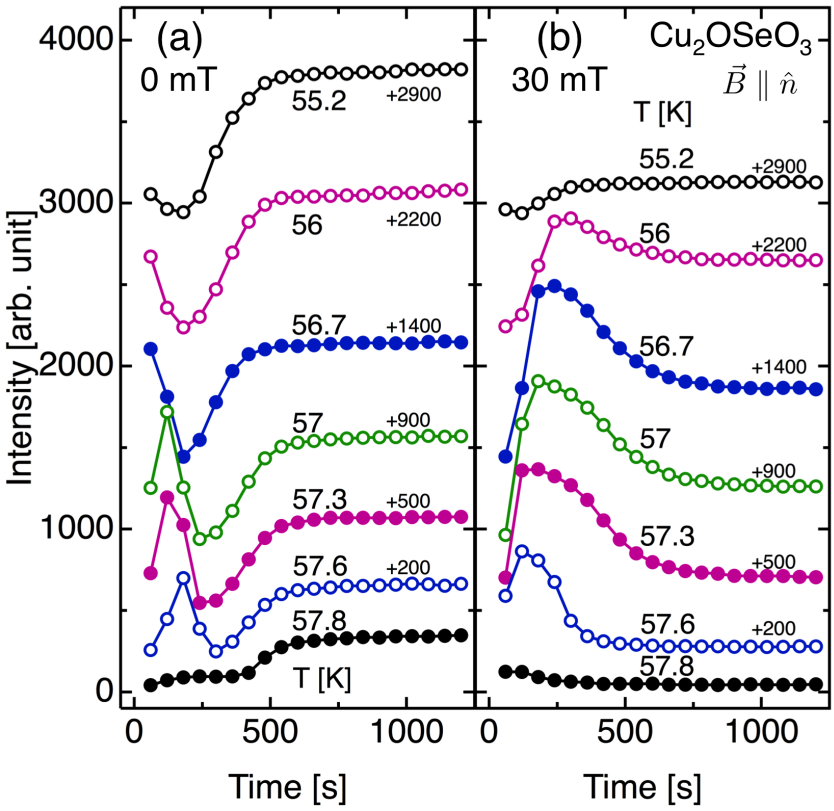

Figure 4.8: Time dependence of the integrated neutron intensity recored at IN15, for various temperatures close to T_C for (a) $B = 0$ mT after switching off the magnetic field from 50 mT and (b) $B = 30$ mT after fast raising from 0 mT. For the sake of clarity, the curves have been shifted by the values indicated.

4.6. DISCUSSION

The neutron scattering measurements presented above reflect the temperature and magnetic field dependences of the magnetic correlations close to T_C and thus complement the AC susceptibility results discussed in *Chapter* 3. At

zero field, the intensity at the positions of the Bragg peaks as well as the fraction of the elastic scattering seen by NSE increase sharply at T_C. Both findings indicate a first order phase transitionat T_C, in agreement with the peak in specific heat at T_C reported in the literature [10, 11].

Above T_C, a weak ring of diffuse scattering appears centred at τ, which reaches its highest intensity at T_C. This diffuse scattering intensity persists, although weak, below T_C and coexists with the long-range helical correlations. The associated correlation length does not diverge at T_C but remains significantly lower than the helix pitch ℓ both above and below T_C. These experimental findings share similarities with MnSi [14–16].

Dynamic scaling relates correlated lengths to relaxation times, as $t_0 \propto \xi^z$, with z the dynamic critical exponent [22]. In Cu_2OSeO_3 we obtain $z \approx 1$, a value similar to that reported for MnSi [15] but much lower than for 3D ferromagnets ($z = 5/2$) or antiferromagnets ($z = 3/2$). As in MnSi, such a low z value may indicate a reduced spin dimensionality for the spin fluctuations above T_C in Cu_2OSeO_3.

It has been suggested that the helimagnetic transition at zero field is governed by a hierarchy of characteristic lengths reflecting the relative strength of the interactions [16, 19]: the Ginzburg length ξ_{Gi}, the Dzyaloshinsky-Moriya (DM) length ξ_{DM}, and ξ_{cub} the length associated with the cubic anisotropy. The Ginzburg length quantifies the strength of the interactions between the magnetic fluctuations, which are strong in the limit of $\xi_{Gi} > \xi(T)$, whereas they can be considered as a perturbation in the other limit $\xi(T) < \xi_{Gi}$. The DM length is related to the pitch of the helix ℓ by $\xi_{DM} = \ell/2\pi$ and the cubic anisotropy length reflects the influence of the cubic anisotropy. If the Ginzburg length is much larger than the length scale associated with the DM interaction, i.e. $\xi_{Gi} \gg \xi_{DM}$, the interactions between the fluctuations should govern the behavior close to the transition, driving it to first order as suggested by Brazovskii [19]. Also for $\xi_{Gi} < \xi_{DM}$ the transition is driven by fluctuations and expected to be of first order following the Bak and Jensen (1980) approach [9] in this so called Wilson-Fisher renormalization group limit [23]. So far, the helimagnetic transition and the role of the characteristic lengths remain largely unexplored and have only been discussed for the case of MnSi [16], $Fe_{1-x}Co_xSi$ [24] and Cu_2OSeO_3 based on susceptibility results [12].

In Cu_2OSeO_3 we obtain $\xi_{Gi} > \xi_{DM}$ from both SANS and susceptibility, which is similar to $Fe_{1-x}Co_xSi$ [24]. However, this is different from MnSi, where the characteristic lengths fulfil the sequence $\xi_{cub} \gg \xi_{Gi} \gg \xi_{DM}$, requested by Brazovskii's theory. Thus it seems that the helimagnetic transition at zero field does not follow a universal behaviour for all chiral helimagnets.

Under magnetic fields, the skyrmion lattice phase scattering patterns show

either a six-fold or a twelve-fold symmetry depending on the crystallographic orientation, magnetic and thermal history in agreement with literature [18]. These results are different from most chiral magnets such as MnSi [1] and FeGe [25], where only the six-fold symmetry has been found. Our results show that the scattering of the skyrmion lattice depends not only on the orientation of the crystallographic lattice but also on the magnetic history.

By changing the orientation of the crystallographic lattice with respect to the magnetic field, the skyrmion lattice scattering pattern changes but always shows a preferred orientation along the easy axes ⟨100⟩. Similar behaviour has also been found in MnSi [1], along the ⟨110⟩ axis, and in $Fe_{1-x}Co_xSi$ ($x = 0.2$) [20]. In the later case the easy axis is the same as in Cu_2OSeO_3, i.e. along ⟨100⟩, but the preferred orientation of the skyrmion lattice can be along either ⟨100⟩ or ⟨110⟩. Our results show that in Cu_2OSeO_3 by rotating the sample in a constant magnetic field, the scattering pattern changes from a twelve-fold to a six-fold symmetry. However, by rotating the sample backwards, the six-fold symmetry pattern persists unchanged and the twelve-fold scattering pattern is not recovered. This indicates the onset of a metastable state stabilised by magnetocrystalline anisotropy. The role of this anisotropy is also highlighted by the delayed response of the magnetic scattering found after a rapid change of the magnetic field. These results may trigger new theoretical work, that may provide a quantitative description of the underlying microscopic processes.

4.7. CONCLUSION

High resolution SANS and NSE measurements on Cu_2OSeO_3 have been used to investigate the magnetic correlations and precursor phenomena close to T_C. The results at zero field show a first order helimagnetic transition at T_C and chiral short range correlations above T_C, similarly to MnSi. The SANS measurements under magnetic fields and in the skyrmion lattice phase indicate a coupling between the skyrmion and the chemical lattices. In addition, by rapidly changing the magnetic field, time dependent scattering patterns have been found corresponding to different phases of the magnetic phase diagram.

REFERENCES

[1] S. Mühlbauer, B. Binz, F. Jonietz, C. Pfleiderer, A. Rosch, A. Neubauer, R. Georgii, and P. Böni, *Skyrmion lattice in a chiral magnet,* Science **323**, 915 (2009).

[2] X. Z. Yu, N. Kanazawa, Y. Onose, K. Kimoto, W. Z. Zhang, S. Ishiwata, Y. Mat-

sui, and Y. Tokura, *Near room-temperature formation of a skyrmion crystal in thin-films of the helimagnet FeGe,* Nat Mater **10**, 106 (2010).

[3] X. Z. Yu, Y. Onose, N. Kanazawa, J. H. Park, J. H. Han, Y. Matsui, N. Nagaosa, and Y. Tokura, *Real-space observation of a two-dimensional skyrmion crystal,* Nature **465**, 901 (2010).

[4] J.-W. G. Bos, C. V. Colin, and T. T. M. Palstra, *Magnetoelectric coupling in the cubic ferrimagnet Cu_2OSeO_3,* Phys. Rev. B **78**, 094416 (2008).

[5] V. Dyadkin, K. Prša, S. V. Grigoriev, J. S. White, and P. Huang, *Chirality of structure and magnetism in the magnetoelectric compound Cu_2OSeO_3,* Phys. Rev. B **89**, 140409(R) (2014).

[6] J. H. Yang, Z. L. Li, X. Z. Lu, M. H. Whangbo, S.-H. Wei, X. G. Gong, and H. J. Xiang, *Strong Dzyaloshinskii-Moriya Interaction and Origin of Ferroelectricity in Cu_2OSeO_3,* Phys. Rev. Lett. **109** (2012).

[7] O. Janson, I. Rousochatzakis, A. A. Tsirlin, M. Belesi, A. A. Leonov, U. K. Roessler, J. van den Brink, and H. Rosner, *The quantum nature of skyrmions and half-skyrmions in Cu_2OSeO_3,* Nat Comms **5** (2014).

[8] J. Romhányi, J. van den Brink, and I. Rousochatzakis, *Entangled tetrahedron ground state and excitations of the magnetoelectric skyrmion material Cu_2OSeO_3,* Phys. Rev. B **90**, 140404 (2014).

[9] P. Bak and M. H. Jensen, *Theory of helical magnetic structures and phase transitions in MnSi and FeGe,* J. Phys. C: Solid State Phys. **13**, L881 (1980).

[10] T. Adams, A. Chacon, M. Wagner, A. Bauer, G. Brandl, B. Pedersen, H. Berger, P. Lemmens, and C. Pfleiderer, *Long-Wavelength Helimagnetic Order and Skyrmion Lattice Phase in Cu_2OSeO_3,* Phys. Rev. Lett. **108**, 237204 (2012).

[11] V. A. Sidorov, A. E. Petrova, P. S. Berdonosov, V. A. Dolgikh, and S. M. Stishov, *Comparative study of helimagnets MnSi and Cu_2OSeO_3 at high pressures,* Phys. Rev. B **89**, 100403(R) (2014).

[12] I. Živković, J. S. White, H. M. Rønnow, K. Prša, and H. Berger, *Critical scaling in the cubic helimagnet Cu_2OSeO_3,* Phys. Rev. B **89**, 060401(R) (2014).

[13] F. Qian, H. Wilhelm, A. Aqeel, T. Palstra, A. Lefering, E. Brück, and C. Pappas, *Phase diagram and magnetic relaxation phenomena in Cu_2OSeO_3,* Phys. Rev. B **94**, 064418 (2016).

[14] S. M. Stishov, A. E. Petrova, A. A. Shikov, T. A. Lograsso, E. I. Isaev, B. Johansson, and L. L. Daemen, *Lost Heat Capacity and Entropy in the Helical Magnet MnSi,* Phys. Rev. Lett. **105**, 236403 (2010).

[15] C. Pappas, E. Lelièvre-Berna, P. Bentley, P. Falus, P. Fouquet, and B. Farago, *Magnetic fluctuations and correlations in MnSi: Evidence for a chiral skyrmion spin liquid phase,* Phys. Rev. B **83**, 224405 (2011).

[16] M. Janoschek, M. Garst, A. Bauer, P. Krautscheid, R. Georgii, P. Böni, and C. Pfleiderer, *Fluctuation-induced first-order phase transition in Dzyaloshinskii-Moriya helimagnets,* Phys. Rev. B **87**, 134407 (2013).

[17] S. Seki, J. H. Kim, D. S. Inosov, R. Georgii, B. Keimer, S. Ishiwata, and Y. Tokura, *Formation and rotation of skyrmion crystal in the chiral-lattice insulator Cu_2OSeO_3,* Phys. Rev. B **85**, 220406(R) (2012).

[18] K. Makino, J. D. Reim, D. Higashi, D. Okuyama, T. J. Sato, Y. Nambu, E. P. Gilbert, N. Booth, S. Seki, and Y. Tokura, *Thermal stability and irreversibility of skyrmion-lattice phases in Cu_2OSeO_3,* Phys. Rev. B **95**, 134412 (2017).

[19] S. A. Brazovskii, *Phase transition of an isotropic system to a nonuniform state,* Soviet Journal of Experimental and Theoretical Physics **41**, 85 (1975).

[20] W. Münzer, A. Neubauer, T. Adams, S. Mühlbauer, C. Franz, F. Jonietz, R. Georgii, P. Böni, B. Pedersen, M. Schmidt, A. Rosch, and C. Pfleiderer, *Skyrmion lattice in the doped semiconductor $Fe_{1-x}Co_xSi$,* Phys. Rev. B **81**, 041203(R) (2010).

[21] J. Rajeswari, P. Huang, G. F. Mancini, Y. Murooka, T. Latychevskaia, D. McGrouther, M. Cantoni, E. Baldini, J. S. White, A. Magrez, T. Giamarchi, H. M. Rønnow, and F. Carbone, *Filming the formation and fluctuation of skyrmion domains by cryo-Lorentz transmission electron microscopy,* P Natl Acad Sci USA **112**, 14212 (2015).

[22] P. C. Hohenberg and B. I. Halperin, *Theory of dynamic critical phenomena,* Rev. Mod. Phys. **49**, 435 (1977).

[23] K. G. Wilson, *The renormalization group and critical phenomena,* Rev. Mod. Phys. **55**, 583 (1983).

[24] L. J. Bannenberg, K. Kakurai, P. Falus, E. Lelièvre-Berna, R. Dalgliesh, C. D. Dewhurst, F. Qian, Y. Onose, Y. Endoh, Y. Tokura, and C. Pappas, *Universality of the helimagnetic transition in cubic chiral magnets: Small angle neutron scattering and neutron spin echo spectroscopy studies of fecosi,* Phys. Rev. B **95**, 144433 (2017).

[25] E. Moskvin, S. Grigoriev, V. Dyadkin, H. Eckerlebe, M. Baenitz, M. Schmidt, and H. Wilhelm, *Complex Chiral Modulations in FeGe Close to Magnetic Ordering,* Phys. Rev. Lett. **110**, 077207 (2013).

5

LOW TEMPERATURE MAGNETISM OF Cu_2OSeO_3 BELOW 50 K: MAGNETISATION, SUSCEPTIBILITY AND NEUTRON SCATTERING STUDIES

The magnetic phase diagram of the chiral magnet Cu_2OSeO_3 has been investigated by DC magnetisation and AC susceptibility as well as neutron scattering for temperatures below 50 *K. Qualitatively different phase diagrams have been obtained by applying the magnetic field along the easy* ⟨100⟩ *or the hard* ⟨110⟩ *crystallographic directions, which may be related to the cubic anisotropy. Strong χ'' appears close to B_{C2}, but only below* 30 *K and is more pronounced when B is applied along* ⟨100⟩*. Complementary results have been obtained by neutron scattering. In addition, the transition from the helical to the conical phase seems to be a two-step process leading to two adjacent B_{C1} lines below* 50 *K. The frequency dependence of χ'' indicates the existence of very broad distributions of long relaxation times both at B_{C1} and B_{C2}.*

5.1. INTRODUCTION

In this chapter we investigate the $B-T$ phase diagram of Cu_2OSeO_3 at temperatures below 50 K by DC magnetisation and AC susceptibility spanning a large frequency range from 0.1 Hz up to 1 kHz. These measurements are complemented by small angle neutron scattering. For a comparison with theory the magnetic field has been applied along the easy ⟨100⟩ and the hard ⟨110⟩ crystallographic directions. Magnetic susceptibility shows that the B_{C1} transition from the helical to the conical phase splits in two distinct lines below 50 K. Furthermore, the transition to the field polarised state at B_{C2} is seen not only on the real component of the susceptibility, χ', but also on the imaginary one, χ'', most prominently for $B \parallel \langle 100 \rangle$ and below 30 K. Neutron scattering provides complementary information revealing the appearance of additional scattered intensity close to B_{C2} and below 30 K but only for $B \parallel \langle 100 \rangle$.

The results are discussed in view of theoretical predictions [1] derived by a quantum mechanical treatment of the S=1/2 spins and of the Cu^{2+} tetrahedra that are the building blocks of the magnetic structure of Cu_2OSeO_3. These are composed of three Cu(1) and one Cu(2) ions, and interact weakly between each other [1, 2]. Within each tetrahedron the spin of the single Cu(2) ion is antiparallel to the spins of the three Cu(1) ions, resulting in a total spin of S=1 and a magnetic moment of $\sim 0.5\ \mu_B$ per Cu^{2+} ion. This description is consistent with the quantum mechanical treatment of the S=1/2 spins and has profound implications on the magnetic properties. In particular, the low temperature phase diagram of Cu_2OSeO_3 is qualitatively different when a magnetic field is applied along the easy ⟨100⟩ crystallographic direction or not [1].

5

5.2. EXPERIMENTAL DETAILS

5.2.1. SAMPLE DETAILS

Three single crystals of Cu_2OSeO_3 prepared by chemical vapour transport method [3, 4] were used for the measurements and their structure was checked by single crystal x-ray diffraction. Two samples with smaller dimensions of $\sim 1\times1\times1$ mm^3 were used for magnetic susceptibility measurements. Among them, one sample was oriented with the ⟨100⟩ crystallographic axis vertical and was the same as in the previous study [5]. The other sample was oriented with the ⟨110⟩ axis vertical. A much larger sample with dimensions of $\sim 5\times3\times3$ mm^3 was used for neutron scattering measurements with the ⟨110⟩ crystallographic axis along the vertical direction. The accuracy of the orientation for these samples was within ±5°.

5.2.2. DC MAGNETISATION AND AC SUSCEPTIBILITY

The magnetisation and magnetic susceptibility measurements were performed with a MPMS-5XL SQUID using the extraction method. The DC magnetic field B was applied along the ⟨100⟩ or ⟨110⟩ axis, as was the drive AC field B_{ac} = 0.4 mT with frequency ranging from 0.1 to 1000 Hz. The measurements yield the DC magnetisation M as well as the real and imaginary components of the AC susceptibility, χ' and χ'' respectively. Three specific experimental protocols were adopted in order to investigate the influence of magnetic history:

- Zero-field-cooled scans (ZFC): the sample was brought to the temperature of interest in zero field and then the measurements were performed by increasing stepwise the magnetic field.
- Field-cooled cooling scans (FCC): the sample was brought to 70 K, a magnetic field was applied and the signal was recorded by decreasing stepwise the temperature.
- Field-cooled warming scans (FCW): the sample was brought to 70 K, and then cooled down to 5 K in a magnetic field. The signal was recorded by increasing the temperature stepwise.

All measurements have been performed once the sample has reached thermal equilibrium.

5.2.3. NEUTRON SCATTERING

The neutron scattering measurements were performed on the small angle neutron scattering (SANS) instrument PA20 of the Laboratoire Léon Brillouin, using a wavelength of $\lambda = 6$ Å and $\Delta\lambda/\lambda = 10\%$. The position sensitive detector of 64×64 cm^2 with 0.5×0.5 cm^2 pixel resolution was placed at 12.7 m from the sample. A 10 T horizontal cryomagnet was used, that created a horizontal magnetic field $\vec{B}$ parallel or perpendicular to the incoming neutron beam wavevector $\vec{k}_i$. The magnetic field was applied along the ⟨100⟩ and ⟨110⟩ crystallographic directions. Background correction was performed using a measurement at 70 K where the magnetic scattering is negligible.

In order to compare the results with the literature, correction of the demagnetizing field has been performed assuming a spherical sample shape, which leads to the demagnetisation field $B_{dem} = D\mu_0 M$ with $D = 1/3$ for a sphere, $\mu_0 = 4\pi \cdot 10^{-7}$ T/(A/m) and M the magnetisation.

5.3. DC MAGNETISATION

Figure 5.1 displays the magnetic field dependence of the ZFC magnetisation M and its corresponding susceptibility $\Delta M/\Delta B$, deduced by numerical differen-

tiation, for a set of temperatures between 5 and 50 K. The results are given for B along the easy axis ⟨100⟩, in panels (a) and (b), and along the ⟨110⟩ axis, in panels (c) and (d).

For both orientations, M increases almost linearly with B at low fields. By further increasing the magnetic field, a kink appears in the magnetisation curves, which is more clearly seen as a peak in the derivative $\Delta M/\Delta B$ and marks the transition from the helical to the conical phase at the critical field B_{C1}. This peak is more pronounced at low temperatures and at 5 K it shifts to ~ 25 mT in agreement with the B_{C1} values reported in the literature [6–9].

At high fields, M levels off above B_{C2} and for both sample orientations it reaches a temperature dependent value M_{sat}, which at 5 K amounts to ~ 0.54 μ_B/-Cu^{2+} in agreement with literature [6–10]. The way M approaches M_{sat} depends on the sample orientation below 20 K, and this is more clearly seen in the $\Delta M/\Delta B$ curves. These show for $B \parallel \langle 100 \rangle$ a maximum centered at ~ 40 mT for 5 K, which is absent for $B \parallel \langle 110 \rangle$. Similar behaviour and differences between the two sample orientations have been reported in the literature [9].

Figure 5.2 displays the temperature dependence of the FCC and FCW magnetisation for some specific magnetic fields with $B \parallel \langle 100 \rangle$ in panel (a) and $B \parallel \langle 110 \rangle$ in panel (b). The ZFC data from the M vs B curves are included as well. For both orientations, the ZFC magnetisation is slightly lower than the FCC and FCW ones, which practically overlap. For all magnetic fields the magnetisation increases monotonically with decreasing temperature with the exception of 25 mT, where for both orientations a broad maximum occurs around 30 K, that corresponds to B_{C1}. Close to T_C all data follow the same generic curve that is reached at B = 55 mT for $B \parallel \langle 100 \rangle$ and 100 mT for $B \parallel \langle 110 \rangle$, and is accounted for by a modified power law [10]:

$$M_{sat}(T) = M_{sat}(0)\left[1 - \left(T/T_C^0\right)^n\right]^\beta \tag{5.1}$$

with $M_{sat}(0)$ the saturated magnetic moment at T = 0 K, n and β critical exponents, and T_C^0 the associated critical temperature. The fit leads to the continuous lines in Fig. 5.2. The fitting parameters are tabulated in Table 5.1 and are almost the same for the two sample orientations and in agreement with a previous study [10]. Close to T_C, Eq. 5.1 reduces to the simple power law (for n = 1) predicted theoretically [1], that mimics a 3D-Heisenberg behaviour. Deviations from these generic curves occur at temperatures and fields that correspond to the B_{C2} values determined from the inflection points of $\Delta M/\Delta B$ as derived from Fig. 5.1(b).

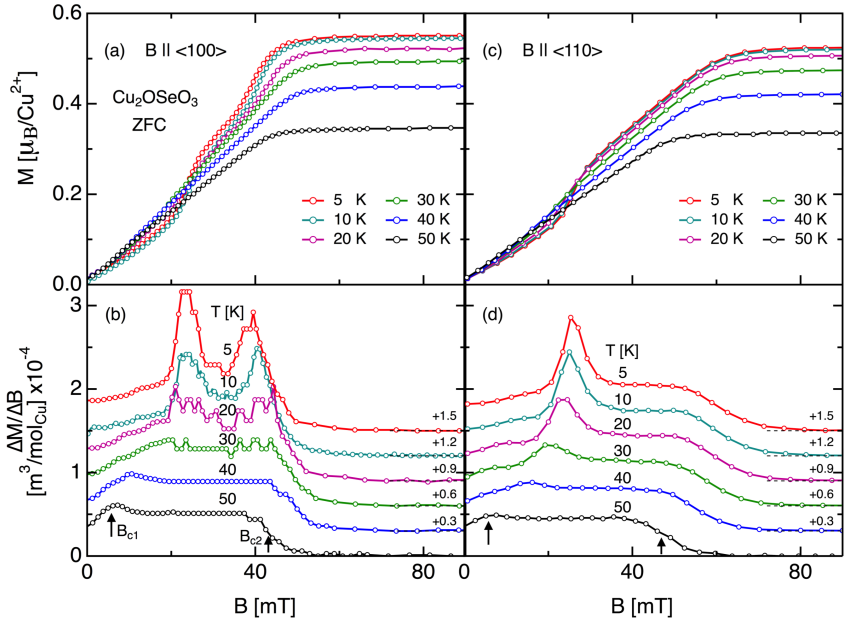

Figure 5.1: Magnetic field dependence of the ZFC magnetisation, panels (a) and (c), and of the deduced susceptibility $\Delta M/\Delta B$, panels (b) and (d), of Cu_2OSeO_3 between 5 K and 50 K for $B \parallel \langle 100 \rangle$, panels (a) and (b), and $B \parallel \langle 110 \rangle$, panels (c) and (d). The arrows to the 50 K curve in (b) indicate the critical fields B_{C1} and B_{C2} determined from the inflection points of $\Delta M/\Delta B$. For the sake of clarity the $\Delta M/\Delta B$ curves have been shifted vertically with respect to the base line as indicated.

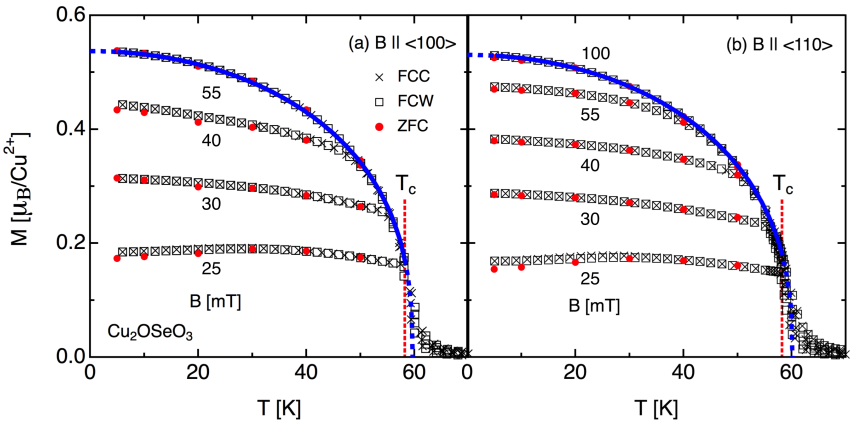

Figure 5.2: Temperature dependence of FCC and FCW magnetisation of Cu_2OSeO_3 at several magnetic fields for (a) $B \parallel \langle 100 \rangle$ and (b) $B \parallel \langle 110 \rangle$. The ZFC data from M vs B measurements are included as well. The blue lines in both panels are fits of eq. 5.1 with the parameters given in the text. The red vertical dashed lines indicate $T_C = 58.2$ K.

5.4. AC SUSCEPTIBILITY AT 10 HZ

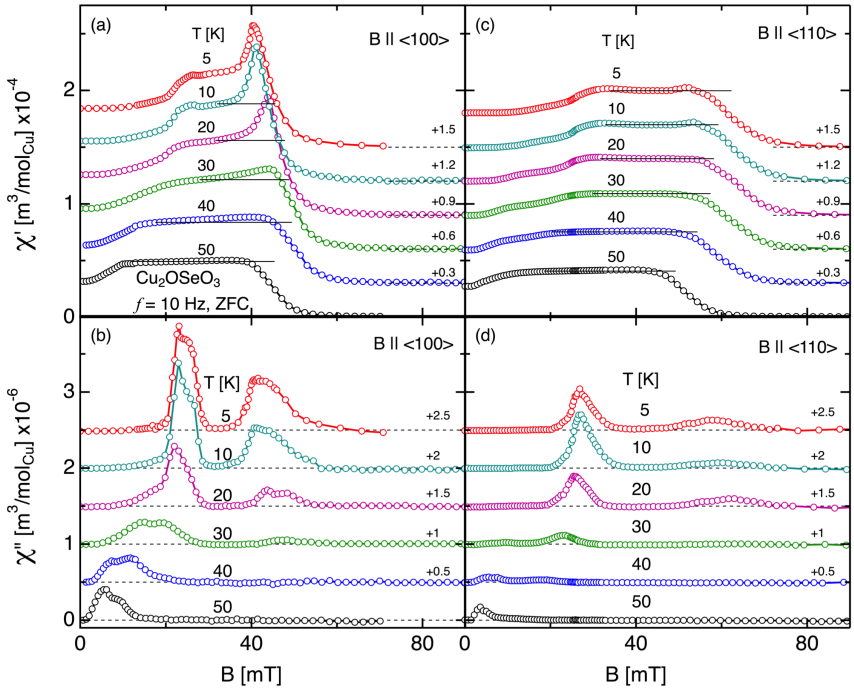

Figure 5.3: Magnetic field dependence of ZFC χ' and χ'' of Cu_2OSeO_3 at selected temperatures from 5 to 50 K at $f = 10$ Hz. Panels (a) and (b) correspond to $B \parallel \langle 100 \rangle$ and panels (c) and (d) to $B \parallel \langle 110 \rangle$. The horizontal lines in panels (a) and (c) are guides to the eye. All curves have been shifted vertically with respect to the base line as indicated.

5

Complementary information is provided by AC magnetic susceptibility which measures with high accuracy the frequency dependent field derivative of the magnetisation. Figure 5.3 illustrates the magnetic field dependence of ZFC χ' and χ'' at an intermediate frequency of $f = 10$ Hz for selected temperatures between 5 and 50 K. For both $B \parallel \langle 100 \rangle$ and $\langle 110 \rangle$ χ' increases slowly at low fields, following the same trend as $\Delta M/\Delta B$, but crosses over to a plateau-like behaviour characteristic of the conical phase, without a peak at B_{C1}. At 50 K, the plateau is horizontal for both field configurations, but at lower temperatures a slope sets in and below 30 K a peak develops at ~ 40 mT, which is very weak for $B \parallel \langle 110 \rangle$ but well pronounced for $B \parallel \langle 100 \rangle$.

The corresponding χ'' is shown in Figs. 5.3(b) and 5.3(d) for both orientations. Around B_{C1}, for $B \parallel \langle 100 \rangle$, χ'' seems to consist of two adjacent peaks,

which at 50 K are centred at 5 and 9 mT respectively. With decreasing temperature the amplitude of these peaks increases and their positions move to higher magnetic fields. At 5 K they occur at 23 and 25 mT respectively. These two peaks are also observed for $B \parallel \langle 110 \rangle$ but with relatively weaker intensity and occur simultaneously only between 40 and 30 K. Above B_{C1}, χ'' becomes zero for both orientations, with the exception of a broad maximum, which appears below 30 K and close to B_{C2} for $B \parallel \langle 100 \rangle$, a configuration where the peak of χ' develops as well. Similarly to the peak of χ', the peak of χ'' becomes more pronounced at lower temperatures. Weak signal was also found for $B \parallel \langle 110 \rangle$ close to B_{C2}, which might be due to a slight misalignment of the sample.

5.5. FREQUENCY DEPENDENCE OF ZFC AC MAGNETIC SUSCEPTIBILITY

The relaxation phenomena associated with B_{C1} and B_{C2} presented in the previous section are most visible for $B \parallel \langle 100 \rangle$ and in the following we will focus on the results obtained in this orientation. Figure 5.4 displays the ZFC χ' and χ'' for various frequencies at 40 and 5 K. The figure highlights the differences between $\Delta M/\Delta B$ and χ', as $\Delta M/\Delta B$ develops a peak around B_{C1} while χ' shows a smooth crossover to a plateau. Above B_{C1}, the AC and DC susceptibilities converge for both temperatures and overlap close to B_{C2}.

The frequency dependence of χ'' is given in Fig. 5.4 (b) and (d). At 40 K, χ'' shows two peaks which are located at 7 and 12 mT, thus close to B_{C1}. The amplitude of the peak at 7 mT decreases with increasing frequency, while the one at 12 mT slightly increases. At 284 Hz only the peak at 12 mT is visible. On the other hand, at 5 K these two χ'' peaks seem to merge as shown in Fig. 5.4(d) and vary very weakly with frequency. Close to B_{C2} the broad peak of χ'' shows a noticeable frequency dependence.

A quantitative analysis of the frequency dependence of χ' and χ'' is provided by the modified Cole-Cole formalism [11, 12]:

$$\chi(\omega) = \chi(\infty) + \frac{\chi(0) - \chi(\infty)}{1 + (i\omega\tau_0)^{1-\alpha}} \tag{5.2}$$

with $\omega = 2\pi f$ the angular frequency, $\chi(0)$ and $\chi(\infty)$ the adiabatic and isothermal susceptibilities respectively and $\tau_0 = 1/(2\pi f_0)$ the characteristic relaxation time with f_0 the characteristic frequency. The parameter α measures the distribution of characteristic relaxation times: $\alpha = 0$ corresponds to a single relaxation time, and $\alpha > 0$ to a distribution of relaxation times, which becomes broader as α approaches 1. Equation 5.2 leads to the in-phase and out-of-phase components

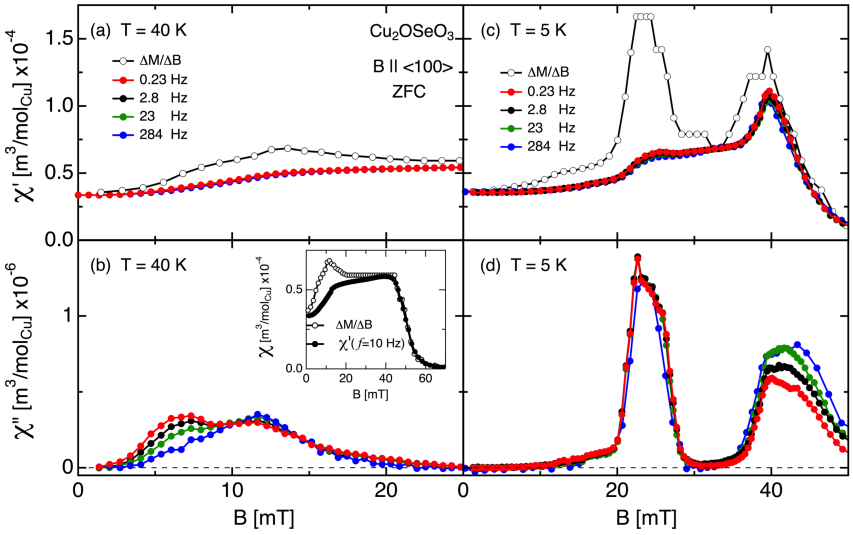

Figure 5.4: ZFC χ' and χ'' as a function of magnetic field at various frequencies for 40 K in panels (a) and (b), and 5 K in panels (c) and (d) with $B \parallel \langle 100 \rangle$. The DC susceptibility $\Delta M/\Delta B$ from Fig. 5.1(b) is included as well and the inset of (b) shows its variation beyond B_{C2} up to 70 mT for 40 K.

of the susceptibility, and a relation between these two quantities discussed in *Chapter* 3 and our previous report [5].

Figure 5.5 illustrates the frequency dependence of ZFC χ' and χ'' at 5 K for 25 and 40 mT. With increasing frequency, χ' decreases very weakly, only by ~ 3%, as seen in the panels (a) and (d). A more significant variation is found for χ'', which shows broad maxima at the characteristic frequencies $f_0 \sim 10$ Hz and 100 Hz for 25 and 40 mT, thus around B_{C1} and B_{C2} as seen in the panels (b) and (e), respectively.

The fit of the data to eq. 5.2 is illustrated by the solid lines in Fig. 5.5. It leads to $\alpha \sim 0.85$ and ~ 0.65 for $B = 25$ and 40 mT, respectively, thus revealing the existence of broad distributions of relaxation times. In addition, deviations from the simple Cole-Cole behaviour are found at low frequencies, as illustrated in Fig. 5.5(b), (c), (e) and (f). These may originate from the co-existence of several relaxation processes similarly to what has been reported at B_{C1} close to T_C [5] and over a larger temperature and magnetic field range in $Fe_{1-x}Co_xSi$ [13].

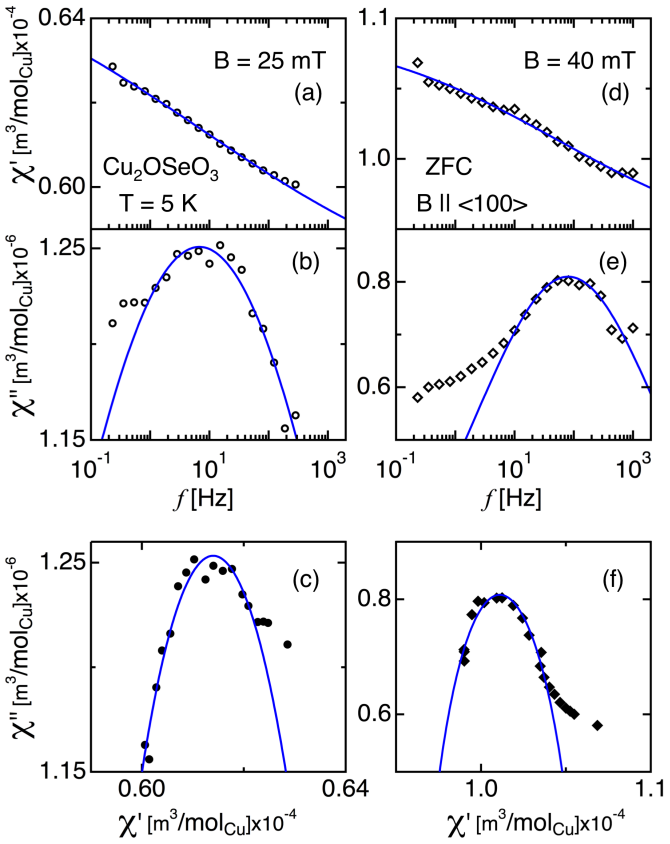

Figure 5.5: Frequency dependence of χ' and χ'' at (a and b) 25 mT and (d and e) 40 mT for $B \parallel \langle 100 \rangle$. Panels (c) and (f) show χ'' plotted versus χ' for 25 and 40 mT respectively. The solid lines represent fits of the Cole-Cole formalism to the data.

Table 5.1: Parameters of the power law fits to the temperature dependence of M_{sat} and B_{C2} below T_C = 58.2 K for $B \parallel \langle 100 \rangle$ and $B \parallel \langle 110 \rangle$. For the sake of comparison the corresponding parameters from the literature are also provided.

		$M_{sat}(0)$	$B_{C2}(0)$	$T_C^0 - T_C$	β	n
fit of $M_{sat}(T)$	$B \parallel \langle 100 \rangle$	0.54±0.01	–	1.5±0.1	0.368±0.005	1.99±0.02
	$B \parallel \langle 110 \rangle$	0.53±0.01	–	1.8±0.3	0.391±0.002	2.01±0.01
	Ref[10]	0.559±0.007	–	1.8±0.1	0.393±0.004	1.95
fit of B_{C2}	$B \parallel \langle 100 \rangle$	–	50±1	0.3±0.1	0.34±0.02	5.1±0.2
	$B \parallel \langle 110 \rangle$	–	67±1	0.4±0.1	0.30±0.01	2.2±0.2
	Ref[10]	–	41	0	0.25	1

5.6. MAGNETIC PHASE DIAGRAMS BELOW 50 K

The results presented in the previous sections reveal new features and qualitatively different phase diagrams for $B \parallel \langle 100 \rangle$ and $\langle 110 \rangle$, as illustrated by the contour plots of the ZFC χ' and χ'' at $f = 10$ Hz shown in Fig. 5.6. These include additional data close to T_C from *Chapter* 3 [5]. Figure 5.7 shows the same data after the correction of the demagnetisation field. The phase boundaries are determined following the same criteria as in *Chapter* 3 [5]: B_{C1}, B_{A1} and B_{A2} from the peaks of χ'', and B_{C2} from the inflection points of χ' vs B. The discussion in the following is based on the results after the correction of the demagnetisation field.

Close to T_C, the transition from the helical to the conical phase is marked by a single B_{C1} line, which below ~ 50 K splits to two for $B \parallel \langle 100 \rangle$, reflecting the two adjacent peaks of χ''. On the other hand, for $B \parallel \langle 110 \rangle$ χ'' leads to two discontinuous B_{C1} lines, which coexist only at a limited temperature range, between ~ 40 and ~ 30 K, as seen in Fig. 5.3(d).

At high magnetic fields, a single B_{C2} line is found, which is similar for both orientations close to T_C. Differences appear below ~ 50 K, where B_{C2} levels off with decreasing temperature for $B \parallel \langle 100 \rangle$, while it keeps increasing for $B \parallel \langle 110 \rangle$. The temperature dependence of the two B_{C2} lines can be accounted for by Eq. 5.1 and the parameters are given in Table 5.1 with $\beta \approx 0.32$ and $T_C^0 \approx 58.6$ K~ T_C + 0.4 K for both orientations, $n = 5.1 \pm 0.2$ for $B \parallel \langle 100 \rangle$ and $n = 2.2 \pm 0.2$ for $B \parallel \langle 110 \rangle$. These values are different from those reported in the literature [14] and from those deduced from the temperature dependence of M_{sat}. Close to T_C, both B_{C2} lines reduce to the same simple power law, for $n = 1$, that has been previously reported for the same sample in *Chapter* 3 [5].

As already mentioned, the most remarkable difference between the two sample orientations appears close to B_{C2} and below ~ 30 K. In this field and temperature range, clear maxima are seen in both χ' and χ'' for $B \parallel \langle 100 \rangle$. This behaviour seems to be unique to Cu_2OSeO_3.

Figure 5.6: Contour plots of χ' and χ'' displayed versus temperature and magnetic field at $f = 10$ Hz from ZFC measurements for $B \parallel \langle 100 \rangle$ in panel (a) and (b), and $B \parallel \langle 110 \rangle$ in panel (c) and (d). The phase boundaries between the helical, conical, A- and field-polarised phases, B_{C1}, B_{A1}, B_{A2} and B_{C2} are shown as well. Below ~ 50 K two B_{C1} lines are illustrated by the circles and squares at lower fields. The units for χ' and χ'' are 10^{-4} and $10^{-6}\mathrm{m}^3/\mathrm{mol}_{\mathrm{Cu}}$ respectively.

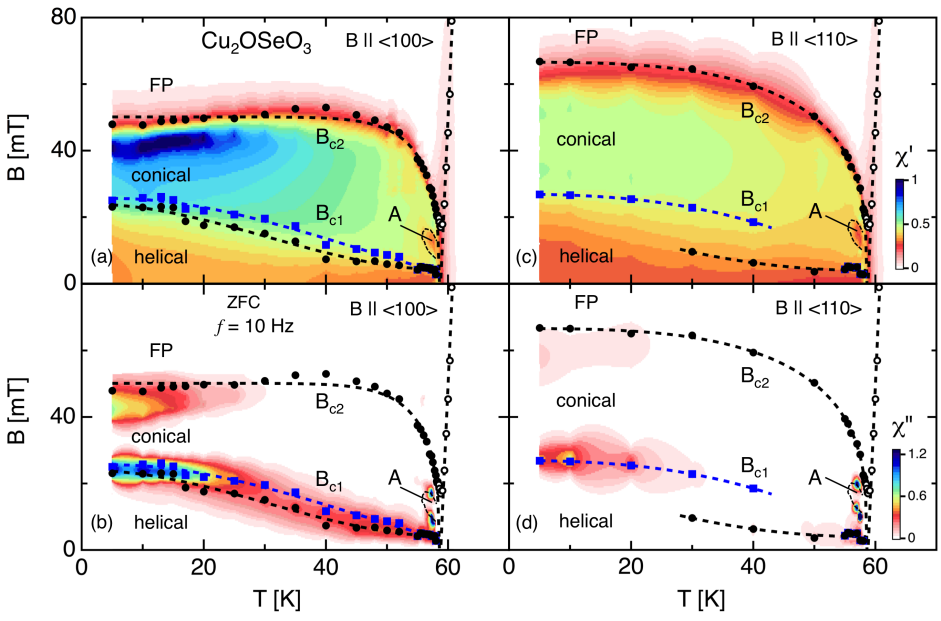

Figure 5.7: The contour plots of Fig. 5.6 after the correction of the demagnetisation field for $B \parallel \langle 100 \rangle$ in panel (a) and (b), and $B \parallel \langle 110 \rangle$ in panel (c) and (d).

5.7. NEUTRON SCATTERING

Complementary information is provided by small angle neutron scattering and the resulting patterns for $\vec{B} \parallel \langle 100 \rangle$ and $\langle 110 \rangle$ at $T = 6$ K are shown in Fig. 5.8(a-d) for $\vec{B} \perp \vec{k}_i$ and $\vec{B} \parallel \vec{k}_i$ realised by rotating both the sample and the magnetic field over 90° with respect to the neutron beam and thus to $\vec{k}_i$. At the helical phase, i.e. at low magnetic fields and $B = 10$ mT, the Bragg peaks appear along all three equivalent $\langle 100 \rangle$ crystallographic directions, and the scattering patterns show either four peaks along the diagonal axes for $\vec{k}_i \parallel \langle 100 \rangle$ or two peaks along the horizontal axis for $\vec{k}_i \parallel \langle 110 \rangle$, as discussed in *Chapter* 4.

By increasing the magnetic field to $B = 25$ mT, the helices are reoriented towards the magnetic field and the scattered intensity vanishes for $\vec{B} \parallel \vec{k}_i$, but appears along the magnetic field direction for $\vec{B} \perp \vec{k}_i$, as expected for the conical phase. For $\vec{B} \parallel \langle 100 \rangle$ and $\vec{B} \perp \vec{k}_i$ it is not possible to distinguish between the helical and conical peaks, as the scattering pattern does not change. On the other hand for $\vec{B} \parallel \langle 110 \rangle$ and $\vec{B} \perp \vec{k}_i$, the peaks of the conical phase appear at a different position on the detector than the helical peaks and coexist with them. Furthermore, the helical peaks drift away by 5° from the $\langle 100 \rangle$ directions and move towards the magnetic field direction. The weak additional peaks are most probably due to multiple scattering.

At $B = 30$ mT, if the magnetic field is applied along $\langle 100 \rangle$, the conical Bragg peaks for $\vec{B} \perp \vec{k}_i$ broaden along a circle with radius τ shown by the red dashed line, whereas weak diffuse scattering appears inside this circle for $\vec{B} \parallel \vec{k}_i$. When the magnetic field is applied along $\langle 110 \rangle$, the scattering patterns are similar to those for $B = 25$ mT but the intensity of the helical peaks is weaker.

By further increasing the magnetic field to $B = 35$ mT, the conical scattering for $\vec{B} \parallel \langle 100 \rangle$ and $\vec{B} \perp \vec{k}_i$ further broadens along the circle and develops to well defined peaks at $\sim \pm 30°$ with respect to the direction of the magnetic field. Furthermore, additional spots appear perpendicular to the magnetic field, in the vertical direction. In the complementary configuration for $\vec{B} \parallel \langle 100 \rangle$ and $\vec{B} \parallel \vec{k}_i$ it is clear that these additional spots arise from a ring of diffuse scattering that develops inside the circle with radius τ. When the magnetic field is applied along $\langle 110 \rangle$, the scattering patterns are as expected for the conical phase, with the conical Bragg peaks along the direction of the magnetic field for $\vec{B} \perp \vec{k}_i$ and no scattered intensity for $\vec{B} \parallel \vec{k}_i$. The broadening or diffuse scattering seen for $\vec{B} \parallel \langle 100 \rangle$ is thus absent for $\vec{B} \parallel \langle 110 \rangle$.

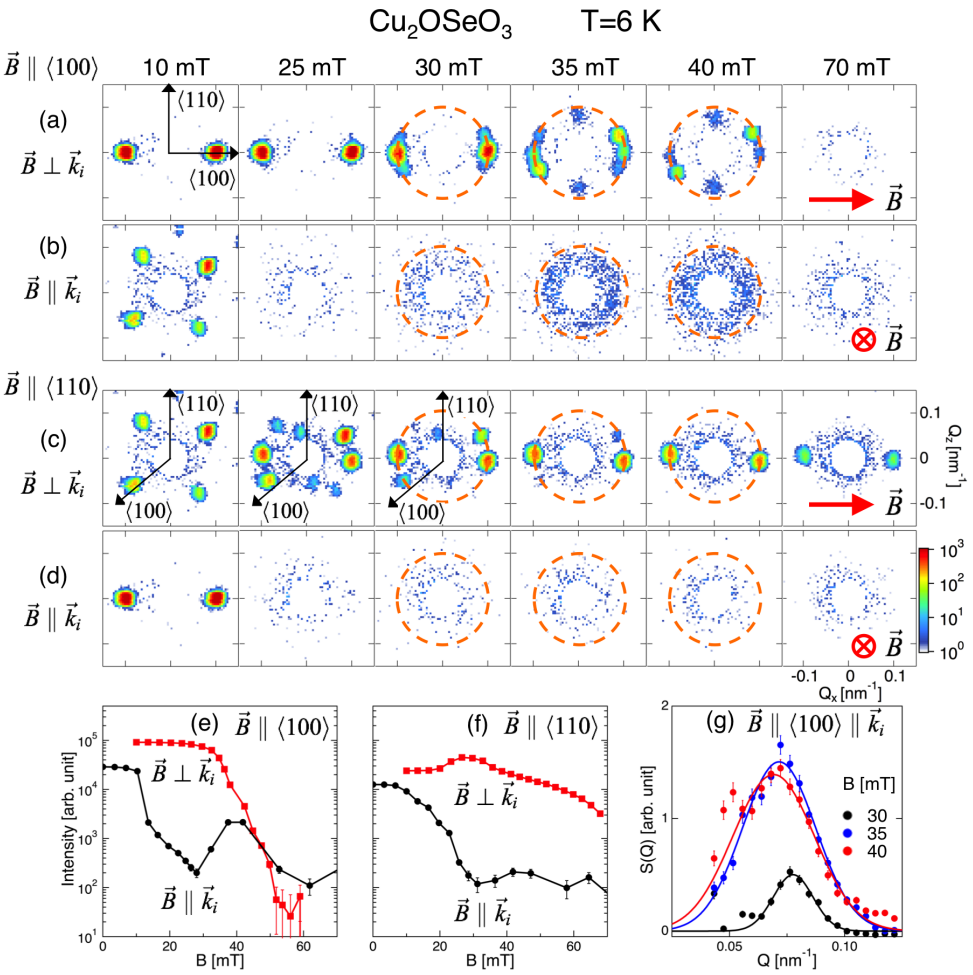

Figure 5.8: Panels (a-d): Neutron scattering patterns of Cu_2OSeO_3 at $T = 6$ K for various magnetic fields. The magnetic field $\vec{B}$ is along ⟨100⟩ (a and b) or ⟨110⟩ (c and d). For both field orientations the magnetic field was applied along and perpendicular to the neutron beam propagation vector $\vec{k}_i$. The dashed circles have a radius corresponding to the helix propagation vector $|\vec{\tau}| = 2\pi/\ell \sim 0.1$ nm^{-1}. Panels (e) and (f) show the scattered intensity integrated over the detector for $\vec{B} \parallel \langle 100 \rangle$ and ⟨110⟩, respectively. Panel (g) displays $S(Q)$ of the ring of diffuse scattering seen for $B = 30$, 35 and 40 mT in panel (b).

At $B = 40$ mT, the scattering patterns are similar to those at $B = 35$ mT, and the intensity of the conical peaks weakens. Finally at 70 mT, the scattered intensity vanishes for $\vec{B} \parallel \langle 100 \rangle$, whereas the conical phase persists for $\vec{B} \parallel \langle 110 \rangle$.

Figure 5.8 (e)-(g) give a quantitative analysis of the SANS results as a function of the magnetic field. Figure 5.8(e) and (f) show the magnetic field dependence

of the scattered intensity integrated over the detector for $\vec{B} \parallel \langle 100 \rangle$ and $\langle 110 \rangle$, respectively. For $\vec{B} \parallel \langle 100 \rangle$, the scattered intensity decreases continuously with increasing magnetic field for $\vec{B} \perp \vec{k}_i$ whereas for $\vec{B} \parallel \vec{k}_i$ it first drops significantly, marking the conical phase, shows a minimum at ~ 25 mT, and then a broad maximum at ~ 40 mT resulting from the ring of diffuse scattering.

For $\vec{B} \parallel \langle 110 \rangle$, the scattered intensity depends weakly on the magnetic field for $\vec{B} \perp \vec{k}_i$, with a weak maximum at ~ 25 mT resulting from the reorientation of the helices along the field direction in the conical phase. Above ~ 25 mT the intensity gradually decreases with increasing magnetic field. For $\vec{B} \parallel \vec{k}_i$ the intensity decreases continuously with increasing magnetic field up to ~ 25 mT, above which it practically vanishes.

Figure 5.8(g) shows $S(Q)$ deduced by azimuthal average of the diffuse scattering ring. For $\vec{B} \parallel \langle 100 \rangle$ and $\vec{B} \parallel \vec{k}_i$, $S(Q)$ can be fitted by a Gaussian function centred at 0.0776(3), 0.0715(3) and 0.0692(3) nm^{-1}, for 30, 35 and 40 mT respectively. The scattering thus moves towards lower values of Q with increasing magnetic field and reflects modulations $\sim 30\%$ longer than the helix pitch $\ell \sim 65$ nm.

The thermal evolution of the scattering for $\vec{B} \parallel \langle 100 \rangle$ is illustrated by Fig. 5.9 for $B = 40$ mT and $\vec{B} \perp \vec{k}_i$. At 52 K, only two well defined Bragg peaks are seen along the magnetic field direction as expected for the conical phase. By decreasing the temperature to 30 K, the peaks broaden along the circle with radius τ. At 22 K the peaks almost split, and this splitting is more visible at 15 K and 6 K. At these temperatures, additional spots appear in the vertical direction, perpendicular to the magnetic field direction, a signature of the diffuse scattering ring that shows up for $\vec{B} \parallel \vec{k}_i$.

A quantitative analysis of the broadening and splitting of the conical peaks has been performed by considering the angular dependence of $S(Q = \tau)$ shown in Fig. 5.9(b) for $T = 22$ K, which can be fitted by a superposition of two Gaussians, labelled as peak 1 and 2 in the figure, separated by $\Delta\phi$. The temperature dependence of $\Delta\phi$ is given in Fig. 5.9(c), showing a monotonic increase with decreasing temperature, from zero at $T = 52$ K to $\sim 30°$ for $T = 6$ K. The integrated intensities of the two Gaussians are given in Fig. 5.9(d). For both peaks the intensity increases with decreasing temperature from 52 K to 30 K. At lower temperatures, the intensity of peak 1, that is along the magnetic field, decreases significantly whereas the intensity of peak 2 levels off.

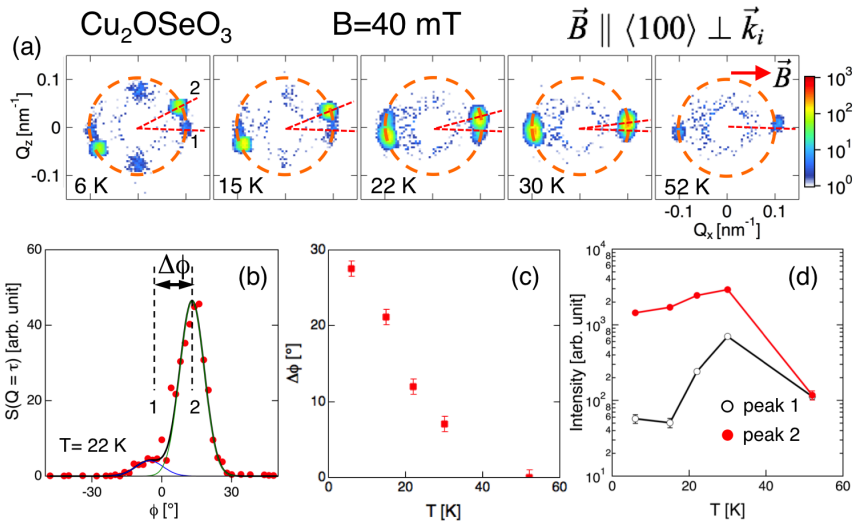

Figure 5.9: Neutron scattering patterns (a) and the corresponding data analysis (b-c) of Cu_2OSeO_3 at $B = 40$ mT for $\vec{B} \parallel \langle 100 \rangle \perp \vec{k}_i$. The dashed circles have a radius corresponding to the helix propagation vector $|\vec{\tau}| = 2\pi/\ell \sim 0.1\ nm^{-1}$. Panel (b) shows the angular dependence of the scattered intensity at $Q = \tau$ for $T = 22$ K, and the solid lines are a fit by a weighted superposition of two Gaussian functions. Below 52 K the conical Bragg peak splits in two denoted 1 and 2 in the pattern for 6 K. The angular distance between the peak positions is denoted by $\Delta\phi$, the temperature dependence of which is given in (c). Panel (d) shows the temperature dependence of the scattered intensities integrated over the Bragg peaks 1 and 2.

5

5.8. DISCUSSION

The magnetization, AC susceptibility and neutron scattering results presented above highlight the dependence of the magnetic phase diagram on the magnetic field directions and reveal the effect of anisotropy that has been predicted by theory [1, 15] but has not been observed in B20 magnets so far. Due to anisotropy, the magnetic moments at zero field rotate in the (100) plane. On the application of an external magnetic field, the magnetic moments cant towards the magnetic field forming a cone and thus deviate from the "easy" plane. With increasing magnetic fields, the cone closes continuously when a magnetic field is applied outside the easy axis of the helix, i.e. $B \parallel \langle 110 \rangle$. On the other hand for $B \parallel \langle 100 \rangle$, i.e. when the magnetic field is applied along the easy axis of the helix, thus perpendicular to the "easy" plane of the magnetic moments, the anisotropy distorts the cone leading to a metastable magnetic texture, which would flip by a first-order transition to the field-polarised state at B_{C2} [15].

Indeed, while a continuous second order transition is expected close to B_{C2}

for $B \parallel \langle 110 \rangle$, a discontinuous first order transition is predicted for $B \parallel \langle 100 \rangle$. This first order transition should appear as a jump of the magnetisation at $T = 0$ K, leading to a divergence of the derivative, thus of the susceptibility. This is consistent with our experimental results and the literature [9, 10], which however show less sharp change than theory. Furthermore, according to theory the jump of the magnetisation at B_{C2} should be visible up to ~ 50 K, while in our measurements the maxima in χ' and $\Delta M/\Delta B$ set in only below 20 K.

5.9. CONCLUSION

The DC magnetization, AC susceptibility and neutron scattering studies of Cu_2OSeO_3 reveal qualitatively different phase diagrams below 50 K depending on whether the magnetic field was applied along the easy $\langle 100 \rangle$ or the hard $\langle 110 \rangle$ crystallographic directions of the sample. The differences are not only in the specific values of the critical fields B_{C1} and B_{C2} but also in the behaviour of the magnetisation and susceptibility as well as of the neutron scattering patterns.

The B_{C1} transition from the helical to the conical phase splits in two well distinct lines below ~ 50 K. These two B_{C1} lines coexist only between 30 and 40 K for $B \parallel \langle 110 \rangle$, but expand almost over the whole temperature range for $B \parallel \langle 100 \rangle$.

Close to B_{C2}, the magnetisation and the susceptibility are in qualitative agreement with theory, which however foresees more dramatic effects with a discontinuous first order transition from the conical to the field polarised state when the magnetic field is applied along the easy axis and a continuous second order transition otherwise. These phenomena should be attributed to the cubic anisotropy, which may also be at the origin of the distorted conical spin textures and exotic scattering patterns observed for $B \parallel \langle 100 \rangle$ by neutron scattering.

At both B_{C1} and B_{C2} the frequency dependence of χ'' reflects the existence of very broad distributions of relaxation times and the superposition of several relaxation processes.

REFERENCES

[1] O. Janson, I. Rousochatzakis, A. A. Tsirlin, M. Belesi, A. A. Leonov, U. K. Roessler, J. van den Brink, and H. Rosner, *The quantum nature of skyrmions and half-skyrmions in Cu_2OSeO_3*, Nat Comms **5** (2014).

[2] J. Romhányi, J. van den Brink, and I. Rousochatzakis, *Entangled tetrahedron ground state and excitations of the magnetoelectric skyrmion material Cu_2OSeO_3*, Phys. Rev. B **90**, 140404 (2014).

[3] A. Aqeel, J. Baas, G. R. Blake, and T. T. M. Palstra, *Growth and helicity of non-centrosymmetric Cu_2OSeO_3 crystals*, unpublished (2017).

[4] K. H. Miller, X. S. Xu, H. Berger, E. S. Knowles, D. J. Arenas, M. W. Meisel, and D. B. Tanner, *Magnetodielectric coupling of infrared phonons in single-crystal Cu_2OSeO_3*, Phys. Rev. B **82**, 144107 (2010).

[5] F. Qian, H. Wilhelm, A. Aqeel, T. Palstra, A. Lefering, E. Brück, and C. Pappas, *Phase diagram and magnetic relaxation phenomena in Cu_2OSeO_3*, Phys. Rev. B **94**, 064418 (2016).

[6] J.-W. G. Bos, C. V. Colin, and T. T. M. Palstra, *Magnetoelectric coupling in the cubic ferrimagnet Cu_2OSeO_3*, Phys. Rev. B **78**, 094416 (2008).

[7] C. L. Huang, K. F. Tseng, C. C. Chou, S. Mukherjee, J. L. Her, Y. H. Matsuda, K. Kindo, H. Berger, and H. D. Yang, *Observation of a second metastable spin-ordered state in ferrimagnet Cu_2OSeO_3*, Phys. Rev. B **83**, 052402 (2011).

[8] T. Adams, A. Chacon, M. Wagner, A. Bauer, G. Brandl, B. Pedersen, H. Berger, P. Lemmens, and C. Pfleiderer, *Long-Wavelength Helimagnetic Order and Skyrmion Lattice Phase in Cu_2OSeO_3*, Phys. Rev. Lett. **108**, 237204 (2012).

[9] M. Belesi, I. Rousochatzakis, M. Abid, U. K. Rößler, H. Berger, and J. P. Ansermet, *Magnetoelectric effects in single crystals of the cubic ferrimagnetic helimagnet Cu_2OSeO_3*, Phys. Rev. B **85**, 224413 (2012).

[10] I. Živković, D. Pajić, T. Ivek, and H. Berger, *Two-step transition in a magnetoelectric ferrimagnet Cu_2OSeO_3*, Phys. Rev. B **85**, 224402 (2012).

[11] K. S. Cole and R. H. Cole, *Dispersion and Absorption in Dielectrics I. Alternating Current Characteristics*, J. Chem. Phys. **9**, 341 (1941).

[12] D. Huser, A. J. van Duyneveldt, G. J. Nieuwenhuys, and J. A. Mydosh, *Phenomenological model for the frequency dependence of the susceptibility of spin glasses and related compounds*, J. Phys. C: Solid State Phys. **19**, 3697 (1986).

[13] L. J. Bannenberg, A. J. E. Lefering, K Kakurai, Y. Onose, Y. Endoh, Y Tokura, and C. Pappas, *Magnetic relaxation phenomena in the Chiral Magnet $Fe_{1-x}Co_xSi$: an AC susceptibility study*, Phys. Rev. B **94**, 134433 (2016).

[14] I. Levatić, P. Popčević, V. Šurija, and A. Kruchkov, *Dramatic pressure-driven enhancement of bulk skyrmion stability*, Sci. Rep. **6**, 21347 (2016).

[15] A. Leonov, *Twisted, localized, and modulated states described in the phenomenological theory of chiral and nanoscale ferromagnets*, Ph.D. thesis (2011).

6

AC SUSCEPTIBILITY AND DISSIPATION PHENOMENA IN MNSI

We present comprehensive AC magnetic susceptibility measurements on the archetype helimagnet MnSi covering a frequency range from 0.5 *to* 1000 *Hz. The results lead to a magnetic phase diagram with the helical, conical, skyrmion lattice and field-polarised phases below* $T_C = 29.2$ *K. Above* T_C *dissipation phenomena have been found under magnetic fields and at low frequencies. These span a wide temperature and field range outside the ordered phase of MnSi and are bounded by the* B_{C2} *line.*

6.1. INTRODUCTION

MnSi is the archetype helimagnet and its chiral properties result from the lack of inversion symmetry in the crystal structure. The magnetic interactions, with the strongest ferromagnetic exchange, the weaker Dzyaloshisky-Moriya (DM) and the weakest anisotropy [1], lead to a helical magnetic ground state with a pitch of $\ell \sim 18$ nm propagating along $\langle 111 \rangle$ [2].

The helimagnetic transition at $T_C \sim 29$ K is of weakly first order, as seen by a sharp peak of the specific heat [3] and the sharp increase of the helical Bragg peaks observed by neutron scattering [4, 5]. The first-order transition is preceded by strong fluctuating correlations that are chiral and appear by neutron scattering as an intense ring of diffuse scattering with radius $\tau = 2\pi/\ell$ [4–8]. Magnetic fields suppress these fluctuating correlations and it is a subject of debate whether they also induce a tricritical point between a first and second order transition lines [9, 10].

The magnetic phase diagram of MnSi has been investigated by several experimental methods [2, 9, 11, 12], revealing the helical, conical, skyrmion lattice and field-polarised phases. Theory on the other side predicts a richer phase diagram with isolated skyrmions in the field-polarised state [13, 14], which have been observed in thin films [15], but not in bulk samples yet.

In the current study the magnetic phase diagram of MnSi has been investigated by AC magnetic susceptibility covering a frequency range of almost four orders of magnitude from 0.5 Hz to 1000 Hz. The results below T_C are in agreement with the literature [12, 16, 17]. Above T_C and at low frequencies dissipation phenomena have been found under magnetic fields, which have not been reported so far. The low characteristic frequencies involved reflect slow relaxation processes, possibly due to ferromagnetic fluctuations.

6.2. EXPERIMENTAL DETAILS

The measurements were performed on a cubic single crystal MnSi grown from a stoichiometric melt [18] and oriented with the $\langle 110 \rangle$ crystallographic direction vertical. The real and imaginary components of the AC susceptibility, χ' and χ'' respectively, were measured with a Quantum Design MPMS-5XL SQUID using the extraction method. The DC and the drive AC magnetic fields were applied along the vertical direction, thus $B \parallel \langle 110 \rangle$. The frequency of the AC field B_{ac} ranged from 0.5 to 1000 Hz. After having checked that the susceptibility above T_C is independent of the amplitude of B_{ac}, $B_{ac} = 0.4$ mT was used for all measurements.

The signals were recorded following two protocols: (i) T scans: the sample was brought to 50 K, where a magnetic field was applied and the susceptibility was measured by decreasing stepwise the temperature. (ii) B scans: the sample was first brought to 50 K and then to the measuring T at zero field. The susceptibility was measured by increasing stepwise the magnetic field. All measurements were performed once the sample reached thermal equilibrium.

6.3. RESULTS

Figure 6.1 shows the temperature dependence of χ' (a and b) and χ'' (c and d) for selected magnetic fields at a frequency of 5 Hz. At zero field, χ' increases with decreasing temperature and a cusp at $T_C = 29.2$ K marks the transition to the helical state. Under an external magnetic field, this cusp becomes less pronounced and eventually reduces to a kink at $B \sim 0.08$ T. With increasing magnetic fields, two sharp maxima develop just below T_C for $B = 0.12$ T and 0.2 T. These mark the lower and upper field boundaries of the A-phase, which appears as a minimum in χ' at the intermediate field of $B = 0.16$ T. By further increasing the magnetic field, a kink reappears at T_C for $B = 0.24$ T, where the shape of χ' becomes similar to that at $B = 0.08$ T. Above $B = 0.3$ T, the kink shifts to lower temperatures with increasing magnetic fields, marking the transition line B_{C2} that separates the conical from the field polarised state. In addition, a broad maximum develops above T_C, which is centred at $T_1 \sim 31$ K for $B = 0.3$ T and shifts to higher temperatures with increasing magnetic field. At 2 T, T_1 is higher than 40 K.

Complementary information is provided by the χ'' curves in Figs. 6.1(c) and (d). At zero field χ'' is zero over the whole temperature range. At $B = 0.04$ T a broad χ'' signal appears below T_C. This signal vanishes for $B > 0.08$ T and thus it should be related to B_{C1} and the transition from the helical to the conical phase. The borders of the A-phase are identified by sharp χ'' peaks, as shown in Fig. 6.1(c) for fields between 0.12 and 0.2 T.

These results are in agreement with previous reports [12, 16, 17]. A new feature revealed by our low frequency measurements is the broad χ'' signal that appears above T_C and for $B \gtrsim 0.08$ T. The amplitude of this signal increases with increasing magnetic field and reaches a maximum at $B \sim 0.4$ T. By further increasing the magnetic field, this signal decreases and eventually dies out for $B > 2$ T. This χ'' signal is centred at $T_2 \sim 31$ K for $B < 0.4$ T and shifts to higher temperatures for larger magnetic fields. At 2 T it is centred at $T_2 \sim 35$ K, i.e. $\sim T_C + 6$ K.

This χ'' signal appears only at low frequencies, for $f \lesssim 20$ Hz, and its frequency dependence for $T = 31$ K and selected magnetic fields given in Fig. 6.2(a) shows that the associated characteristic frequency is below 0.5 Hz. On the other hand, this frequency dependence is hardly seen on χ', shown in the inset of

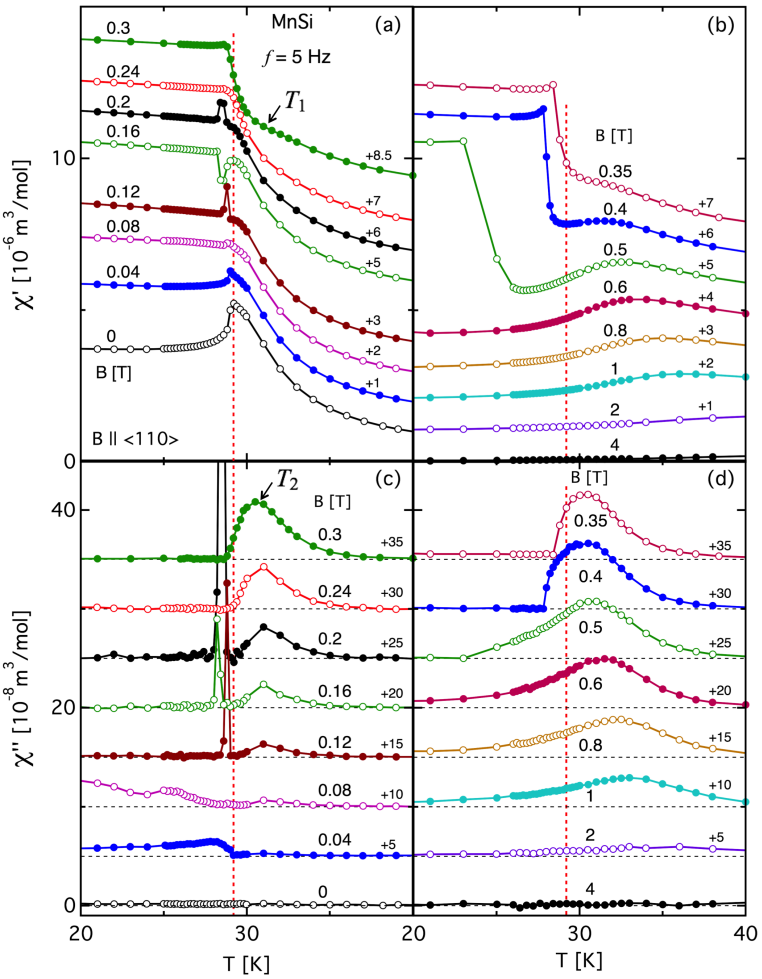

Figure 6.1: Temperature dependence of the magnetic susceptibility χ', panels (a) and (b), and χ'', panels (c) and (d) at $f = 5$ Hz for various magnetic fields with $B \parallel \langle 110 \rangle$ in MnSi. The vertical lines indicate $T_C = 29.2$ K at zero field. For the sake of clarity, all curves have been shifted vertically with respect to the base lines as indicated.

Fig. 6.2(a). Figure 6.2(b) shows complementary measurements of χ' and χ'' as a function of magnetic field for selected frequencies. χ' decreases continuously with increasing magnetic field and does not change with frequency. In contrast χ'' changes with frequency and shows a broad maximum at ~ 0.4 T for all frequencies.

The contour plots in Fig. 6.3 summarise the magnetic field and temperature dependence of χ' and χ'' at a frequency of $f = 5$ Hz. The light blue area at low magnetic fields in Fig. 6.3(a) stands for the helical phase, which is bounded by the B_{C1} transition line seen in χ''. The dark blue area in Fig. 6.3(a) corresponds to the conical phase, where no χ'' signal is found and is delimited by the B_{C2} transition line deduced from the kink of χ'. The A-phase is seen both in χ', as a light blue narrow window close to T_C, and in χ'' which clearly marks its boundaries.

Above T_C the contour plots are dominated by the broad maxima centred at T_1 for χ', and at T_2 for χ''. T_1 increases linearly with increasing magnetic fields, and T_2 shows an almost vertical line below ~ 0.4 T and then increases linearly at higher magnetic fields. Furthermore, the χ'' signal spans a wide field and temperature range and seems to be bounded by the B_{C2} line at the low temperature and magnetic field side.

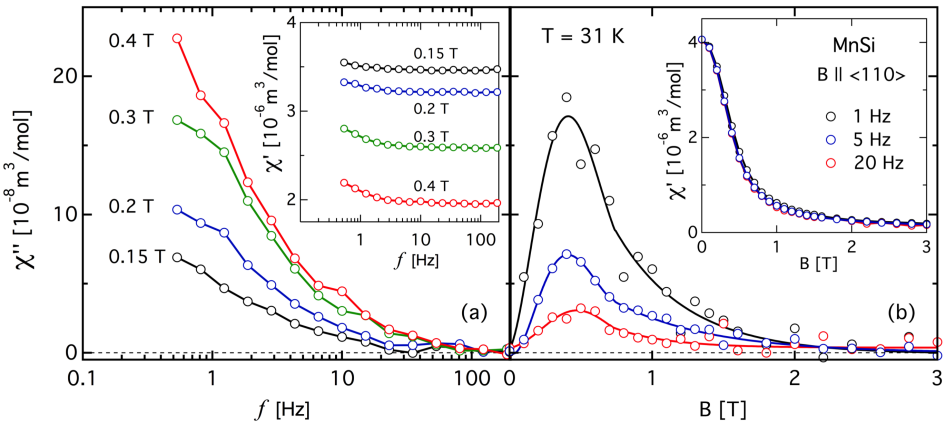

Figure 6.2: χ'' versus frequency (a) for selected magnetic fields and versus magnetic field (b) for $f = 1$, 5 and 20 Hz at $T = 31$ K. The insets in panels (a) and (b) show the frequency and magnetic field dependence of χ' respectively.

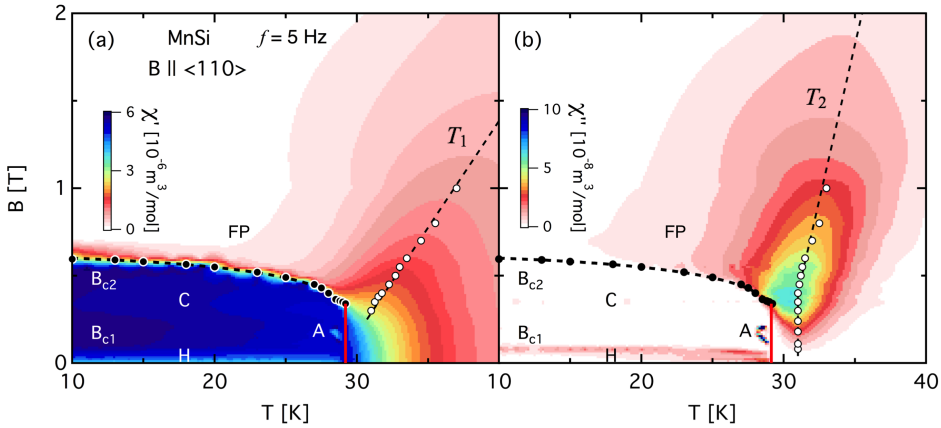

Figure 6.3: Contour plots of χ' (a) and χ'' (b) at $f = 5$ Hz for MnSi with $B \parallel \langle 110 \rangle$. The vertical red lines indicate $T_C = 29.2$ K. Below T_C, the symbols stand for the following phases : H for the helical, C for the conical, A for the A-phase and FP for the field-polarised state. The B_{C2} line that separates the conical phase from the field-polarised one is deduced from the kink of χ'. Above T_C, the position of the broad maxima in χ' and χ'' lead to T_1 and T_2 respectively.

6.4. DISCUSSION

The phase diagram measured by AC susceptibility is consistent with the literature and can be understood considering the stability region of the helical, conical, A- and field-polarised phases reported for MnSi [12, 16, 17] and other B20 chiral magnets [19–21]. The new feature revealed by this investigation is the strong χ'' signal that appears above T_C and at very low frequencies, lower than in previous studies [12, 16, 17] which were performed for $f \geqslant 10$ Hz, where the χ'' signal above T_C is very weak as illustrated by Fig. 6.2(a). We note that similar χ'' have been reported above T_C for Cu_2OSeO_3 [20] and $Fe_{0.7}Co_{0.3}Si$ [21]. However, in these systems, the χ'' signal is much weaker and appears at a lower frequency of 0.8 Hz for Cu_2OSeO_3 and 5 Hz for $Fe_{0.7}Co_{0.3}Si$. Thus, this χ'' above T_C seems to be universal for chiral magnetic systems, although the associated frequency range is different from one system to another.

The frequency dependence of χ'' above T_C indicates macroscopic characteristic times associated with slow relaxation dynamics. The fact that this χ'' signal is bounded by the B_{C2} line may be considered as an indication that it is incompatible with the conical order and thus is due to ferromagnetic fluctuating correlations. The non-monotonic change of χ'' with increasing magnetic field shown in Fig. 6.2(b) indicates that these correlations are enhanced for $B \lesssim 0.4$ T and then suppressed at higher magnetic fields up to ~ 2 T.

6.5. CONCLUSION

In conclusion, the AC susceptibility measurements lead to a magnetic phase diagram of MnSi, which below T_C is consistent with literature. Above T_C and at low frequencies a broad χ'' signal appears under magnetic fields, spanning a wide field and temperature range and is bounded by the B_{C2} line. The very low associated characteristic frequencies imply slow relaxation dynamics, the origin of which is unknown, but could reflect ferromagnetic fluctuating correlations.

REFERENCES

[1] P. Bak and M. H. Jensen, *Theory of helical magnetic structures and phase transitions in MnSi and FeGe,* J. Phys. C: Solid State Phys. **13**, L881 (1980).

[2] S. Mühlbauer, B. Binz, F. Jonietz, C. Pfleiderer, A. Rosch, A. Neubauer, R. Georgii, and P. Böni, *Skyrmion lattice in a chiral magnet,* Science **323**, 915 (2009).

[3] S. M. Stishov, A. E. Petrova, A. A. Shikov, T. A. Lograsso, E. I. Isaev, B. Johansson, and L. L. Daemen, *Lost Heat Capacity and Entropy in the Helical Magnet MnSi,* Phys. Rev. Lett. **105**, 236403 (2010).

[4] C. Pappas, E. Lelièvre-Berna, P. Bentley, P. Falus, P. Fouquet, and B. Farago, *Magnetic fluctuations and correlations in MnSi: Evidence for a chiral skyrmion spin liquid phase,* Phys. Rev. B **83**, 224405 (2011).

[5] M. Janoschek, M. Garst, A. Bauer, P. Krautscheid, R. Georgii, P. Böni, and C. Pfleiderer, *Fluctuation-induced first-order phase transition in Dzyaloshinskii-Moriya helimagnets,* Phys. Rev. B **87**, 134407 (2013).

[6] C. Pappas, E. Lelièvre-Berna, P. Falus, P. Bentley, E. Moskvin, S. Grigoriev, P. Fouquet, and B. Farago, *Chiral Paramagnetic Skyrmion-like Phase in MnSi,* Phys. Rev. Lett. **102**, 197202 (2009).

[7] S. Grigoriev, S. Maleyev, A. Okorokov, Y. Chetverikov, R. Georgii, P. Böni, D. Lamago, H. Eckerlebe, and K. Pranzas, *Critical fluctuations in MnSi near T_C: A polarized neutron scattering study,* Phys. Rev. B **72**, 134420 (2005).

[8] S. V. Grigoriev, S. V. Maleyev, E. V. Moskvin, V. A. Dyadkin, P. Fouquet, and H. Eckerlebe, *Crossover behavior of critical helix fluctuations in MnSi,* Phys. Rev. B **81**, 144413 (2010).

[9] A. Bauer, M. Garst, and C. Pfleiderer, *Specific heat of the skyrmion lattice phase and field-induced tricritical point in MnSi,* Phys. Rev. Lett. **110**, 177207 (2013).

[10] S. M. Stishov and A. E. Petrova, *Vollhardt invariant and phase transition in the helical itinerant magnet MnSi,* Phys. Rev. B **94**, 140406(R) (2016).

[11] T. Adams, S. Mühlbauer, C. Pfleiderer, F. Jonietz, A. Bauer, A. Neubauer, R. Georgii, P. Böni, U. Keiderling, K. Everschor, M. Garst, and A. Rosch, *Long-Range Crystalline Nature of the Skyrmion Lattice in MnSi,* Phys. Rev. Lett. **107**, 217206 (2011).

[12] A. Bauer and C. Pfleiderer, *Magnetic phase diagram of MnSi inferred from magnetization and ac susceptibility,* Phys. Rev. B **85**, 214418 (2012).

[13] M. N. Wilson, A. B. Butenko, A. N. Bogdanov, and T. L. Monchesky, *Chiral skyrmions in cubic helimagnet films: The role of uniaxial anisotropy,* Phys. Rev. B **89**, 094411 (2014).

[14] A. O. Leonov and M. Mostovoy, *Multiply periodic states and isolated skyrmions in an anisotropic frustrated magnet,* Nat Comms **6**, 8275 (2015).

[15] X. Z. Yu, Y. Onose, N. Kanazawa, J. H. Park, J. H. Han, Y. Matsui, N. Nagaosa, and Y. Tokura, *Real-space observation of a two-dimensional skyrmion crystal,* Nature **465**, 901 (2010).

[16] C. Thessieu, C. Pfleiderer, A. N. Stepanov, and J. Flouquet, *Field dependence of the magnetic quantum phase transition in MnSi,* J. Phys.: Condens. Matter **9**, 6677 (1997).

[17] A. Bauer, A. Neubauer, C. Franz, W. Münzer, and M. Garst, *Quantum phase transitions in single-crystal $Mn_{1-x}Fe_xSi$ and $Mn_{1-x}Co_xSi$: Crystal growth, magnetization, ac susceptibility, and specific heat,* Phys. Rev. B **82**, 064404 (2010).

[18] S. M. Stishov, A. E. Petrova, S. Khasanov, G. K. Panova, A. A. Shikov, J. C. Lashley, D. Wu, and T. A. Lograsso, *Magnetic phase transition in the itinerant helimagnet MnSi: Thermodynamic and transport properties,* Phys. Rev. B **76** (2007).

[19] H. Wilhelm, M. Baenitz, M. Schmidt, U. K. Rößler, A. A. Leonov, and A. N. Bogdanov, *Precursor Phenomena at the Magnetic Ordering of the Cubic Helimagnet FeGe,* Phys. Rev. Lett. **107**, 127203 (2011).

[20] F. Qian, H. Wilhelm, A. Aqeel, T. Palstra, A. Lefering, E. Brück, and C. Pappas, *Phase diagram and magnetic relaxation phenomena in Cu_2OSeO_3,* Phys. Rev. B **94**, 064418 (2016).

[21] L. J. Bannenberg, A. J. E. Lefering, K Kakurai, Y. Onose, Y. Endoh, Y Tokura, and C. Pappas, *Magnetic relaxation phenomena in the Chiral Magnet $Fe_{1-x}Co_xSi$: an AC susceptibility study,* Phys. Rev. B **94**, 134433 (2016).

7

NEUTRON SCATTERING INVESTIGATION OF MAGNETIC CORRELATIONS IN FEGE

This chapter presents a small angle neutron scattering and polarisation analysis investigation of the magnetic correlations in FeGe. At zero magnetic field, chiral magnetic short-range order appears above $T_C \sim 278$ K, where the transition to the helical phase seems to be of first order. On the application of magnetic fields, close to T_C and the skyrmion lattice phase, the neutron scattering patterns lead to a phase diagram that is in agreement with literature. A new feature is additional scattering that appears just above T_C as a precursor to the skyrmion lattice phase.

Below ~ 250 K, the helices at zero field reorient from the $\langle 100 \rangle$ crystallographic direction at high temperatures to $\langle 111 \rangle$ at low temperatures. The origin of this effect is discussed in conjunction with magnetoelastic coupling and possible structural changes.

7.1. INTRODUCTION

Cubic FeGe is a chiral helimagnet [1, 2] similar to MnSi but with $T_C \sim 278$ K that is slightly below room temperature and a helix pitch of $\ell \sim 70$ nm [1]. The helix propagation vector in FeGe is along the crystallographic ⟨100⟩ direction just below T_C and along the ⟨111⟩ axis at low temperatures [3], which contrasts to the typical single propagation vector found for other chiral helimagnets [4, 5].

The magnetic phase diagram of FeGe close to T_C has been investigated by magnetic susceptibility [6, 7] and neutron scattering [8], revealing the helical, conical, *A*- and field-polarised phases characteristic of chiral B20 magnets below T_C [4, 9] and precursor phenomena just above T_C [6, 7].

Comparatively to other B20 compounds, very few studies have been carried out for FeGe, in particular by neutron scattering [3, 8]. This is mainly due to the difficulty to grow large single crystals of cubic FeGe, as other polymorphs appear as impurity phases [10]. In the current study, two single crystals of FeGe with a volume of ~ 1 mm^3 have been investigated by small angle neutron scattering. In addition, polarisation analysis was used to determine the magnetic chirality. The resulting magnetic phase diagram with the helical, conical and skyrmion lattice phases is in agreement with previous studies [1, 6–8]. A new finding is an indication for specific precursor phenomena above the skyrmion lattice phase.

The temperature dependence of the SANS patterns at zero field reveal the reorientation of the helices from ⟨100⟩ to ⟨111⟩ below ~ 250 K and the results are discussed in conjunction with magnetoelastic coupling and possible structural changes.

7.2. EXPERIMENTAL DETAILS

Two identical single crystals of cubic FeGe have been prepared by chemical vapour transport method [10]. The quality of the samples was checked by x-ray diffraction and the Laue single crystal neutron diffractometer at the Institut Laue Langevin (ILL). Both samples had a nearly spherical shape and a volume of ~ 1 mm^3 with the ⟨111⟩ crystallographic direction along the vertical $\vec{z}$ axis, as illustrated by Fig. 7.1.

Small angle neutron scattering (SANS) in combination with polarization analysis and neutron spin echo (NSE) were performed at a high-resolution NSE spectrometer IN15 of ILL. The wavelength was $\lambda = 8$ Å at zero field and $\lambda = 9$ Å under magnetic fields with $\Delta\lambda/\lambda = 15\%$ and a polarisation of 95%. The measurements under magnetic fields were performed with a 7 T horizontal Cryomagnet, producing a magnetic field along the incoming neutron beam. The detector at IN15

had dimensions of 32×32 cm^2 with 1 cm^2 pixel resolution and was located at 4.6 m from the sample.

For all measurements, the background was determined above T_C, at 283 K, where the magnetic scattering was negligible. In order to compare data sets obtained from different sample environments, the results in the following will be plotted against $(T - T_C)$.

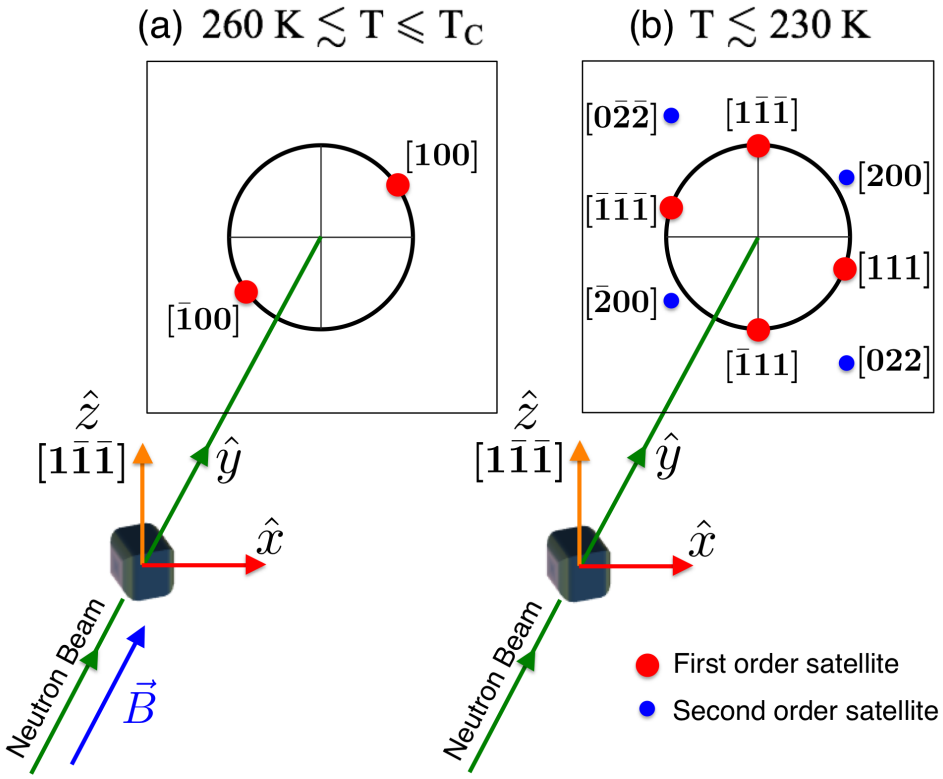

Figure 7.1: Schematic drawings of the SANS geometry. A polarised neutron beam was used and for the analysis of the scattering patterns a right-handed xyz Cartesian coordinate system was introduced as shown in the figure. The neutron beam propagates along the $\vec{y}$ axis and the neutrons scattered by the sample are detected by a position sensitive detector leading to the different scattering patterns of (a) and (b). The FeGe sample was mounted with the $\langle 111 \rangle$ axis vertical and along the $\vec{z}$ axis. Just below T_C, helimagnetic Bragg peaks appear at all equivalent $\langle 100 \rangle$ directions as illustrated in (a). Around 230 K, the helix propagation vector reorients towards the $\langle 111 \rangle$ directions. At low temperatures, the scattering pattern is more complex and includes high order Bragg peaks as given in (b). For the investigation of the magnetic field–temperature $(B - T)$ phase diagram close to T_C, a horizontal magnetic field was applied along $\vec{y}$ direction, as indicated in (a).

7.3. MAGNETIC BEHAVIOUR CLOSE TO T_C

The temperature dependence of the scattered intensity integrated over the ⟨100⟩ magnetic Bragg peak positions is given in Fig. 7.2 and the insets show typical scattering patterns just above and below T_C. Above $T_C \sim 278.4$ K, substantial scattered intensity has been observed at a ring with a radius of $Q = 0.09$ nm^{-1}, as illustrated by the scattering pattern at 279 K. Below T_C, magnetic Bragg peaks appear at the ⟨100⟩ positions, giving rise to the pattern at 260 K. The intensity of these Bragg peaks increases by decreasing the temperature and reaches a maximum at about 250 K. Between 250 K and T_C, the temperature dependence of the intensity follows the dotted red line, which corresponds to the power law: $I_{100} = A(1 - T/T_0)^{2\beta_1}$ with $\beta_1 = 0.414 \pm 0.007$ and $T_0 = 279.6 \pm 0.1$ K, i.e. ~ 1.2 K higher than T_C. These parameters are given in Table 7.1.

A close inspection of the scattered intensity in the vicinity of T_C is illustrated by Fig. 7.3. The data are the same as in Fig. 7.2 but the temperature scale is limited to the close vicinity of T_C. Above T_C, the scattered intensity is weak but the appearance of the helimagnetic Bragg peaks at T_C gives rise to a fast intensity increase, which is described by the blue line and the power law: $I_{100} = B(1 - T/T_C)^{2\beta_2}$ with $T_C = 278.4 \pm 0.1$ K and $\beta_2 = 0.153 \pm 0.003$.

As seen in Fig. 7.3, this power law deviates significantly from the red dashed line that corresponds to the fit between 250 K and T_C, and extrapolates to a lower transition temperature. A similar behaviour has been reported by Lebech [3], as shown in the inset of Fig. 7.3, which re-plots the data points of Ref. 3. These data have been fitted with the parameters given in Table 7.1, leading to the black line in the inset. The exponent close to T_C does not correspond to any universality class, which may indicate a first order transition at T_C. On the other hand, the exponent $\beta_1 = 0.414$ obtained from the fit between 250 K and T_C agrees with the one obtained from the magnetisation measurement [11] and is close to the value expected for a $3D$-Heisenberg magnet.

Table 7.1: Parameters of the power law fits to the temperature dependence of the scattered intensity integrated over the Bragg peaks along ⟨100⟩ at zero field. The fitting results of the data from the literature [3] and the magnetisation [11] are also provided.

method	β	T_0	T-range
Fig. 7.2	0.414(7)	$T_C + 1.2$ K	250 K$< T < T_C$
Fig. 7.3	0.153(3)	T_C	$\Delta T/T_C < 1\%$
Data from Lebech [3]	0.150(2)	T_C	$\Delta T/T_C < 1\%$
Magnetisation [11]	0.369(8)	T_C	$\Delta T/T_C < 1\%$

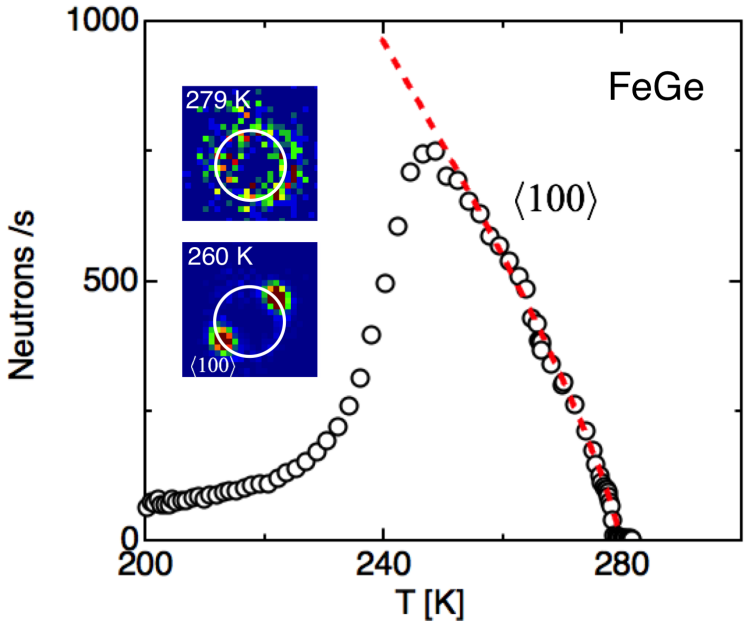

Figure 7.2: Temperature dependence of the scattered neutron intensity integrated over the ⟨100⟩ magnetic Bragg peak positions. The red dashed line is the fit to the data between 250 K and T_C. The insets show typical scattering patterns below and above T_C. The white circles in the scattering patterns have a radius of $Q = 0.09$ nm^{-1}.

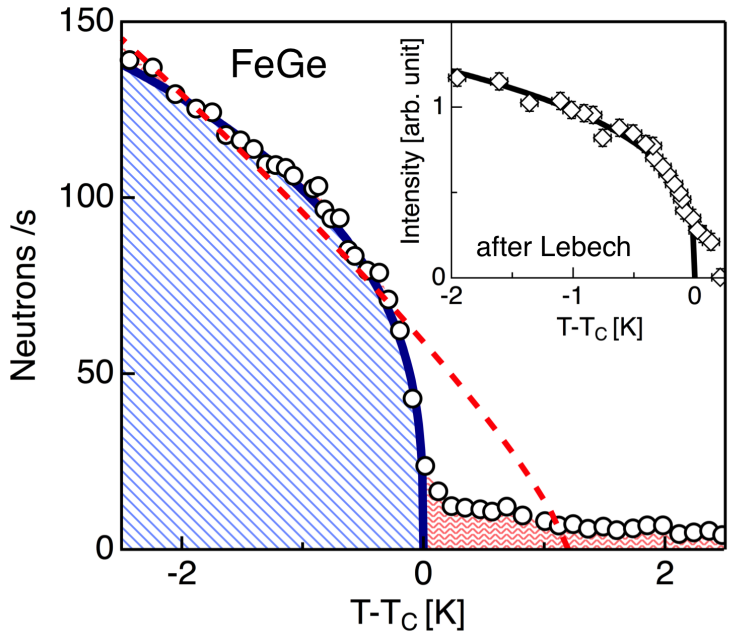

Figure 7.3: Temperature dependence of the scattered neutron intensity in the close vicinity of T_C. The data and the red dashed line are the same as in Fig. 7.2. The blue line is the fit to the data very close to T_C. The inset shows the data re-digitised from Lebech [3].

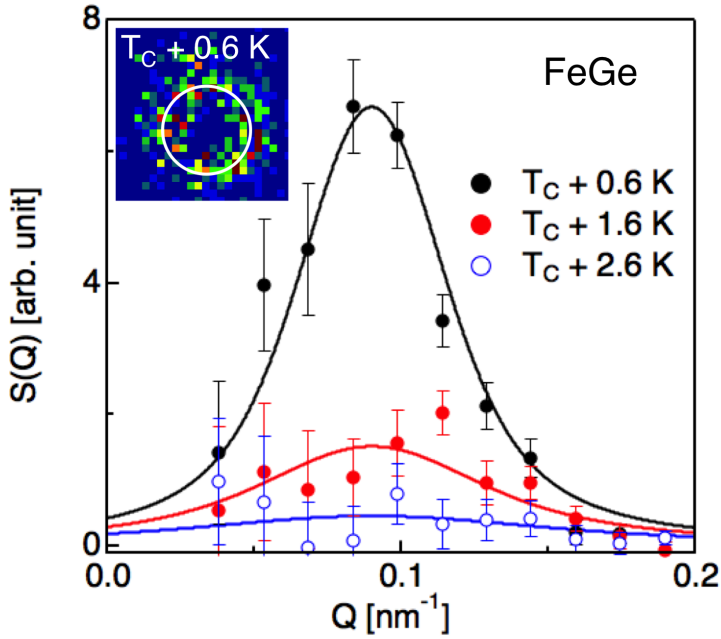

Figure 7.4: $S(Q)$ obtained from the diffuse scattering patterns at $T_C + 0.6$ K (circles), $T_C + 1.6$ K (squares) and $T_C + 2.6$ K (triangles) for FeGe. The inset shows a typical scattering pattern at $T_C +$ 0.6 K and the white circle has a radius of $Q = 0.09$ nm^{-1}.

Figure 7.4 shows azimuthal averages of the diffuse scattering patterns above T_C, leading to $S(Q)$. At $T_C + 0.6$ K and $T_C + 1.6$ K, the scattered intensity is higher and clear maxima are observed at $Q = 0.09$ nm^{-1}, and $S(Q)$ follows the Ornstein-Zernike function (eq. 4.1) convoluted with the Gaussian resolution. The fit leads to $\xi = 25 \pm 6$ nm and 53 ± 7 nm for $T_C + 1.6$ K and $T_C + 0.6$ K, respectively. Thus even at the closest vicinity of T_C the correlations are by $\sim 25\%$ shorter than the helix pitch $\ell \sim 70$ nm.

The chirality of the magnetic correlations was investigated with polarised neutron scattering following eq. 2.9. Figure 7.5 shows the scattering patterns of FeGe obtained with opposite incoming beam polarisations and the resulting temperature dependence of the magnetic chirality. Below T_C, the helical Bragg peaks along $\langle 100 \rangle$ are enhanced for $\vec{P} \parallel \vec{Q}$ and are extinct for $\vec{P} \parallel -\vec{Q}$. Above T_C, the scattering patterns show half-moon shapes at the right or left of the direct beam depending on the orientation (right or left) of the incoming beam polarisation, as shown in Fig. 7.5 (c) and (d). This behaviour is similar to that found in MnSi [12] and Cu_2OSeO_3 [13].

Below T_C, the polarisation matrix at $T_C-0.4$ K is that of an ideal right-handed single domain helix, shown in below:

$$\mathbb{P}_{T_C-0.4\text{ K}} = \begin{vmatrix} -1.003\pm0.002 & 0.951\pm0.008 & 0.991\pm0.007 \\ -0.066\pm0.008 & -0.021\pm0.011 & 0.069\pm0.009 \\ 0.078\pm0.007 & 0.088\pm0.011 & 0.096\pm0.009 \end{vmatrix}$$

Following eq. 2.13 full chirality has been found below T_C and up to $\sim T_C+0.1$ K, as shown in Fig. 7.5 (e). At higher temperatures, the poor signal to noise ratio due to the weak intensity and limited sample size prevents a reliable determination of η and leads to large error bars in Fig. 7.5.

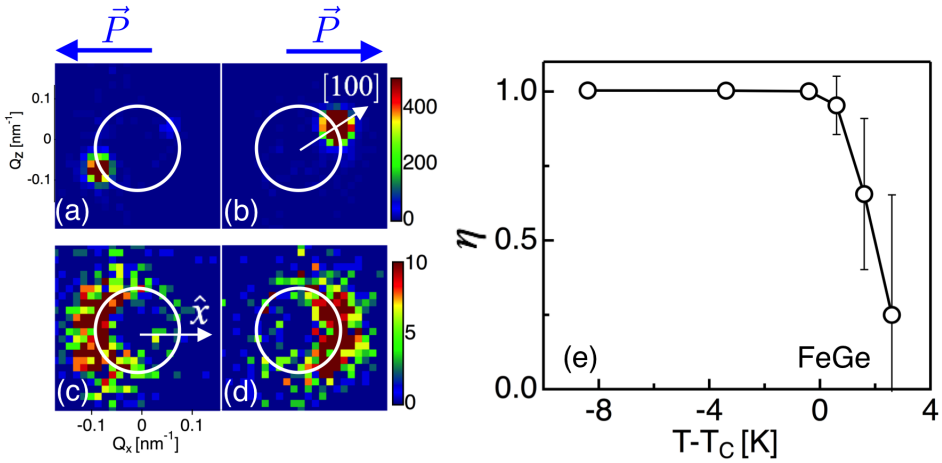

Figure 7.5: Scattering patterns of FeGe at $T_C-0.4$ K (a and b) and $T_C+0.6$ K (c and d) with opposite incoming beam polarisation. The resulting temperature dependence of the chiral fraction η at zero field and close to T_C is given in (e).

7.4. $B-T$ PHASE DIAGRAM

The magnetic behaviour under magnetic field was investigated close to T_C, where the A-phase appears by applying a magnetic field along the neutron propagation direction, as illustrated in Fig. 7.1(a).

The field evolution of the scattering patterns in the vicinity of T_C is depicted in Fig. 7.6. Below T_C, at 277.9 K, at low magnetic fields for $B=2$ mT, the helical peaks appear along $\langle 100\rangle$ at $Q=0.09$ nm^{-1}. A magnetic field at 5 mT is sufficient to dramatically suppress the helical peaks. At 12 mT, the scattering pattern is practically the background as expected for the conical phase. Further increasing the magnetic field to $B=15$ mT, a hexagonal scattering pattern sets in, showing

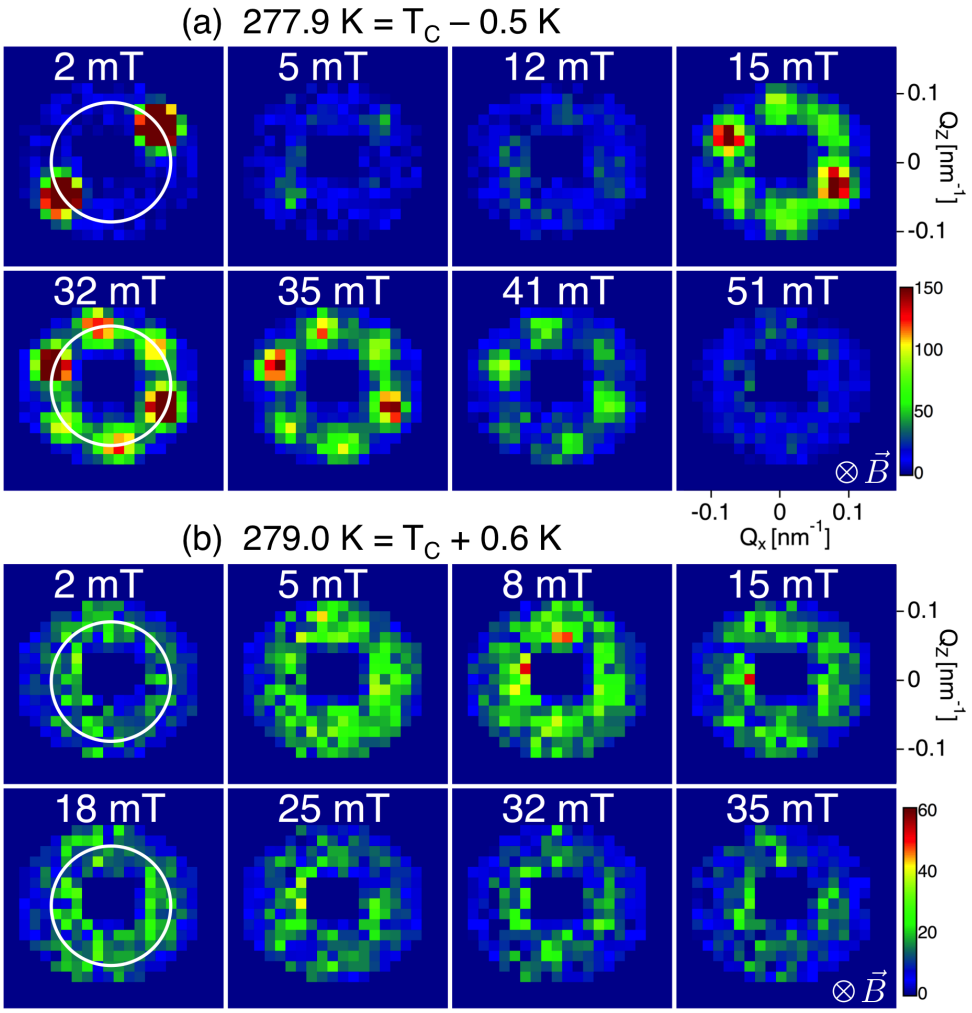

Figure 7.6: Evolution of the magnetic scattering patterns as a function of magnetic field for temperatures (a) below T_C at $T_C - 0.5$ K= 277.9 K and (b) above T_C at $T_C + 0.6$ K= 279.0 K after zero field cooling from 283 K. The white circles in the scattering patterns have a radius of $Q = 0.09$ nm^{-1}.

six-fold Bragg peaks perpendicular to the magnetic field direction, which is characteristic of the A-phase. Those peaks are located at $Q = 0.09$ nm^{-1}, as indicated by the ring, which is the same as the helical peaks. Such hexagonal scattering pattern becomes much weaker for $B = 41$ mT and finally vanishes above 51 mT, resulting to a similar scattering pattern at 12 mT.

Above T_C at 279 K (= $T_C + 0.6$ K), the pattern at low magnetic fields is weakly diffuse scattering with a maximum intensity centred at $Q = 0.09$ nm^{-1}. With in-

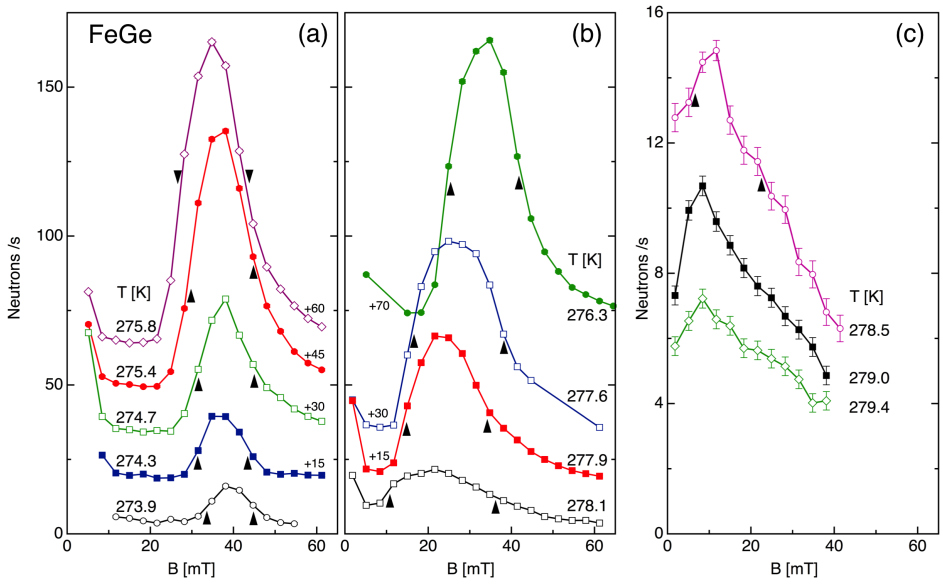

Figure 7.7: Field dependence of the magnetic intensity integrated over the whole detector with the magnetic field applied along the neutron propagation direction as illustrated by Fig. 7.1 (a). Each curve has been recorded after zero-field cooling from 283 K. The results below T_C are given in panels (a) and (b) whereas above T_C in panel (c). For the sake of clarity, the curves in (a) and (b) are vertically shifted with respect to the base line by the values indicated. In panel (c) such a shift was not required. The arrows in the figure indicate the inflection points of the field dependent intensity, used to determine the limits of the A-phase.

creasing magnetic fields, the brilliance of the diffuse pattern gets enhanced and reaches maximum at ~ 8 mT. Further increasing magnetic fields, the scattered pattern practically vanishes.

Figure 7.7 shows the resulting magnetic field dependence of the scattered intensity integrated over the detector for selected temperatures in the vicinity of T_C. Below T_C, even low magnetic fields lead to significant suppression of the recorded scattered intensity, indicating the onset of the conical phase. Close to T_C however, the intensity increases at intermediate magnetic fields, and this is the signature of the A-phase. The boundaries of this phase are given by the infection points of the field dependent neutron intensity, as indicated by the arrows. The maximum intensity of the A-phase scattering occurs at ~ 275.8 K and for a magnetic field of 35 mT. Close to T_C, the peak decreases in intensity and shifts to lower magnetic fields, as seen in Fig. 7.7(b). Surprisingly this feature persists even above T_C, as illustrated by Fig. 7.7(c), where however the intensity is very weak and precise determinations of the field boundaries are difficult.

The resulting magnetic field-temperature phase diagram of FeGe close to T_C is given in Fig. 7.8, where the phase diagram determined from the magnetic susceptibility measurements [6, 7] is included as a reference. Below T_C, the field boundaries of the A-phase, marked by the red squares for the neutron scattering measurement, show a single pocket and cover the A_1 and A_3 phase pockets determined from susceptibility measurement [6, 7]. This is in agreement with previous neutron studies [8]. Above T_C, the low and high field boundaries are also extracted from the neutron scattered intensity, as indicated by the blue squares, which however do not have an equivalence in the susceptibility [6, 7] nor in other measurements [8]. The non-monotonic variation of the magnetic scattering above T_C indicates precursor phenomena to the skyrmion lattice phase that are unique to FeGe.

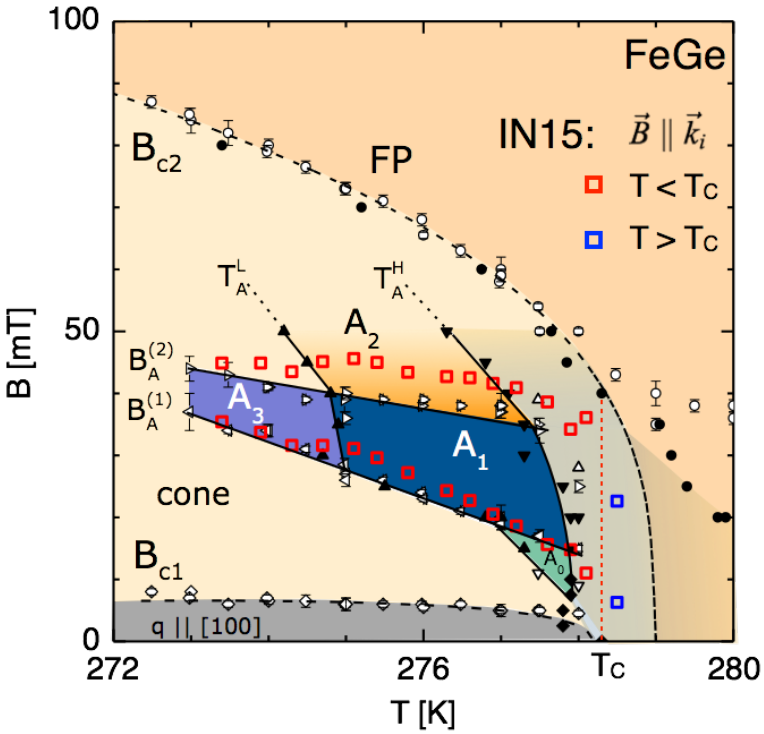

Figure 7.8: Magnetic field-Temperature ($B-T$) phase diagram of FeGe obtained from neutron scattering at IN15 (red and blue squares) in comparison with that determined from magnetic susceptibility measurements (black symbols) [6, 7]. The field boundaries of the A-Phase from neutron scattering were determined from the inflection points of the intensity curves indicated by the arrows in Fig. 7.7.

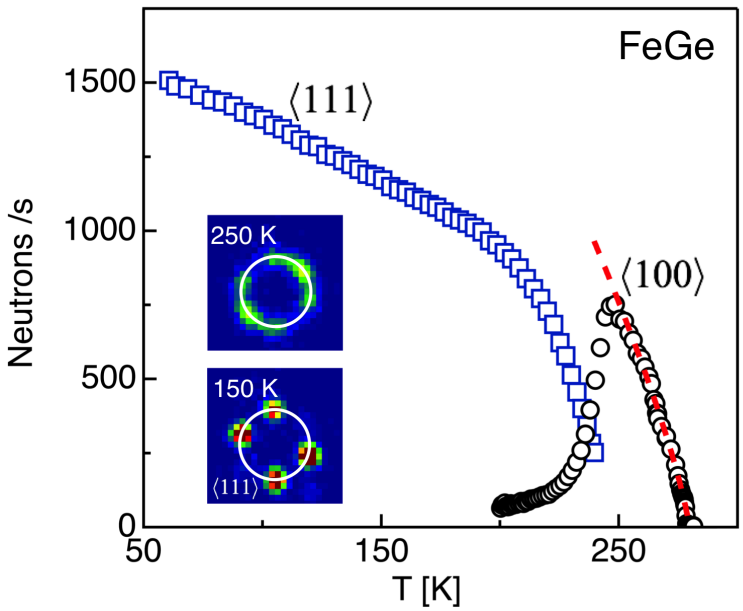

Figure 7.9: Temperature dependence of the scattered neutron intensity at the ⟨111⟩ and ⟨100⟩ magnetic Bragg peak positions. The insets show typical scattering patterns at 250 and 150 K. The white circles in the scattering patterns have a radius of $Q = 0.09$ nm^{-1}.

7.5. HELIX REORIENTATION AT LOW TEMPERATURES AND ZERO FIELD

Fig. 7.9 shows the temperature dependence of the scattered intensity integrated over the ⟨111⟩ and ⟨100⟩ Bragg peak positions, as given schematically in Fig. 7.2. The insets show typical scattering patterns at $T = 150$ K and 250 K.

Below 250 K, the intensity of the ⟨100⟩ Bragg peaks decreases while additional intensity appears at the position of ⟨111⟩ Bragg peaks, leading to broad scattering features shown by the inset scattering pattern at 250 K. These broad features persist down to ~ 200 K.

Below 200 K, the ⟨100⟩ peaks disappear whereas the intensity of the ⟨111⟩ Bragg peaks increases continuously with decreasing temperature. The inset for 150 K shows a typical low temperature scattering pattern, with only the Bragg reflections from the crystallographic ⟨111⟩ directions and weaker high order peaks.

The change in the helix propagation vector is consistent with the previous work by Lebech et. al [3], who has reported the two different helix directions, along ⟨100⟩ at high temperatures and along ⟨111⟩ at low temperatures, on the ba-

sis of SANS experiments. Both crystallographic directions are indeed compatible with the the $P2_13$ space group as it has been theoretically predicted by Bak and Jensen [14]. However, only one helix direction has been found in other B20 chiral magnetic systems such as MnSi and Cu_2OSeO_3. Thus, the change in the helix direction seems to be characteristic for FeGe, and may be due to slight changes in magnetic anisotropy that determines the helix propagation direction. A spin torque experiment by Lundgren et al [15] shows a discontinuity of the anisotropy parameter at ~ 220 K, which seems to agree with this assumption. It is reasonable to assume that the change of anisotropy may originate from a slight distortion of the crystal lattice, and indeed a thermal expansion measurement [11] has reported a slight magnetovolume change in this temperature range.

7.6. CONCLUSION

Small angle neutron scattering in combination with polarisation analysis has been performed in FeGe. Above T_C, the short range magnetic correlations are chiral and transform to a long range helical order at T_C by a transition that is most likely of first order. The magnetic phase diagram reveals the helical, conical and skyrmion lattice phases below T_C, consistent with the literature, and additional scattering that appears just above T_C as a precursor of the skyrmion lattice phase.

In addition, below ~ 250 K and at zero field, the helical order reorients from the ⟨100⟩ to ⟨111⟩ direction. The origin of this phenomenon is not clear and may be due to magnetoelastic coupling and possible structural changes.

REFERENCES

[1] X. Z. Yu, N. Kanazawa, Y. Onose, K. Kimoto, W. Z. Zhang, S. Ishiwata, Y. Matsui, and Y. Tokura, *Near room-temperature formation of a skyrmion crystal in thin-films of the helimagnet FeGe,* Nat Mater **10**, 106 (2010).

[2] N. Romming, C. Hanneken, M. Menzel, J. E. Bickel, B. Wolter, K. Bergmann, A. Kubetzka, and R. Wiesendanger, *Writing and Deleting Single Magnetic Skyrmions,* Science **341**, 636 (2013).

[3] B. Lebech, J. Bernhard, and T. Freltoft, *Magnetic structures of cubic FeGe studied by small- angle neutron scattering,* J. Phys.: Condens. Matter **1**, 6105 (1989).

[4] S. Mühlbauer, B. Binz, F. Jonietz, C. Pfleiderer, A. Rosch, A. Neubauer, R. Georgii, and P. Böni, *Skyrmion lattice in a chiral magnet,* Science **323**, 915 (2009).

[5] X. Z. Yu, Y. Onose, N. Kanazawa, J. H. Park, J. H. Han, Y. Matsui, N. Nagaosa, and Y. Tokura, *Real-space observation of a two-dimensional skyrmion crystal,* Nature **465**, 901 (2010).

[6] H. Wilhelm, M. Baenitz, M. Schmidt, U. K. Rößler, A. A. Leonov, and A. N. Bogdanov, *Precursor Phenomena at the Magnetic Ordering of the Cubic Helimagnet FeGe,* Phys. Rev. Lett. **107**, 127203 (2011).

[7] H. Wilhelm, M. Baenitz, M. Schmidt, C. Naylor, R. Lortz, U. K. Rößler, A. A. Leonov, and A. N. Bogdanov, *Confinement of chiral magnetic modulations in the precursor region of FeGe,* J. Phys.: Condens. Matter **24**, 294204 (2012).

[8] E. Moskvin, S. Grigoriev, V. Dyadkin, H. Eckerlebe, M. Baenitz, M. Schmidt, and H. Wilhelm, *Complex Chiral Modulations in FeGe Close to Magnetic Ordering,* Phys. Rev. Lett. **110**, 077207 (2013).

[9] A. Bauer and C. Pfleiderer, *Magnetic phase diagram of MnSi inferred from magnetization and ac susceptibility,* Phys. Rev. B **85**, 214418 (2012).

[10] M. Richardson, N. Ingri, P. Salomaa, G. Bloom, and G. Hagen, *The Partial Equilibrium Diagram of the Fe-Ge System in the Range 40-72 at. % Ge, and the Crystallisation of some Iron Germanides by Chemical Transport Reactions,* Acta Chem. Scand. **21**, 2305 (1967).

[11] H. Wilhelm, A O Leonov, U. K. R. oßler, P. Burger, F. Hardy, C. Meingast, M. E. Gruner, W. Schnelle, M. Schmidt, and M. Baenitz, *Scaling Study and Thermodynamic Properties of the cubic Helimagnet FeGe,* Phys. Rev. B **94**, 144424 (2016).

[12] C. Pappas, E. Lelièvre-Berna, P. Falus, P. Bentley, E. Moskvin, S. Grigoriev, P. Fouquet, and B. Farago, *Chiral Paramagnetic Skyrmion-like Phase in MnSi,* Phys. Rev. Lett. **102**, 197202 (2009).

[13] V. Dyadkin, K. Prša, S. V. Grigoriev, J. S. White, and P. Huang, *Chirality of structure and magnetism in the magnetoelectric compound Cu_2OSeO_3,* Phys. Rev. B **89**, 140409(R) (2014).

[14] P. Bak and M. H. Jensen, *Theory of helical magnetic structures and phase transitions in MnSi and FeGe,* J. Phys. C: Solid State Phys. **13**, L881 (1980).

[15] L. Lundgren, O. Beckman, V. Attia, S. P. Bhattacheriee, and M. Richardson, *Helical spin arrangement in cubic FeGe,* Phys. Scr. **1**, 69 (1970).

SUMMARY

The research presented in this thesis focuses on chiral magnets, where skyrmion lattices are stablised by magnetic fields. Neutron scattering, magnetisation and magnetic susceptibility measurements have been performed on several typical chiral magnets such as the multiferroic insulator Cu_2OSeO_3 and the metallic MnSi and FeGe.

The measurements on the multiferroic insulator Cu_2OSeO_3 cover up the whole magnetic phase diagram from 5 K up to well above T_C = 58.2 K and are presented in *Chapters* 3 – 5. The high temperature results close to T_C, where skyrmions are stablized, are discussed in *Chapters* 3and 4. *Chapter* 5 focuses on the low temperature phase diagram, where the interplay between the magnetic field and the magnetic anisotropy becomes most noticeable.

Chapter 3 discusses the AC magnetic susceptibility measurements that cover a large frequency range and reveal macroscopic relaxation times of some milliseconds for the transitions between the helical and conical phases at B_{C1} and between the conical and A-phases at B_{A1} and B_{A2}. Such macroscopic relaxation times reflect rearrangements of large magnetic volumes. A strongly non-exponential relaxation was found that bears similarities with spin glasses and is in-line with the glassy behaviour reported by electron microscopy in Cu_2OSeO_3 and other systems with similarly long helices. The resulting magnetic phase diagram of Cu_2OSeO_3 is strongly frequency dependent and the borders between the different phases (helical, conical and A-phase) are not sharp but their exact positions depend on the specific criteria used. The dynamical phenomena could be at the origin of the different phase boundaries reported in the literature not only for Cu_2OSeO_3 but also for other systems of the same family including the reference chiral magnet MnSi.

Neutron scattering close to T_C (*Chapter* 4) shows that the helimagnetic transition of Cu_2OSeO_3 at T_C is of first order. Above T_C, short range chiral magnetic correlations persist. Under magnetic fields in the skyrmion lattice phase, the scattering patterns depend on the crystal lattice orientation and the magnetic history. Long relaxation processes are also seen by rapidly changing the magnetic fields, which go through the magnetic phase diagram between the helical, conical and skyrmion phases.

Below 50 K (*Chapter* 5), neutron scattering and AC magnetic susceptibility as well as DC magnetisation show qualitatively different magnetic phase diagrams

when the magnetic field is applied along the easy ⟨100⟩ or the hard ⟨110⟩ crystallographic directions of Cu_2OSeO_3. More specifically, strong dissipation appears close to B_{C2}, but only below 30 K and is more pronounced when the magnetic field is applied along the easy axis ⟨100⟩. Complementary observations are provided by neutron scattering, which shows additional scatterings below ~ 30 K and only for the magnetic field along the easy ⟨100⟩ axis. Those features may be related to the cubic anisotropy. In addition, the transition from the helical to the conical phase splits to two adjacent B_{C1} lines and below 50 K. Macroscopic characteristic times of milliseconds with broad distributions are observed both at B_{C1} and B_{C2}, which may eventually prevent the system from reaching thermal equilibrium and lead to thermal hysteresis.

Comprehensive AC magnetic susceptibility measurements were also performed on the archetype chiral magnet MnSi, covering a frequency range from 0.5 to 1000 Hz (*Chapter* 6). By going to low frequencies, strong dissipation is found above T_C and under magnetic fields, which vanishes at the transition to the conical phase along B_{C2}. The associated long characteristic times reflect slow relaxation dynamics and indicate the relaxation of large objects above T_C.

High resolution small angle neutron scattering studies were performed on FeGe, which is ordered just below room temperature (*Chapter* 7). Magnetic helices at zero field reorient from the high temperature ⟨100⟩ to the low temperature ⟨111⟩ directions, at temperatures between 250 and 200 K. Close to T_C, the magnetic scattering is consistent with a first order phase transition. Chiral magnetic short-range correlations are observed above T_C, which on the application of magnetic field vary non-monotonically with the magnetic field.

In conclusion, the neutron scattering and magnetic susceptibility experiments on a variety of chiral magnets provide insights on the static magnetic correlations and the dynamical phenomena in connection with the magnetic phase diagram and phase transitions. The results presented in this thesis contribute to understanding the chiral magnetism including the helical, conical and skyrmion lattice phases. They pave the way to future investigations in conjunction with theory to control and manipulate the helimagnets and skyrmion lattices in view of potential applications in the future.

SAMENVATTING

Het onderzoek dat in dit proefschrift gepresenteerd wordt concentreert zich op chirale magnetische systemen waarin magnetische velden skyrmionroosters stabiliseren. Neutronenverstrooiing, magnetisatie- en magnetische susceptibiliteitsmetingen zijn uitgevoerd op meerdere chirale magneten zoals de multiferroische isolator Cu_2OSeO_3 en de metallische systemen MnSi en FeGe.

De metingen met betrekking tot Cu_2OSeO_3 bestrijken het hele magnetisch fase diagram van 5 K tot ver boven de kritische temperatuur $T_C = 58.2$ K en worden gepresenteerd in *Hoofdstukken* 3 – 5. De hoge temperaturen dichtbij T_C, waar Skyrmionen stabiel zijn, worden besproken in *Hoofdstuk* 3 en 4. *Hoofdstuk* 5 legt de nadruk op het fasediagram bij lage temperaturen, waar de interactie tussen het magnetisch veld en de magnetische anisotropie het duidelijkste zijn.

Hoofdstuk 3 bespreekt de AC magnetische susceptibiliteitsmetingen die een groot frequentiebereik beslaan en welke macroscopische relaxatie tijden laten zien van enkele milliseconden voor de transities tussen de helische en conische fase die plaatsvindt bij B_{C1} en tussen de conische en A-fase rondom B_{A1} en B_{A2}. Zulke macroscopische relaxatietijden reflecteren herrangschikkingen van grote magnetische volumes. Een sterke niet-exponentiële relaxatie is gevonden die overeen komt met relaxaties in spin-glas systemen en die in overeenstemming is met het glasachtig gedrag gerapporteerd op basis van elektronen microscopie in Cu_2OSeO_3 en andere systemen met gelijksoortige lange helices. Het resulterende magnetische fasediagram voor Cu_2OSeO_3 is sterk frequentie afhankelijk en de grenzen tussen de verschillende fases (helische, conische, en A-fase) zijn niet scherp maar hun exacte posities hangen af van de specifieke criteria die gebruikt worden. De dynamische fenomenen liggen mogelijk ten grondslag aan de verschillende fasegrenzen die gerapporteerd zijn in de literatuur, niet alleen voor Cu_2OSeO_3 maar ook voor andere systemen uit de zelfde familie inclusief de referentie chirale magneet MnSi.

Neutronen verstrooiing dichtbij T_C (*Hoofdstuk* 4) laat zien dat de helimagnetische transitie in Cu_2OSeO_3 een eerste-orde overgang is. Boven T_C blijven chirale magnetische correlaties met een korte dracht bestaan. In de skyrmionroosterfase onder magnetische velden hangen de verstrooiingspatronen af van de kristalroosteroriëntatie en de magnetische geschiedenis. Processen met lange relaxatieduur zijn ook te zien wanneer het magnetisch veld snel veranderd wordt,

waarbij de relaxatie door het gehele magnetische fasediagram gaat tussen de helische, conische en skyrmionische fases.

Beneden 50 K (*Hoofdstuk* 5) laten neutronen verstrooiing en AC magnetische susceptibiliteit alsmede DC magnetisatie metingen kwalitatief verschillende magnetische fasediagrammen zien wanneer het magnetisch veld langs de gemakkelijke ⟨100⟩ of de lastige ⟨110⟩ kristallografische richtingen van Cu_2OSeO_3 wordt aangelegd. Specifieker, sterke dissipatie treedt op dichtbij B_{C2} maar alleen beneden de 30 K en deze is meer uitgesproken wanneer het veld langs de gemakkelijke as ⟨100⟩ wordt aangelegd. Complementaire observaties worden gegeven door neutronen verstrooiing, welke ook additionele verstrooiing laat zien beneden de ~ 30 K maar alleen wanneer het veld langs de gemakkelijke ⟨100⟩ as is. Deze aspecten houden mogelijk verband met aan de kubische anisotropie. Verder splitst de transitie tussen de helische en conische fase in twee nabijgelegen B_{C1} lijnen beneden de 50 K. Macroscopische karakteristieke tijden van milliseconden met brede verdelingen worden waargenomen rond zowel B_{C1} als B_{C2}, wat mogelijk uiteindelijk voorkomt dat het systeem in thermisch evenwicht komt en daarmee tot thermische hysterese leidt.

Uitgebreide AC magnetische susceptibiliteitsmetingen zijn ook gedaan voor de typische chirale magneet MnSi met een groot frequentiebereik van 0.5 tot 1000 Hz (*Hoofdstuk* 6). Door naar lage frequenties te kijken, is sterke dissipatie gevonden boven T_C en onder magnetische velden, die verdwijnt bij de conische transitie langs B_{C2}. De bijbehorende lange karakteristieke tijden reflecteren trage relaxatiedynamica en duiden op relaxaties van grote objecten boven T_C.

Hoge resolutie kleine hoek neutronenverstrooiing metingen zijn uitgevoerd voor FeGe, waarin de ordening net beneden kamertemperatuur plaatsvindt (*Hoofdstuk* 7). Magnetische helices bij veld nu heroriënteren zich van de ⟨100⟩ richting die gezien wordt bij hoge temperaturen tot de ⟨111⟩ richting die bij lage temperaturen gezien wordt, waarbij deze heroriëntatie plaatsvindt tussen de 250 en 200 K. Dichtbij T_C is de magnetische verstrooiing consistent met een eerste order faseovergang. Chirale magnetische korte-drachts gezien boven T_C, welke onder aanleg van een magnetisch veld niet-monotoon veranderen met het magnetisch veld.

Concluderend kunnen we stellen dat de neutronenverstrooiing en magnetische susceptibiliteitsexperimenten aan een verscheidenheid aan chirale magneten inzicht geven in de statische magnetisch correlaties en dynamische fenomenen in relatie tot de magnetische fasediagrammen en faseovergangen. De resultaten die in dit proefschrift gepresenteerd worden leveren een bijdrage aan het begrip van chiraal magnetisme inclusief de helische, conische en skyrmionrooster fases. Zij maken het pad vrij voor toekomstige onderzoeken in samenspel met theorie voor de controle en manipulatie van helimagneten en skyrmionroosters

in het licht van potentiele toepassingen in de toekomst.

ACKNOWLEDGEMENTS

It is an exciting moment to write this part of the thesis as it is the finishing touch! When I look back, the nearly five years' life in Delft is converging into wonderful memories. I feel lucky to have so many friends and colleagues helping, supporting and encouraging me to achieve this great milestone and I had such a wonderful life in the Netherlands. Let me take this opportunity to express my sincere gratitude to all of them.

First of all, I would like to give my deepest appreciation to my supervisor Professor Catherine (Katia) Pappas, who has definitely been the most important person all long my PhD. Dear Katia, thank you very much for leading me into the wonderful world of chiral magnetism and neutron scattering, and for your enthusiastic encouragement and tremendous effort during my PhD project. I really appreciate your responsible attitude and the time we spent together during the experiments as well as our weekly discussions on science and life. You taught me to think critically and your rigorous approach to science will be beneficial to my scientific career. My gratitude to your support and guidance will never be limited to this paragraph.

Another very important person for my PhD is Dr. habil. Heribert Wilhelm from Diamond Light Source, UK. We met during an experiment at the very beginning of my PhD and since then he showed continuous interest and support to my work, which I deeply appreciate. Dear Heribert, I am very thankful for the regular and intensive discussions we had via Skype on our experiments and common publications.

My gratitude also goes to the other members of my PhD committee: Dr. habil. Grégory Chaboussant, Dr. Eddy Lelièvre-Berna, Prof. Maxim Mostovoy, Prof. Ekkes Brück and Dr. Ad van Well. I thank all of you not only for reading my thesis, but also for your great contribution to my PhD project. Dear Grégory, I would like to thank you for your great support during the experiments at PAXY and PA20, LLB, Saclay. Thank you so much for picking me up from "La Porte du Nord" and for driving me back to my hotel even in the middle of the night. Without your help, the experiments would not have been so successful. Dear Eddy, I appreciate your great contribution to our polarised neutron scattering measurements at the ILL and the discussions on polarimetry matrices. With you I learnt how to eat the french way and this includes an unforgettable Champagne dinner I enjoyed with you, Isabelle and Katia in Grenoble. Dear Maxim, thank you

so much for the enlightening discussions and your work on my experimental results. Without your comprehensive contribution, it would have been impossible for me to interpret my experimental findings. More is underway and we will certainly keep in touch to understand the whole repercussions of these results. Dear Ekkes, I thank you for your support with the AC susceptibility measurements and your great help every time I had questions. My thanks also go to Ad, to whom I acknowledge his involvement at the beginning of my PhD and the master course from which I learned a lot of about neutron and X-ray scattering.

A lot of thanks go to all my collaborators, to whom I am greatly indebted. I am very thankful to Dr. Ashia Aqeel and Prof. Thom Palstra from the Zernike institute of Groningen University for providing the Cu_2OSeO_3 samples for the susceptibility measurements, from which I achieved many excellent results. I would like to thank Dr. Grame Blake for the alignment of the samples on the single crystal diffractometer in Groningen. My gratitude also goes to Dr. Peter Falus and Dr. Charles Dewhurst from the ILL for the help with the neutron experiments at IN15 and D33, respectively, to Prof. Kazuhisa Kakurai from JAEA for the experiments at IN15 and the help with data analysis, and to Dr. Nicolas Martin from the LLB for the great help with experiments at PA20 and the Igor files for data analysis. I thank Dr. Marcus Schmidt from MPI Dresden for providing the FeGe and Cu_2OSeO_3 samples for the neutron measurements, to Dr. Thomas Lograsso from Ames Laboratory for the MnSi sample used for the susceptibility measurements. I would also like to thank Prof. Katsuya Inoue for inviting me to Hiroshima University and for the discussions on the susceptibility measurements. Special thanks go to Prof. Alex Bogdanov from IFW Dresden and Dr. Andrey Leonov who is currently at Hiroshima University for the enlightening discussions on my experimental results. Andrey, I deeply appreciate your theoretical simulations of my data. Without your great help, we will not have been able to move forward with the data interpretation. I look forward to the publication with you and Maxim that will follow very soon.

At Delft, I was very lucky to have so many supportive colleagues from the NPM2 and FAME sections. Firstly, I would like to give a thumb to our lovely ladies Nicole Banga, Ilse van der Kraaij and Trudy Beentjes for arranging properly all administrative matters. Your great assistance really saved me a lot of time and made my life easier. My special thanks go to Anton Lefering, who has been very important for the susceptibility measurements. Dear Anton, you have always been amazingly kind and helped me with changing the SQUID heads from DC to AC modes, performing intensive calibration work and keeping an eye on my data detecting any bad points. My great thanks also go to Lars Bannenberg, my first colleague on chiral magnetism at Delft, for the common experiments and our great discussions on research and life. I would like to thank Dr. Jouke

Heringa for his simulations of chiral magnetism and the inspiring discussions that greatly deepen my understanding of the research. Dear Lars and Jouke, I deeply thank you for the Dutch translation of the summary and the propositions of my thesis. Last but not least, I would like to thank Dr. Wicher Kraan for his great help with the BEP student project on PANDA and the enlightening discussions of polarimetry matrices.

Certainly, chiral magnetism has always been a fancy topic at the coffee machine, a great place to brainstorm and drink with colleagues from various research backgrounds and cultures. Theo Rekveldt, it is always inspiring to talk skyrmion with you and thank you for your interest and useful comments during and after every work discussion I gave. Henk Schut and Wim Bouwman, thank you for those great group day outs, which deepened my knowledge of Delft and Amsterdam. Lambert van Eijck and Jeroen Plomp, time with you has always been nice and at my ease. I enjoyed very much the trips I had with you to Zaragoza and to Sydney, respectively. Talks with Piet van de Ende, Martijn de Boer, Kees de Vroege, Fred Naastepad, Michel Steenvoorden, Kees Goubitz and Paul Gubbens have always been interesting and full of fun. I also had a great time chatting and playing games with excellent colleagues from the NPM2 section: Steven Parnell, André Kusmin, Zhou Zhou, Bei Tian, Michel Thijs, Jurrian Bakker, Evgenii Velichko, Serge Duarte Pinto, Chuanqing Shi, and the FAME section: Luana Caron, Niels Van Dijk, Thang Nguyen, Yibole, Zhiqiang Ou, Maurits Boeije, Dimitris Bessas, Jose Leit*ão*, Swapna Ganapathy, Prasad Gonuganta, Stephan Eijt, Niek de Klerk, Peter-Paul Harks, Violetta Arszelewska, Xiaoyu Zhang, Shasha Zhang, Wenqin Shi, Haixing Fang, Lei Ma, Jiawei Lai, Bowei Huang, Xinmin You, Heng Wang, Chao Wang, Yaolin Xu, and Bo Peng. Special thanks go to Bert Zwart and Ben Harrison for their warm welcome to Alkmaar and to the wonderful football game that I saw on the spot for the first time in my life.

My thanks also go to my roommates for the quite but happy atmosphere in these years: to Anca Anastasopol, Anna Grzech, Kun Shen, Chuang Yu, Zhaolong Li, Thomas Verhallen, Michael Maschek, Francois Guillou, Martijn van Hulzen, Maxim Ariens, and Casper Versteylen. It was amazing that I have shared office with so many people. I particularly thank Shasha Lyu for staying with me at home, the last months when I was alone in Delft.

Moreover I would like to thank my friends that have not been directly involved in my research but made my life in Delft colourful: Prasenjit Roy, Shan Shen, Hao Chen, Jiayi Chen, Tiantian Yao, Qian Feng, Mengqiu Zheng, Qiao Pan, Hongde Luo, Zheng Liu, Nan Zhong, Lian Zhang and Lily Li. Again, I would like to thank you all for making my time in the Netherlands so impressive and memorable!

I am particularly grateful to my master supervisor Prof. Renli Fu for support-

ing my PhD application and for agreeing that I wrote my master thesis while I was in Delft. I also would like to thank Cees Timmers for recommending me to TU Delft and for his support.

Last but not the least, I would like to express my deepest love to my family: my parents, my grandmother, my parents in-law and my younger sister Meijiao Qian. They have supported me spiritually throughout my PhD and throughout my life in general. I also thank Jie Gu, Chun Cai and Liujin Wu for making my holidays in China full of fun and tasty food. Finally, special thanks go to my beloved husband, Dr Xuefei Miao, with whom I am happy to share my life not only in the past but also in the future. We support each other in daily life and in science. Dear Xuefei, at my rough times, you have always cheered me up and encouraged me to move forward. Your commitment makes me feel secure and strong. Life is so beautiful with you!

LIST OF PUBLICATIONS

PUBLICATIONS

1. **F. Qian**, H. Wilhelm, L.J. Bannenberg, G. Chaboussant, P. Falus, E. Lelièvre-Berna, M. Schmidt, and C. Pappas, *"Magnetic correlations and dynamics close to T_C in Cu_2OSeO_3: Small angle neutron scattering and neutron spin echo spectroscopy studies"*, in preparation.

2. **F. Qian**, A.J.E. Lefering, L.J. Bannenberg, E. Brück, T.A. Lograsso, and C. Pappas, *"Dissipation phenomena and magnetic phase diagram of MnSi"*, in preparation.

3. **F. Qian**, H. Wilhelm, L.J. Bannenberg, G. Chaboussant, P. Falus, E. Lelièvre-Berna, M. Schmidt, and C. Pappas, *"Chiral Magnetism in FeGe: A polarised neutron scattering study"*, in preparation.

4. **F. Qian**, L.J. Bannenberg, H. Wilhelm, G. Chaboussant, A.J.E. Lefering, A. Aqeel, M. Schmidt, T.T.M. Palstra, E. Brück, C. Pappas, M. Mostovoy and A.A. Leonov, *"Dissipation phenomena and magnetic phase diagram of Cu_2OSeO_3 below 50 K"*, arXiv:1611. 06014 (2016).

5. **F. Qian**, H. Wilhelm, A. Aqeel, T.T.M. Palstra, A.J.E. Lefering, E.H. Brück and C. Pappas, *"Phase diagram and magnetic relaxation phenomena in Cu_2OSeO_3"*, Phys. Rev. B **94**, 064418 (2016).

6. L.J. Bannenberg, K. Kakurai, P. Falus, E. Lelièvre-Berna, R. Dalgliesh, C.D. Dewhurst, **F. Qian**, Y. Onose, Y. Endoh, Y. Tokura, and C. Pappas, *"Universality of the helimagnetic transition in cubic chiral magnets: Small angle neutron scattering and neutron spin echo spectroscopy studies of FeCoSi"*, Phys. Rev. B **95**, 144433 (2017).

7. L.J. Bannenberg, K. Kakurai, **F. Qian**, E. Lelièvre-Berna, C.D. Dewhurst, Y. Onose, Y. Endoh, Y. Tokura, and C. Pappas, *"Extended skyrmion lattice scattering and long-time memory in the chiral magnet $Fe_{1-x}Co_xSi$"*, Phys. Rev. B **94**, 104406 (2016).

8. X.F. Miao, L. Caron, J. Cedervall, P.C.M. Gubbens, P. Dalmas de Réotier, A. Yaouanc, **F. Qian**, A.R. Wildes, H. Luetkens, A. Amato, N.H. van Dijk and E. Brück, *"Short-range magnetic correlations and spin dynamics in the paramagnetic regime of $(Mn,Fe)_2(P,Si)$"*, Phys. Rev. B **94**, 014426 (2016).

CONFERENCE PRESENTATIONS

1. Oral presentation: **F. Qian**, L.J. Bannenberg, C. Pappas, *et al*, *"Dissipation phenomena and magnetic phase diagram of Cu_2OSeO_3"*, IV DMI Workshop, Peterhof, Russia, 2017.

2. Oral presentation (invited): **F. Qian**, H. Wilhelm, C. Pappas, *et al*, *"Dissipation phenomena and magnetic phase diagram of Cu_2OSeO_3 close to T_C"*, χ-Mag Symposium, Hiroshima, Japan, 2016.

3. Oral presentation: **F. Qian**, H. Wilhelm, C. Pappas, *et al*, *"A Polarised Neutron Approach to Chiral Magnetism: The case of cubic FeGe"*, VI ECNS conference, Zaragoza, Spain, 2015.

4. Poster presentation: **F. Qian**, H. Wilhelm, C. Pappas, *et al*, *"Chiral Magnetism in multiferroic insulator Cu_2OSeO_3: A polarised neutron scattering study"*, VI ECNS conference, Zaragoza, Spain, 2015.

5. Poster presentation: **F. Qian**, H. Wilhelm, C. Pappas, *et al*, *"A Polarised Neutron Approach to Chiral Magnetism: The case of multiferroic Cu_2OSeO_3"*, 20^{th} International Conference on Magnetism, Barcelona, Spain, 2015.

6. Poster presentation: **F. Qian**, H. Wilhelm, C. Pappas, *et al*, *"A Polarised Neutron Approach to Chiral Magnetism: The case of multiferroic Cu_2OSeO_3"*, FOM Physics, Veldhoven, the Netherlands, 2015.

7. Oral presentation (invited): **F. Qian**, H. Wilhelm, C. Pappas, *et al*, *"A Polarised Neutron Approach to Chiral Magnetism: The case of cubic FeGe"*, PNCMI, Sydney, Australia, 2014.

8. Poster presentation: **F. Qian**, H. Wilhelm, C. Pappas, *et al*, *"Polarized neutron scattering on a long-range helimagnet FeGe"*, SYNEW, Antwerp, Belgium, 2013.

CURRICULUM VITÆ

Fengjiao QIAN

Fengjiao Qian was born on December 17th, 1988 in Hefei, Anhui Province, China. In 2006, she attended Nanjing University of Aeronautics and Astronautics as an undergraduate student and majored in Materials Science and Engineering. After four years study, in 2010, she was entitled the bachelor degree on a thesis "Synthesis and luminescent properties of a red phosphor for warm white LEDs", and was recommended as a master student in the same university with exemption from the admission examinations.

After two and half years study, she obtained her Master degree as a material scientist in the Spring of 2013. The master project, supervised by Prof. Renli Fu, was on studying the synthesis and luminescent properties of $Ca_3Si_2O_7$-based red phosphor for warm white LEDs with high color index.

During the master period, she received a scholarship from the China Scholarship Council to pursue a PhD degree abroad. She moved to Delft, the Netherlands, August 2012, where she finished her MSc March 2013. Immediately afterwards she started her PhD in the section Neutron and Positron Methods in Materials (NPM2) at Delft University of Technology. The PhD research was supervised by Prof. Catherine (Katia) Pappas and was focused on the investigation of static and dynamic properties of chiral magnetism in cubic chiral magnets Cu_2OSeO_3, MnSi and FeGe using a variety of experimental techniques: DC and AC magnetometry, Small Angle Neutron Scattering (SANS), Spherical Neutron Polarimetry, Neutron and Spin Echo Spectroscopy. The results of this research are presented in this thesis entitled "Static and Dynamic properties of Cubic Chiral Magnets".